UAB

Universitat Autònoma de Barcelona

Nanoscale Investigation and Control of the Interfacial Properties of Organic Solar Cells and Organic Thin-Film Transistors

A Dissertation in partial fulfilment of the requirements for the degree of

DOCTOR OF PHILOSPHY IN PHYSICS

Universidad Autónoma de Barcelona

by

Mahdieh Aghamohammadi

Dr. Esther Barrena Villas, PhD Advisor

Dr. Hagen Klauk, PhD Advisor

Prof. Javier Rodríguez Viejo, Tutor

Department of Physics, Universidad Autónoma de Barcelona (UAB)

Max Planck Institute for Solid State Research, Stuttgart (MPI-FKF)

Instituto de Ciencia de Materiales de Barcelona (ICMAB-CSIC)

2016

To my parents

and

Malte,

My husband and best friend for life

Abstract

Thin-film and interface properties of organic semiconductors are among the most prominent aspects with regard to the overall performance of organic electronic devices. The interface formed between two organic materials can influence the electronic and optical properties of organic electronic devices by determining the growth mechanisms, morphology, defect density and the electronic interface structures of organic films.

The impact of the relative molecular orientation at the organic/organic interface on the performance of organic solar cells is one of the less understood factors and thus, it represents an outstanding opportunity for research and technologies based on the control of the local molecular ordering of the organic molecules in donor/acceptor organic photovoltaics. Using state-of-the-art scanning probe microscopy techniques and photoluminescence studies a clear link between the relative molecular orientation of the DIP (donor)/PTCDI-C_8 (acceptor) heterostructures and an emissive charge transfer state is demonstrated, which is ultimately associated with an efficient π-orbital overlap at the interface.

Another extremely interesting organic/organic interface is the one found in organic thin-film transistors (TFTs), where the gate dielectric contains organic species such as self-assembled monolayers (SAMs). The use of SAMs opens an appealing path of research in manufacturing TFTs with the desired operating voltages, due to the observation that the threshold voltage can be modulated using different SAMs. Revealing the underlying mechanisms of this phenomenon, which is known as threshold-voltage shift, signifies a considerable challenge. Kelvin probe force microscopy (KPFM) was used as a powerful tool to explore at the nanoscale the electronic properties at the interface between DNTT and two different SAMs namely an alkly- and a fluoroalkylphosphonic acid SAM. A systematic series of KPFM investigations combined with the analysis of the transistor parameters reveals gate-oxide capacitance-dependent threshold-voltage shift as a result of interface electronic interactions at the DNTT/fluoroalkyl SAM interface. On the contrary, the DNTT transistors with the alkyl SAMs exhibit a small capacitance-independent threshold-voltage shift, associated with the intrinsic dipole-induced electrostatic potential of the SAM.

Together, the studies carried out in this thesis represent innovative approaches utilizing controlled organic semiconductor processing methods and complementary techniques, which enabled us to achieve a better understanding of different electronic processes at the

interfaces involved in organic solar cells and organic thin-film transistors. This thesis emphasizes the relevance of achieving controlled interface architectures with exciting potential for future interface engineering in organic electronic devices.

Zusammenfassung

Dünn- und Grenzschichteigenschaften von organischen Halbleitern gehören zu den wichtigsten Gesichtspunkten, um die Charakteristika organischer elektronischer Geräte zu verbessern. Die Grenzschicht zwischen zwei organischen Materialien kann auf die elektronischen und optischen Eigenschaften des organischen elektronischen Gerätes einwirken, indem es den Wachstumsmechanismus, die Morphologie, die Defektdichte und letztlich auch die elektronischen Strukturen in der Nähe der Grenzschicht vorgibt.

Der Einfluss der relativen molekularen Orientierung an der organisch-organischen Grenzschicht gehört zu den am schlechtesten verstandenen Einflussgrößen und stellt somit eine herausragende Möglichkeit für die Forschung und für Technologien dar, die darauf basieren, die lokale molekulare Ordnung in Donor/Akzeptor Photovoltaikzellen zu manipulieren. Durch die Verwendung von modernster Rastersondenmikroskopie und Photolumineszenzuntersuchungen wurde eine klare Verbindung zwischen der relativen molekularen Orientierung in den DIP (Donor)/PTCDI-C$_8$ (Akzeptor) - Heterostrukturen und einem fluoreszierenden Charge-Transfer-Komplex gezeigt, was auf eine effiziente Überlappung der π-Orbitale hindeutet.

Eine weitere höchstinteressante organisch-organische Grenzschicht kann in organischen Dünnschichttransistoren (thin-film transistors - TFTs) beobachtet werden, in denen das Gate-Dielektrikum aus organischen Materialien wie selbstorganisierenden Monoschichten (self-assembled monolayers - SAMs) besteht. Die Verwendung von SAMs eröffnet aufgrund ihrer Eigenschaft, die Schwellenspannung zu verändern, die reizvolle Möglichkeit, TFTs mit bestimmten Arbeitsspannungen zu fertigen. Den zugrundeliegenden Mechanismus dieses oft beschriebenen Phänomens, der Schwellenspannungsverschiebung, zu beleuchten, stellt eine große Herausforderung dar. Die leistungsfähige Raster-Kelvin-Mikroskopie (Kelvin probe force microscopy - KPFM) wurde verwendet, um die elektronischen Eigenschaften an der Grenzschicht zwischen DNTT und zwei verschiedenen SAMs, eine Alkyl- und eine Fluoralkylphosphorsäure-SAM, im Nanobereich zu untersuchen. Eine systematische Reihe von KPFM-Untersuchungen in Kombination mit einer Auswertung der Transistorenparameter offenbarte eine Abhängigkeit der Schwellenspannungsverschiebung von der Gateoxid-Kapazität aufgrund von elektronischen Grenzschichtwechselwirkungen an der DNTT/Fluoralkyl-SAM-Grenzschicht. Im Gegensatz dazu weisen die DNTT-Transistoren mit Alkyl-SAMs eine kleine kapazitätsunabhängige Schwellenspannungsverschiebung auf, die im

Zusammenhang mit dem intrinsischen dipolinduzierten elektrostatischen Potential der SAM steht.

Die Projekte, die in dieser Arbeit präsentiert werden, stellen als Ganzes eine Reihe von innovativen Herangehensweisen dar, die uns durch hochkontrollierte Herstellungsmethoden für organische Halbleiter und durch komplementäre Untersuchungsmethoden ermöglichten, ein besseres Verständnis für die verschiedenen elektronischen Prozesse an den Grenzflächen, die bei organischen Solarzellen und organischen Dünnschichttransistoren eine Rolle spielen, zu erlangen. Diese Arbeit unterstreicht die Wichtigkeit, die Grenzschichtarchitektur zu kontrollieren, mit aufregenden Möglichkeiten für zukünftiges Grenzschichtdesign in organischen elektronischen Geräten.

Stichwörter: Organische Halbleiter, organische Solarzellen, Charge-Transfer-Komplex, organische Dünnschichttransistoren, Schwellenspannungsverschiebung, Raster-Kelvin-Mikroskopie

Content

"I have a suspicion that things make it a lot more obscure before they become clearer."

Sherlock Holmes, the Rediscovered Railway Mysteries and Other Stories by John Taylor.

1. Introduction

The use of organic molecular materials with semiconducting properties for electronic and optoelectronic applications has drawn growing attention over the last two to three decades because of certain advantages they have over their traditional inorganic counterparts, such as silicon and germanium. Although organic semiconductor devices are not and probably will never be able to compete with inorganic semiconductor devices in terms of performance, the advantages of organics, such as low-temperature processing and their potential for large area manufacturing on flexible substrates have made them attractive candidates for the development of new fields of applications. Three major classes of organic electronic devices, namely organic photovoltaic cells (OPVCs), organic light-emitting diodes (OLEDs) and organic field-effect transistors (OFETs) have shown promising features, with OLEDs being already considered popular choices in the market of electronic devices. OPVCs and OFETs have shown propitious advances and are currently on the verge of commercialization.

Despite the many advances in the field of organic electronics, a number of obstacles remain before the full realization of high-performance organic electronic devices. One of these obstacles concerns the optimization of the involved interfaces and obtaining control over the different aspects of the interfaces formed in organic electronic devices. To overcome this issue, intensive research has been carried out worldwide for the synthesis of new functional materials with desired electronic properties, through which optimum energy-level alignments at the organic/electrode and organic/organic interfaces could be achieved.[1] Therefore, the development of novel high-performance organic semiconductors has been a popular strategy to enhance the performance and stability of organic electronic devices. The type of interactions that occur at an organic/organic interface, however, is not only an effect of the materials involved but also of the way the molecules arrange at the interface. One of the less systematically studied aspects of the organic/organic interfaces is the role of the structural order at the interface. The local order in thin films of organic semiconductors can affect the interface electronic properties.[1]

In modern multilayer organic devices, for applications involving more than one organic component, the organic/organic interfaces formed between two different organic materials are critical features essential to the optimum performance of the devices. However, compared to the organic/electrode interface, the electronic phenomena occurring at the organic/organic interfaces are poorly regarded.

The importance of interfaces for the device performance cannot be overestimated. In organic solar cells based on the donor/acceptor concept, optimum interfacial structural and electronic properties are critical for efficient charge separation, and can significantly affect the open-circuit voltage.[1,2] In systems used for solar cells, special attention needs to be paid to the crystalline order of the materials, due to the fact that the transport properties of excitons are strongly affected by the structural order of the involved materials. As organic semiconductors usually suffer from low crystallinity and thus from small exciton diffusion lengths, the morphology of the active layer in organic solar cells is considered a crucial parameter for efficient exciton dissociation processes. There are two main factors that determine the successful implementation of a donor/acceptor (D/A) system for application in solar cells; one is the energy level alignment at the interface, meaning that the D/A pair is required to be energetically favorable for charge separation, and the second factor is the morphological aspect of the interface formed between the donor and the acceptor. The first point has been subject to thorough research over the course of many years. The latter, however, has not received proper attention, although it can be equally as important as the former. In-depth investigations need to be conducted in order to gain control over the structural and electronic properties at the D/A interface and to optimize the architectures. In the D/A solar cell configuration, of particular interest could be the investigation of the optical phenomena at the D/A interface, such as charge transfer (CT) states. CT states are highly-regarded phenomena in solar cells because of their role as intermediate states that facilitate exciton dissociation. CT states can also act as recombination centers for the charges. They are, however, not easily detected in organic systems, due to their weak emission and the fact that they are often superimposed by the emission from the pristine donor and acceptor phases.

Organic field-effect transistors are the next class of organic electronic devices, in which the interfaces formed between the various species play an essential role in the performance of these devices, *e.g.* by determining the charge transport properties. The different aspects of the insulator/semiconductor interface in OFETs, such as the semiconductor morphology, the presence of defects acting as traps, the surface roughness, the surface energy of the dielectric and the presence of dipoles at the interface, can play a decisive part in determining the carrier mobility, threshold voltage and subthreshold slope of a transistor. The semiconductor/dielectric combination can even determine the polarity of the transistor.[3] Another important transistor parameter that can be linked to the interface properties is the operating voltage of the transistor. For the application of OFETs in complementary logic devices it is desirable to obtain small operating voltages

with the ability to set the threshold voltage to a certain value. A promising approach to reach this goal is the passivation of the gate-oxide surface with self-assembled monolayers (SAMs). Treatment of the gate-oxide of organic transistors with SAMs results in improved transistor parameters, such as the field-effect mobilities, the I_{on}/I_{off} current ratios, the subthreshold slopes and the threshold voltages. The threshold-voltage shift phenomenon,[*] which is one of the most important consequences of the oxide passivation with SAMs, has been the subject to intensive research over the course of the last decade. In spite of the considerable advances in understanding the underlying mechanisms of the threshold-voltage shift phenomenon by SAMs and the fact that it has been addressed by numerous groups, the physical origins of this phenomenon are still open to debate and in fact, have not yet been investigated systematically.

The general objective of this thesis is to develop a profound understanding of the impact of the interfacial properties of films of organic semiconductors on the various processes that determine the performance of organic solar cells and organic transistors. More specifically, the two main objectives include addressing, firstly, the impact of the relative molecular orientation at the D/A heterojunction interface on the exciton dissociation in organic solar cells and, secondly, the impact of the SAMs on the threshold-voltage shift phenomenon in organic transistors.

To reach this goal, a series of systematic investigations on the growth of different vacuum-sublimed organic semiconductors and on the electronic phenomena occurring at their relevant interfaces are carried out. Advanced scanning probe microscopy techniques are employed to study the different properties of the films and the interfaces down to the nanoscale.

This thesis consists of seven chapters that include four results chapters. Chapter 2 provides an introduction to the field of organic electronics with three main sections including organic semiconductors, organic solar cells and organic transistors. In Chapter 3 detailed information on the substrate preparation, sample fabrication and characterization techniques employed in the thesis are presented.

In Chapter 4, the first results chapter of the thesis, the effect of the relative molecular orientation of the donor and the acceptor components in a donor/acceptor heterojunction

---

[*] By threshold-voltage shift, the SAM-induced threshold-voltage shift is meant, which should not be mistaken with the gate-bias induced shift. See Chapter 2 for more details.

system, consisting of diindenoperylene (DIP) and a perylene-diimide derivative (PTCDI-C_8), on the exciton dissociation is investigated.

The second results part of the thesis consists of three chapters, devoted to the importance of interfaces involved in organic thin-film transistors (TFTs). Chapter 5 is a groundwork and preliminary to a series of investigations on organic TFTs based on the high-performance organic semiconductor dinaphto-thieno-thiophene (DNTT). In Chapter 5, DNTT transistors are realized on aluminum oxide functionalized with SAMs. The experiments in this chapter are expanded in Chapter 6, where the threshold-voltage shift caused by the presence of the SAMs is systematically studied.

In Chapter 6, the responsible mechanisms for shifting of the threshold voltage of DNTT TFTs upon the gate-oxide functionalization with various SAMs are identified. For this purpose, the dependence of the threshold voltage on the gate-dielectric capacitance is investigated. The capacitance dependence (or independence) of the threshold voltage provides a unique criterion to distinguish different electronic effects at the SAM/organic semiconductor interface. Kelvin probe force microscopy (KPFM) measurements, together with the electrical characteristics of the TFTs, help to obtain a better insight into the electronic phenomena at the interfaces.

In Chapter 7, the focus is shifted to some of the supplementary aspects of DNTT transistors, such as the shelf-life stability and the implementation of high-performance DNTT TFTs on two different types of flexible substrates.

2. Theory

2.1 Organic semiconductors

Organic semiconductors have received major attention in the recent years as the heart of organic electronics. Organic materials are distinguished from their inorganic counterparts by a weaker intermolecular bonding mechanism. The main components of organic molecules are carbon and hydrogen, although additionally, they can consist of oxygen, nitrogen, sulfur or fluorine.[4] Organic semiconductors can be categorized into two classes of materials, namely **polymers** and light-weight molecular materials (also referred to as **small molecules**).[5] The two classes of organic semiconductors are usually distinguished by their dimensions and processing techniques. Polymer films can be prepared using solution-processing techniques, such as spin-coating, inkjet printing and doctor blading. Thin films of polymers can be easily fabricated on a large scale, but they are usually of amorphous (or semi-crystalline) character, rather than crystalline. Although numerous deposition and post-deposition procedures have been developed to improve the morphology of the solution-processed polymers, the control over the structure and the spatial organization of the molecules in polymer thin-films is still limited. Unlike polymers, which are normally processed from solution, small-molecule semiconductors can also be processed by thermal evaporation from the solid phase in vacuum (sublimation). Sublimation of small-molecule semiconductors permits high control over the growth and the crystalline quality of the films. The order in thin films of small-molecule semiconductors facilitates improved transport properties in organic electronic devices. In addition, the batch-to-batch variation in small-molecules semiconductors is strongly reduced due to the higher purity of the oligomer compounds, which leads to reduced defect densities in the films. In the past few years, a new group of small-molecule semiconductors have been developed which are soluble and therefore offer the possibility of solution-processing for this class of materials. In spite of the large mobilities reported for solution-processed small-molecule semiconductors, vacuum processing has the advantage of being the more environmentally friendly technique. The use of the organic aromatic solvents which are commonly employed for the solution processing of organic semiconductors can be a major threat to the environment. Therefore, vacuum-processed small-molecules, which have been the subject to extensive research in the last years, were selected as the more desirable choice and employed throughout this thesis.

2.1.1 Conjugation in organic semiconductors

Both of the two major classes of organic semiconductors (*i.e.*, polymers and small molecules) are characterized by the presence of conjugation. Conjugation in organic semiconductors, which originates from the sp^2 –hybridization of carbon atoms, is responsible for most optical and electronic properties of organic semiconductors. The sp^2 –hybridization takes place via combining the 2s, $2p_x$ and $2p_y$ orbitals into three $2sp^2$ hybrid orbitals. The remaining $2p_z$ atomic orbital points out of the plane of the sp^2 orbitals, as shown in **Figure 2.1**-a. In order to clarify the concept of conjugation, the structure of the classic example benzene (C_6H_6) will be discussed as the building block of many organic semiconductors (**Figure 2.1**-b). The hybrid sp^2 orbitals of each carbon atom contribute to the formation of two σ bonds to the neighboring carbon atoms, forming the molecular backbone of the molecule. The overlap of the remaining p_z orbitals via π bonds leads to the formation of π-molecular orbitals.

Such an arrangement results in alternating single and double bonds across the π-orbital system within the benzene molecule. This gives rise to delocalization of π electrons (bonding orbital and π* antibonding orbitals) that can support mobile charge carriers. In other words, the electrons which contribute to π bonds do not belong to only two neighboring carbon atoms, but are rather delocalized across all the adjacent aligned carbon atoms.

In benzene the bonding π-molecular orbitals, which are doubly occupied, form the highest occupied molecular orbital (HOMO) and the antibonding π*-molecular orbitals (unoccupied) form the lowest unoccupied molecular orbital (LUMO), as shown in **Figure 2.1**-c. The energy splitting between the bonding and antibonding orbitals (π-π*) is defined as the optical energy gap E_g. Since the π-π* energy splitting (~1.5 eV to 3 eV) is much smaller than the σ-σ* energy difference, the π-π* transitions are the lowest excitations which occur in conjugated molecules, and therefore, the π bonds determine the electronic properties of conjugated molecules.[5]
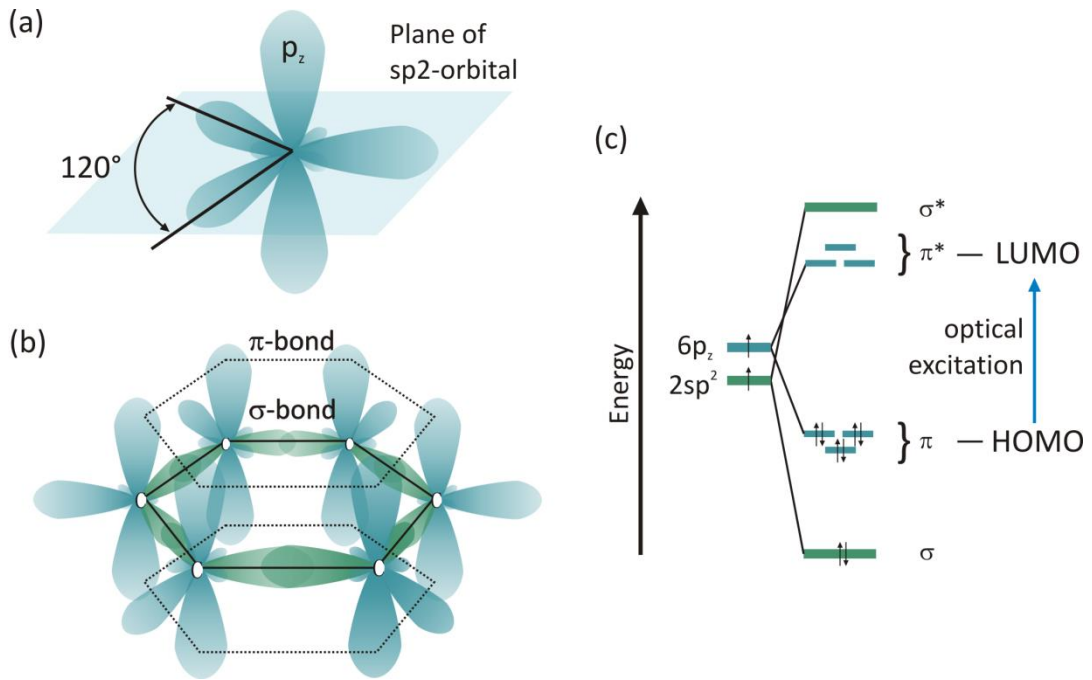
Figure 2.1: Schematic of the sp²-hybridization (a) The structure of benzene and the formation of σ- and π-bonds in benzene (b). (c) Energy level diagram illustrating the bonding and antibonding molecular orbitals in benzene.

2.1.2 Charge-carrier transport in organic semiconductors

One of the important properties of organic semiconductors is their ability to transport the electronic charge which is described by a very important parameter known as charge carrier mobility.

The electric current through a material j is determined by the charge carrier density n and the carrier drift velocity v_D (given by $v_D = \mu \cdot E$, μ being the mobility and E the electric field)

$$j = e \cdot n \cdot v_D = e \cdot n \cdot \mu \cdot E \qquad\qquad \text{Equation 2.1}$$

where e is the elementary charge. In semiconductors, where both j and n can depend on the applied field, the relation between the charge carrier density and mobility, unlike in metals, is not necessarily linear.

The electrical conductivity σ determines how well a material accommodates the transport of an electronic charge. The electrical conductivity is the ratio of the current density to the electric field and can be extracted as shown below:

$$\sigma = e \cdot \mu \cdot n \qquad\qquad \text{Equation 2.2}$$

In all three types of organic electronic devices, namely organic light-emitting diodes (OLEDs), organic photovoltaic cells (OPVCs) and organic field-effect transistors (OFETs),[*] the device efficiency is related to charge carrier transport and hence to the charge carrier mobility.

Imbalanced charge carrier transport in OLEDs can lead to the accumulation of excess charges inside the device or a decrease in charge recombination, both resulting in an efficiency loss.[6] In OPVCs, where the charge carriers are generated by the absorption of photons, the number of charges which contribute to the photocurrent is governed by charge separation and recombination processes, which go hand in hand with mobility. In other words, the balance of the mobility of the two different classes of charge carriers can influence the efficiency of the charge separation and charge transport towards the respective electrodes.

In OFETs, high switching speeds, which are important for the application of organic transistors in integrated circuits, are only realistic upon achieving high charge carrier mobilities. Therefore, understanding the charge transport mechanism in organic semiconductors can hold the key to the realization of high performance organic electronic devices. Given the broad range of charge carrier mobilities reported for organic semiconductors (10^{-6} cm^2/Vs to 10^1 cm^2/Vs),[7] it has been largely debated whether charge carrier transport in organic semiconductors is band transport (as is the case for inorganic semiconductors) or occurs via hopping between localized states, or whether another mechanism is involved. In the following paragraphs, a comparison between the band and hopping transport plus two other proposed models is provided.

Band transport model

The band transport model is a well-established model used to explain the optical and electrical properties of metals and inorganic semiconductors.[8] The delocalized electronic states and wide bands in inorganic semiconductors allow for band transport. Similarly, in the case of pure and highly ordered organic molecular crystals, the band transport model can be applied when the temperature is sufficiently low.[9]

Hopping transport model

In the presence of significant disorder (at elevated temperatures) or when the material lacks long-range order (due to non-crystallinity) band transport is not possible. In this situation the electron wavefunctions become localized and charge carriers move by

---

[*] Find a brief introduction on the devices in Section 2.1.4.

hopping from one localized electronic state to another. The density of states (DOS) of the localized sites in this case is assumed to be Gaussian-like.[10] The hopping transport model holds best for disordered inorganic materials[11] and organic semiconductors in their amorphous phase.[12]

Multiple trapping and release model

The multiple trapping and release model (MTR), which is commonly used for amorphous silicon TFTs,[11] has also been considered to explain the transport in polycrystalline organic transistors.[12] This model is based on the assumption that the localized electronic states are distributed in energy close to a delocalized transport band in which efficient charge transport is possible.[3] The broadening of the DOS is much smaller in this case compared to that in amorphous organic materials. The charges in the transport band can be captured by trapping sites, such as impurities, defects and grain boundaries, and scatter back to localized states.

Despite the various transport models that were discussed above and more sophisticated models, which were not mentioned because of their more complicated aspects, the charge transport mechanisms in organic semiconductors are not fully understood to date.

One way to determine, which of the above-mentioned transport models are applicable to a certain system, is to take the different physical assumptions and approximations associated with each model into consideration. For example, different models are intended for different ranges of charge carrier densities, meaning not all models are valid for the charge carrier densities observed in organic semiconductor devices. Additionally, different measurement conditions, such as different temperatures and applied electric fields should be taken into account before associating a certain model with the system. Therefore, another way to determine the suitable transport model, is the temperature-dependent study of the charge carrier mobility. All things considered, MTR can often be employed to explain charge carrier transport mechanisms in organic semiconductors.

2.1.3   Optical gap *vs.* transport gap in organic semiconductors

As explained earlier, unlike inorganic semiconductors, energy levels in organic semiconductors consist of localized states. As a consequence optical excitations are also localized in the form of an electron-hole pair known as exciton. The exciton motion in organic solar cells is described best by hopping-based diffusion processes.[13] The optical gap is the energy required to excite an electron from the HOMO into the LUMO. This still does not include the exciton binding energy, *i.e.*, dissociation of the exciton. The transport gap, however, is the threshold for creating electrons and holes that are not bound

together. Therefore, the transport gap in organic molecules is larger than the optical gap with the difference being the exciton binding energy that in some cases can be a significant fraction of the HOMO-LUMO gap.[14]

2.1.4 Organic Semiconductor Devices

OLEDs: In OLEDs light is created by injection of holes and electrons from the contacts and their emissive recombination. Low energetic barriers at the interface between the organic semiconductor and both of the contacts are crucial to obtain a balanced flow of electrons and holes in the device.

OPVCs: An OPVC, in which organic semiconductors are used as the active light-harvesting materials, is a device which converts light into electronic charges. OPVCs will be discussed in detail in Section 2.2.

OFETs: An OFET is a transistor with an organic semiconducting active layer that consists of 3 terminals namely source, drain and gate. In OFETs, as in inorganic FETs, the charge carrier density between the source and drain contacts is controlled by an electric field created by the applied gate-source voltage. High-performance OFETs can be obtained by using ordered organic semiconductor (crystalline or polycrystalline) layers in addition to suitable geometries and insulating materials as the gate dielectric. Organic thin-film transistors (OTFTs) are OFETs that are distinguished by their active organic layer that consists of a thin film of a semiconductor layer deposited onto a substrate. The possibility of depositing the active layer onto various substrates makes the OTFT configuration a desirable choice. Further details on OFETs and OTFTs can be found in Section 2.3.

2.1.5 Processing of organic semiconductors

A large number of methods are employed to process organic semiconductors for the application in optoelectronic and electronic devices; mainly based on solution or vapor phase processing. Vapor phase deposition or sublimation in vacuum is a common method for the deposition of low-molecular weight organic molecules and it has been used throughout this thesis for the thin-film growth of our small-molecule organic semiconductors.

The control parameters of the growth kinetics and, therby, of the film morphology are the temperature of the substrate during growth and the deposition rate. The structure of a film deposited by sublimation is also strongly influenced by the nature and the structure

of the substrate onto which the organic film is deposited. For many applications it is desirable to grow films that are as far as possible, free of defects, such as pinholes, which could lead to short-circuits in electronic devices. The optimal growth conditions for the formation of a defect-free thin film from a certain organic semiconductor molecule must be determined empirically.[15]

In the following, the three organic semiconductor molecules used in this thesis are briefly introduced.

2.1.6 Diindenoperylene (DIP)

DIP is a small planar molecule with the chemical formula $C_{32}H_{16}$ (Figure 2.2), which was first synthesized by von Braun in 1934.[16] DIP has a HOMO energy of 5.35 eV, a transport gap of 2.55 eV, and an optical gap of 2.1 eV.[17,18] DIP molecules sublimed onto SiO_2/Si substrates tend to stack in an upright arrangement with a herringbone structure. The height of upright-standing DIP molecules on SiO_2/Si substrates has been reported to be around 1.7 nm.[19–21] Thin films of DIP are known to exhibit a high degree of crystalline order and favorable structural and hole-transport properties.[22,23]
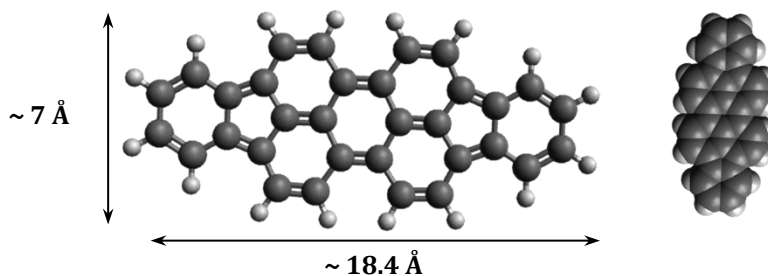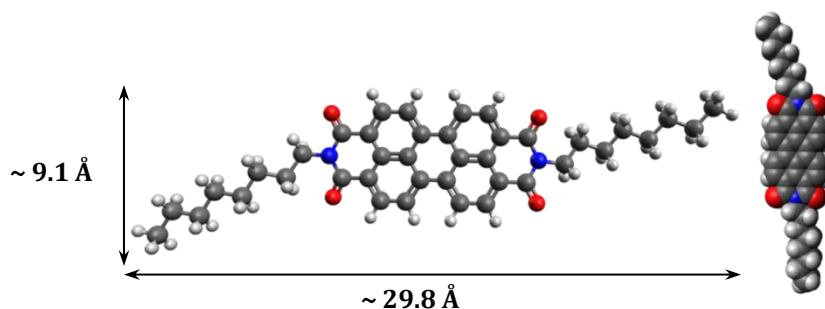

Figure 2.2: The 2D and 3D depiction of the structure of DIP ($C_{32}H_{16}$) molecule: dark-grey spheres correspond to carbon atoms, bright-grey spheres to hydrogen atoms. The arrows mark the lateral dimensions of the molecule.[19]

2.1.7 N,N′-dioctyl-3,4,9,10-perylene tetracarboxylic diimide (PTCDI-C₈)

PTCDI-C_8 is a small molecule from the perylene diimide family with the chemical formula $C_{40}H_{42}N_2O_4$ (Figure 2.3). The HOMO of PTCDI-C_8 has an energy of 6.3 eV[24] and the estimated electron affinity (the difference between the energy of the LUMO and the vacuum level) is ~3.9 eV.[24,25] PTCDI-C_8 molecules sublimed onto SiO_2/Si substrates arrange in a π-π stacking manner leading to the formation of thin films with an outstanding degree of crystalline order. The height of the upright-standing molecules has been reported to be around 2.2 nm, which corresponds to a tilted orientation of PTCDI-C_8, in agreement with X-ray diffraction studies.[26,27] PTCDI-C_8 and other similar derivatives of the perylene diimide family are considered among the most promising materials for the

fabrication of high-mobility n-channel organic field effect transistors.[28–31] PTCDI-C$_8$ has also been used as the acceptor material in solar cells in combination with pentacene.[32]

Figure 2.3: The 2D and 3D depiction of the structure of PTCDI-C$_8$ (C$_{40}$H$_{42}$N$_2$O$_4$) molecule: dark-grey spheres represent carbon atoms, bright-grey spheres hydrogen, blue spheres nitrogen and red spheres oxygen. The arrows mark the lateral dimensions of the molecule.[26]

2.1.8 Dinaphtho[2,3-b:2´,3´-f]thieno[3,2-b]thiophene (DNTT)

DNTT is a small planar molecule with the chemical formula C$_{22}$H$_{12}$S$_2$ (depicted in Figure 2.4), which was introduced by Yamamoto and Takimiya in 2007.[33] DNTT has a relatively low-lying HOMO level (~5.4 eV) and a large HOMO-LUMO energy gap (~3 eV), allowing the utilization of DNTT for organic transistors.[33] Vacuum-deposited DNTT molecules adopt a standing-up configuration and pack in a herringbone arrangement with a reported layer spacing of 16.21 Å in the c-direction.[34] The long axis of the DNTT molecules in such DNTT thin films is approximately perpendicular to the substrate surface, facilitating an efficient π-orbital overlap between neighboring molecules. DNTT is an attractive choice for the realization of high-mobility and air-stable organic TFTs.[35] The thin-film microstructure of this semiconductor favors large hole mobilities well above 1 cm^2/Vs.
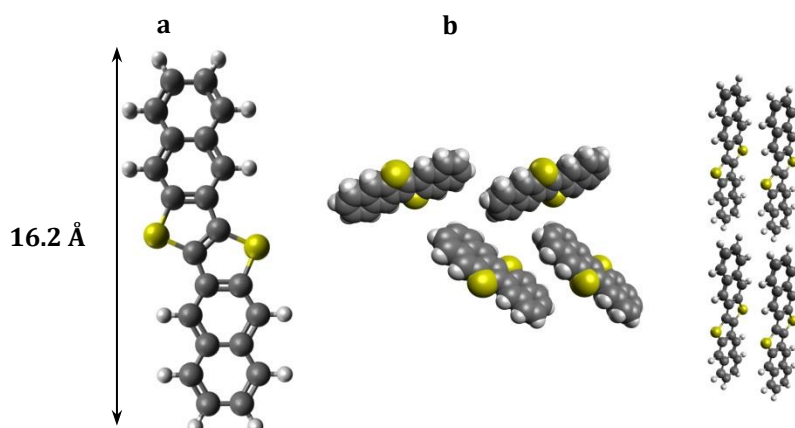
Figure 2.4: a) The 2D depiction of the structure of DNTT (C22H12S2) molecule: dark-grey spheres correspond to carbon atoms, bright-grey spheres to hydrogen atoms and yellow spheres to sulfur. b) Herringbone packing of the DNTT molecules in the ab-plane (left) and in the bc-plane (right) adapted from [34].

2.2   Theory of organic solar cells

Several processes are involved in the operation of organic solar cells which result in the conversion of light into electrical power.

In the following chapter, an overview of the basic physics of organic solar cells, including the donor/acceptor heterojunction concept, is provided. Subsequently, a detailed explanation of the role of the **charge transfer state**, an intermediate state of a bound electron-hole pair at the donor/acceptor interface, is presented. The chapter is closed by a brief remark on the current-voltage characteristics of a typical solar cell.

2.2.1   Working principle of inorganic solar cells

A solar cell is a diode which transforms solar radiation into electrical power. The commercially available and widely used conventional inorganic solar cells are fabricated from inorganic semiconductors, such as silicon. Silicon cells are based on the pin junction concept. A pin junction is formed by three differently-doped regions: a p-doped region (with holes as majority carriers), an n-doped region (with electrons as majority carriers) and an intrinsic or undoped region sandwiched between the p and n regions. A photovoltage is generated across this junction where the p-doped side is depleted of free holes and the n-doped side is depleted of free electrons. In this region, which is called the *depletion zone* (or the space-charge region), an electric field is created and the electrons and holes, generated by the absorption of light, are driven by this electric field towards their respective electrodes. The solar cell performance is described in terms of efficiency, which is the ratio of the output electrical power to the incoming solar radiation power. Commercially available silicon solar cells reach an efficiency of about 20%.[36] Since the absorption of light in silicon is rather low, thick layers are required to enhance the light absorption. As a result, inorganic solar cells are rigid plates and therefore, mechanical flexibility cannot be achieved.

2.2.2   Working principle of organic solar cells

The unique properties of organic semiconductors make them a desirable choice over inorganic solar cells in several aspects. As a result of the weak intermolecular forces in organic semiconductors various manufacturing techniques, such as spin coating and printing techniques, are possible at room temperature, holding the promise of easy and inexpensive fabrication.[37] Organic molecules typically have large absorption coefficients in the visible region of the radiation spectrum, implying that the organic semiconductor

layer in a solar cell does not have to be thick in order to absorb the photons from the solar spectrum.[38] Besides, organic chemistry allows for tailor-making of new organic materials with the desired electrical and optical properties.

As explained briefly, the working mechanism of inorganic solar cells is the electrostatic potential drop at the interface between a p- and an n-doped semiconductor that leads to the separation of the electrons and holes and their transportation to the respective electrodes. In organic solar cells, however, there may not be a built-in electrostatic potential to separate the electrons and the holes that are coulombically bound together. These bound electron-hole pairs are called exciton. In addition, as a consequence of stronger localization of the wave function, smaller dielectric constants and weaker screening of opposite charges, the exciton binding energies in organic solar cells (in the order of several hundred meV) are much larger than the ones in inorganic solar cells (in the order of kT ≈ 25 meV).[38] Therefore, a special strategy is required to separate the electron-hole pairs and make the carriers available for charge collection before they recombine.

### 2.2.3   Optical excitations in organic semiconductors

As a consequence of the weak electronic delocalization, the optical properties of organic molecules are similar to those of a free molecule, *i.e.*, a molecule in the gas phase or in solution.[5,14]

The two basic optical transitions in an organic semiconductor, namely absorption and recombination,[*] can be understood in terms of transitions between two displaced harmonic oscillators.[14] As can be seen in Figure 2.5, the potential energies of the electronic ground state S_0 and the first excited state S_1 are illustrated by two parabolas with a displacement, which is the result of the optical excitation. Each electronic state consists of different vibrational energy levels. In organic semiconductors, S_0 corresponds to the HOMO and S_1 to the LUMO. When a photon is absorbed, an electron makes a transition from the lowest vibronic level of the ground state to one of the vibronic levels of the excited state (absorption). The selection rule for the transitions between the vibronic levels is described by the Franck-Condon principle[39,40] and the allowed transitions are indicated by the vertical arrows in **Figure 2.5**. In order for the S_0-S_1 transition to take place, the incoming photon needs to have an energy above the (optical) band gap. The molecule will relax to the lowest vibronic level of the excited state by a non-radiative

---

[*] Recombination is the reaction of an electron with a hole, in which the charges are annihilated.[38]

process followed by a radiative relaxation to one of the vibronic levels of the electronic ground state (emission). As a result of the non-radiative relaxation within the excited state and the energy loss in the emission process, the emission spectrum exhibits a red shift (a shift towards longer wavelengths) with respect to the absorption spectrum, which is known as the Stokes shift.[41]
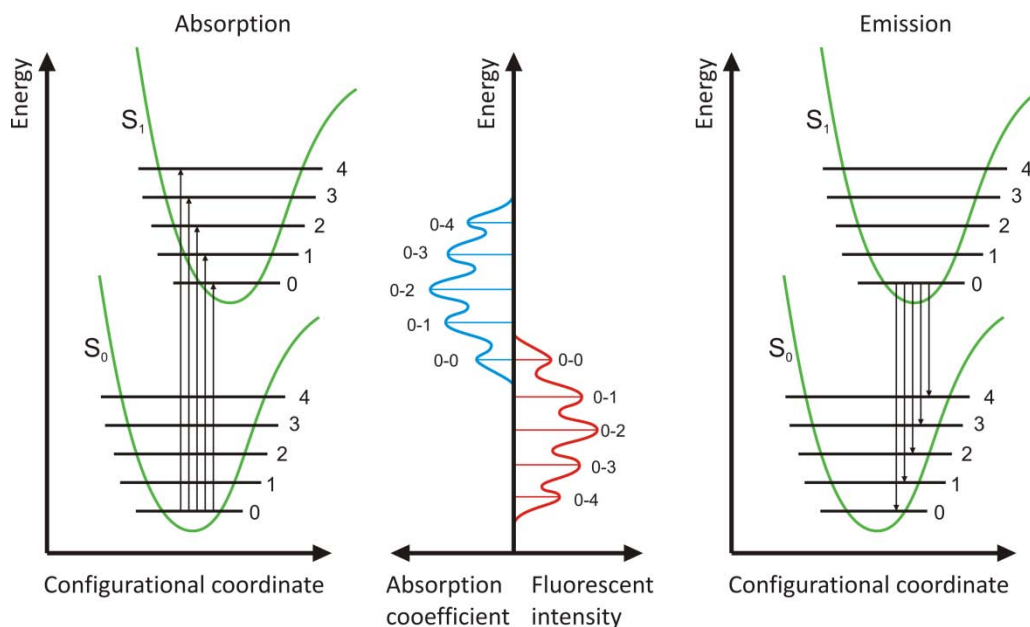

Figure 2.5: Sketch depicting the Frank-Condon principle. Potential energy curves of the ground state (S_0) and excited state (S_1). The vertical arrows indicate optical transitions from S_0 to the vibrational levels of S_1 in case of absorption (left) and from S_1 to vibrational levels of S_0 in case of emission (right). The curves in the middle illustrate the resulting absorption and emission. Figure adapted from reference [41].

2.2.4 The donor/acceptor concept

The first organic solar cells built by Kallmann et al. in 1959 consisted of one layer of an organic semiconductor sandwiched between two metal electrodes with different work functions. Absorption of light resulted in the creation of the strongly bound Frenkel excitons which had to be efficiently split in order to finally generate a photo current. The typical lifetime of molecular excitons is on the order of nanoseconds,[42,43] which leads to a diffusion length of a few nanometers. Since the exciton diffusion length ($\sim$ 5-7 nm)[39,44] is usually much smaller than the thickness of the organic layer, the excitons do not efficiently dissociate at the interface and diffuse to the electrodes, but recombine instead.

The implementation of a second layer of a different material in the photoactive layer lead to the next generation of OPVs, known as bi-layer heterojunctions, which consists of two layers of organic materials. This was the idea behind the donor/acceptor heterojunction concept pioneered by Tang in 1986, who used two different materials which were stacked in layers.[45] The photoactive layer of the organic donor/acceptor solar cell consists of two semiconducting materials, one functioning as an electron donor (D) and the other as an electron acceptor (A). The so-called donor material is often made out of a hole-conducting small-molecule semiconductor. When the solar cell is illuminated, the donor material absorbs the photons and an excited state is created. Absorption by the acceptor is usually small compared to that by the donor. As mentioned earlier, an energetic driving force (a strong electric field) is required to separate the bound electron-hole pair (exciton) into free charge carriers. This field is usually provided by the energy offset of the molecular orbitals of D and A materials at the interface. It means that it has to be energetically favorable for the electrons to be transferred to the LUMO of the acceptor and for the holes to be transferred to the HOMO of the donor material.

If an exciton diffuses to the D/A interface during its lifetime to undergo the charge transfer process, then it can dissociate into free charge carriers. Subsequently, free charges are extracted by selective contacts. **Figure 2.6** shows the individual processes involved in the working of a heterojunction solar cell using a simple schematic.
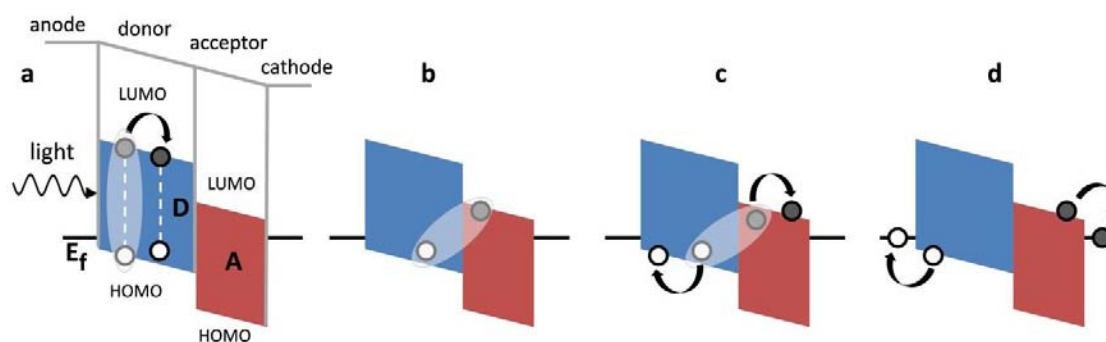
Figure 2.6: Individual processes from light absorption to charge extraction in a heterojunction solar cell: a simplified energy diagram of the HOMO and LUMO levels of donor (D) and acceptor (A) sandwiched between the Fermi levels (E_f) of the electrodes. (a) Absorption of light in the donor material, exciton generation and exciton diffusion towards the D/A interface. (b) Exciton dissociation by electron transfer to the LUMO of the acceptor. (c) Separation of coulombically-bound electron-hole pair. (d) Charge carrier collection at the electrodes.

One problem, however, is that the D/A interface is restricted in area and that the distance from most of the regions of the donor and acceptor material to this interface is much greater than the diffusion length of most excitons. This implies that a significant fraction of

excitons recombine before reaching the D/A interface and dissociating into free charges. Therefore, the interface between the donor and the acceptor materials, which is the key to a more efficient charge separation, needs to be maximized. Following this idea, Yu et al. developed the so-called bulk heterojunction by intermixing the two organic components and thereby increasing the interfacial area significantly.[46]
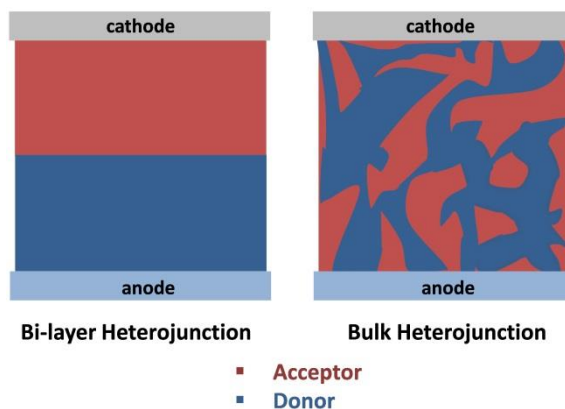
Figure 2.7: The schematic cross-section of a bi-layer heretrojunction solar cell and a bulk heterojunction solar cell

2.2.5 Interfacial charge transfer state and charge separation

It has been demonstrated that the properties of the interface between the donor and the acceptor material, known as the D/A heterointerface, plays a crucial role for the photovoltaic performance by determining the character of the charge transfer states. The charge transfer (CT) state is an intermediate step between exciton dissociation and the free charge generation, in which the bound electron-hole pair resides at the D/A heterointerface (the hole resides in the donor and the electron in the acceptor) while they remain bound by Coulomb attraction.[2,47–49] There are three main scenarios that can happen to CT excitons: the best case scenario for solar cells is when the electron-hole pair separates into two free charges and, therefore, can be turned into an electric current. When this is not the case, the electron-hole pair decays by either a radiative recombination leading to the emission of a photon or a non-radiative decay resulting in phonon creation.

The CT state has been proved crucial for the performance of solar cells by determining the solar cell parameters (briefly introduced in the next section), such as short circuit current as well as setting the maximum achievable open-circuit voltage.[47]

Interfacial CT states can be most easily detected if they are emissive. Photoluminescence (PL) measurements can be done to observe and study the character of such emissive CT

states. Emissive CT state are characterized by a broad, red-emitting PL peak[5] that is detected only in the blend and cannot be assigned to the PL from either the donor or the acceptor in their pristine phase.[2]

Although the investigations on the nature of CT states and their direct correlation with the device performance are ongoing, several studies have shown that the properties of the CT state are determined to a great extent by the properties of the D/A interface, such as the wave-function overlap across the interface. Therefore, the morphology of the heterointerface, and more precisely, the arrangement of the D and A materials at the interface are expected to strongly influence the mechanisms of exciton dissociation and recombination.[2,50] Chapter 4 is devoted to the assessment of the impact of the relative molecular orientation at D/A heterointerfaces on the exciton dissociation.

2.2.6 Solar cells parameters

The key parameters which determine the performance of solar cells, such as the open-circuit voltage V_{oc}, the short-circuit current I_{sc}, the fill factor FF and the power conversion efficiency η, are discussed in the following. **Figure 2.8** illustrates the current-voltage characteristics of a solar cell in the dark and under illumination. As can be seen, the I-V curve in the dark shows the typical diode behavior. The curve under illumination, however, is shifted with respect to the dark curve as a consequence of the charge photo-generation.
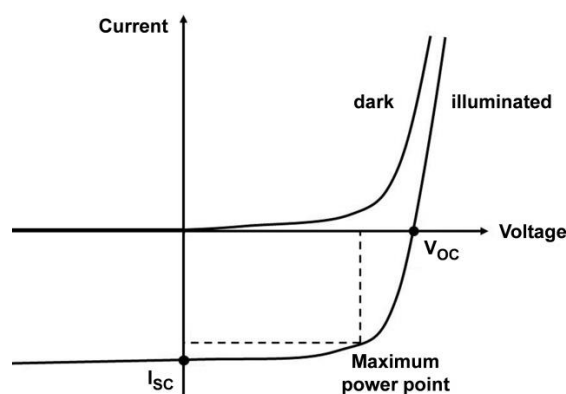
Figure 2.8: I-V curves of a typical solar cell with and without illumination. In the illuminated curve the solar cell parameters are marked.

Open circuit voltage

The open circuit voltage V_{oc} is defined as the voltage at which no current flows through the solar cell under illumination. The energy values of the LUMO of the acceptor and the HOMO of the donor have been shown to determine the V_{OC}.[51]

Short circuit current

The short circuit current I_{sc} is the current which flows through the solar cell device in the absence of an external voltage (for V = 0). I_{SC} is purely based on photo-generated charge carriers. Therefore, the number of photons which are absorbed by the solar cell determines the magnitude of the I_{sc}.

Fill factor

The point where the highest possible power output can be achieved is known as the maximum power point (P_{max}) as marked in **Figure 2.8**. The maximum power point MPP has the corresponding voltage V_{MPP} and the current I_{MPP}. The fill factor FF, which is defined with the following equation, has a linear relation with the overall efficiency of a solar cell device:

$$FF = \frac{P_{max}}{V_{OC} \cdot I_{SC}} = \frac{V_{MPP} \cdot I_{MPP}}{V_{OC} \cdot I_{SC}}$$
<div align="right">Equation 2.3</div>

Power conversion efficiency

The power conversion efficiency η, which is a measure of how efficiently the solar energy is converted into electrical energy, is the ratio between the maximum power P_{max} and the input light power P_L, as shown in the following equation:

$$\eta = \frac{P_{max}}{P_L} = \frac{V_{OC} \cdot I_{SC}}{J_0} FF$$
<div align="right">Equation 2.4</div>

where J_0 is the intensity of the incident light. As can be seen in Equation 2.4 an efficient solar cell requires the optimization of the open circuit voltage, the short-circuit current as well the fill factor all at the same time.

2.3 Theory of organic thin-film transistors

This section consists of a broad outline of the working principle of organic thin-film transistors. Initially, an overview of the general concepts associated with the operation of organic TFTs is provided. The section is followed by introducing the relevant terminology and important TFT parameters. In particular, we focus on the main topic of the transistor part of this thesis, which is the threshold voltage. The section introducing the importance and implications of the threshold voltage is completed by an overview of several different threshold-voltage extraction methods and their implementation in (DNTT) TFTs. Furthermore, two different classes of gate-dielectric materials (inorganic and organic) for TFTs are introduced. The chapter is wrapped up by a brief review of the two most prominent interfaces involved in TFTs, namely the gate-dielectric/organic semiconductor interface and the metal contacts/organic semiconductor interface.

2.3.1 General concepts of thin-film transistors

Field-effect transistors (FETs) are the fundamental building block of integrated circuits. FETs can be built according to various architectures such as metal-insulator-semiconductor FET (MISFET). Thin-film transistors (TFTs) are MISFETs that operate in the accumulation mode.[52]

TFTs have three terminals known as the gate, source and the drain electrodes. The gate electrode forms a parallel plate capacitor together with a thin layer of a semiconducting material and the two plates are separated by an insulator material known as the gate dielectric. The source and drain contacts are used to inject charges into (or retrieve charges from) the semiconducting film.[3]

By applying a potential to the gate electrode (V_{GS}), an electric field is created, which modulates the resistance at the interface between the semiconducting active material and the gate dielectric. In other words, the basic idea behind the operation of TFTs is charging of the capacitor which results in the accumulation of the charge carriers that form a conductive path between the source and the drain electrodes, known as the *channel*. Upon the formation of the conductive channel, applying a voltage between the source and drain contacts (V_{DS}) can result in a drain current (I_D) through the device. In an ideal TFT there would be no current flowing elsewhere in the device (the leakage current). However, in reality a small gate leakage current (I_G) through the gate dielectric often flows during the device operation.

TFTs can adopt various configurations depending on the respective arrangement of the three electrodes. **Figure 2.9** depicts the cross-section of a top-contact, bottom-gate TFT. The distance between the source and the drain electrode is called the *channel length* L, and the lateral dimensions of the source and drain contacts determine the *channel width* W, as marked in **Figure 2.9**.
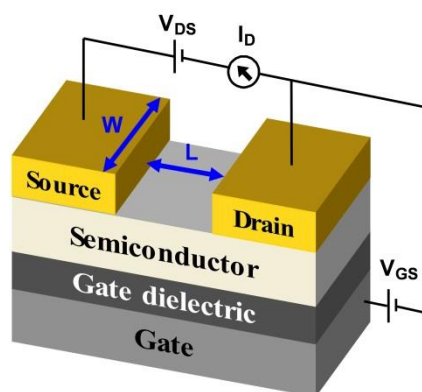
Figure 2.9: The schematic 3D cross-section of a top-contact, bottom-gate TFT, illustrating the source, drain and gate electrodes. The channel length L and the channel width W are marked with the blue arrows in the figure.

2.3.2 P-channel organic field-effect transistors

The polarity of organic transistors depends on the relative position of the Fermi level of the contact metal and the HOMO and LUMO levels of the organic semiconductor. When a voltage is applied to the gate, charges of opposite polarity are induced in the semiconductor. Charge injection from the metal contacts into the organic semiconductor is possible when the energy barrier height between the Fermi level of the metal and the transport energy level of the organic semiconductor is low. An organic semiconductor will result in a p-channel transistor when hole injection is easier than electron injection, which is the case when the HOMO level is closer to the Fermi level of the metal contact compared to the LUMO level. The opposite case occurs for an n-channel organic semiconductor. The focus of this thesis is on DNTT-based p-channel organic TFTs. **Figure 2.10** shows the respective positions of the energy levels of DNTT[33] and the Fermi level of gold. According to this scheme, p-channel behavior is expected in DNTT TFTs, *i.e.*, no current flow upon the application of a positive potential to the gate, and current flow when a negative gate potential is applied. Since the Fermi level of gold is close to the HOMO level, holes can be injected from gold into the DNTT HOMO level (**Figure 2.10**). At this point the conducting channel is formed and a current can flow in the channel by applying a bias voltage to the drain contact.[53]
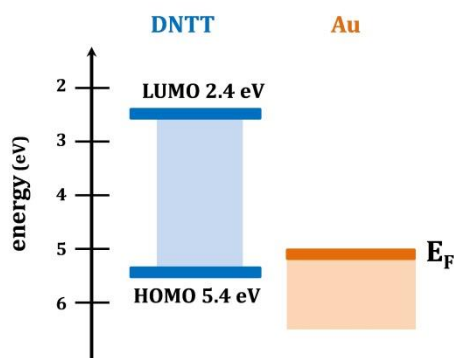
Figure 2.10: Energy scheme of a gold-DNTT interface

2.3.3 Transistor measurements

As explained in the last section, TFTs are operated upon applying a voltage between the gate and the source (V_{GS}), and a second independent voltage between the drain and the source (V_{DS}). The outcome is an electric current from the source to the drain contact through the semiconductor (I_D). TFTs are typically characterized by two different current-voltage characteristics known as *transfer* and *output characteristics*.

Transfer characteristics

In the transfer characteristics, the drain current (I_D) is plotted over a range of gate-source voltages (V_{GS}). In order to obtain the transfer characteristics, V_{DS} is kept constant while V_{GS} is swept between some suitable values. Transfer curves are usually shown on a logarithmic scale in order to determine some important parameters for the performance of the TFTs, namely the turn-on voltage V_{on}, the on/off current ratio and the subthreshold slope of the transistor. Other parameters, like the charge carrier mobility in the channel and the threshold voltage, can also be extracted from the transfer curves. A brief introduction to these parameters will be provided in the following sections.

Hysteresis in transfer curves

The hysteresis phenomenon is often observed in the transfer curves during sweeps of the gate-source voltage V_{GS}, and it appears as an offset between drain currents I_D measured during the forward and backward sweeps of the gate-source voltage V_{GS}. Hysteresis can be put to good use in memory devices. However, it is not a desirable phenomenon in standard integrated circuits and should be avoided. Hysteresis in organic TFTs can originate from various effects, but often it is associated with charge-carrier trapping in shallow traps in the semiconductor close to the dielectric interface or with the presence of mobile charge carriers and mobile ions in the semiconductor or in the gate dielectric.[54]

Output characteristics

As the name suggests, output characteristics represent an output quantity, the drain current I_D, plotted against the drain-source voltage V_{DS}. For the output characteristics, V_{GS} is kept constant while I_D is being measured as a function of V_{Ds}. The output characteristics contain mostly qualitative information about the behavior of the device, rather than providing quantitative measures of the TFT parameters. Charge-carrier mobilities, however, can be extracted from the output curves, providing the threshold voltage values are already known from the transfer curves.

2.3.4 Terminology

Field-effect mobility

The charge-carrier mobility μ measured using a field-effect transistor is called field-effect mobility. The field-effect mobility can be inferred from the transfer characteristics measurement in the saturation regime or in the linear regime, which will be explained in section 2.3.6.

Threshold voltage

In nature, no element is completely pure and even after purification, there are always *defects* present in the crystal structure of any element. These defects, which are of chemical or structural nature, result in the presence of free charges (electrons, holes or ions) in the material. In other words, in FETs, due to the presence of fixed charges in the gate oxide and the mismatch between the work function of the gate metal and the semiconductor, the transistor cannot be switched at zero bias (V_{GS} = 0 V). The threshold voltage (V_{th}) is the voltage necessary to offset the defect-induced free charges. In organic TFTs, V_{th} is defined as the gate-source voltage required to fill all the trap states in the gate dielectric or at the gate dielectric/semiconductor interface.[55]

V_{th} is often used in association with the turn-on voltage V_{on}, being the voltage at which there is no band bending in the semiconductor and flat-band condition has been achieved.[56] V_{on} can be easily determined from the transfer characteristics plotted on a logarithmic scale, being the voltage at which the drain current starts to increase exponentially. Extraction of V_{th}, however, is not as simple, and several methods have been developed for the estimation of V_{th}. The most common methods for the extraction of V_{th} will be discussed in section 2.3.5.

Linear and saturation regions

As already mentioned, the TFT operates like a parallel plate capacitor, *i.e.*, applying a voltage between the gate and the source will result in the induction of an equal number of charges, but of opposite sign, in both plates (the gate and the semiconductor layer). The formation of the conducting channel then takes place on the semiconductor side of the capacitor. When the applied drain-source voltage is low, the drain current follows Ohm's law, meaning that it is proportional to both the drain-source voltage and the gate-source voltage. This is called the linear region, and is the case when $V_{GS} - V_{th} > V_{DS}$. As the drain-source voltage approaches the gate-source voltage, the voltage drop at the drain decreases until it falls down to zero and a pinch-off of the channel occurs, which means no more charges are accumulated at the drain any longer. At this point, the drain current becomes independent of the drain-source voltage, a regime which is called the saturation region and occurs when $V_{GS} - V_{th} = V_{DS}$. The drain current in the linear and saturation regions can be quantified using the equations below which are valid based on the two following assumptions:[3,53]

1. The *gradual channel approximation*, that is, the variation of the electrical field along the channel, is much smaller than that perpendicular to the channel (which implies that the distance between the source and drain contacts is much larger than the thickness of the gate insulator)
2. The mobility µ is constant.

$$I_{D,lin} = \frac{\mu \cdot C_{diel} \cdot W}{L}\left[(V_{GS} - V_{th}) \cdot V_{DS} - \frac{1}{2}V_{DS}^2\right] \qquad \text{Equation 2.5}$$

$$I_{D,sat} = \frac{\mu \cdot C_{diel} \cdot W}{2L}(V_{GS} - V_{th})^2 \qquad \text{Equation 2.6}$$

where C_{diel} is the capacitance per unit area of the gate dielectric.

An extensive description of the operation of organic field-effect transistors can be found in several text books and reviews.[3,52,53,57]

On/off current ratio

The on/off current ratio is defined as the ratio between the drain current in the on-state and the drain current in the off-state. The TFT is in the off-state when $|V_{GS}| < |V_{on}|$, and the off-state current is measured in the transfer curve. Normally, low off-currents are desirable, and therefore the on/off current ratio should be as large as possible. In organic TFTs made with pentacene, on/off current ratios as large as of 10^8 have been obtained.[58,59]

Subthreshold swing

The subthreshold region, as marked in **Figure 2.11**, refers to a region in the transfer curve plotted on a logarithmic scale, where the drain current exhibits an almost linear behavior. The inverse slope of the transfer curve in the subthreshold region is called the subthreshold swing *S*, given by the Equation 2.7. This parameter gives information about how much voltage is required to increase the drain current directly above the on-state current. Since low operating voltages are always of high interest, steep subthreshold swings are desired.

$$S = \frac{dV_{GS}}{d(\log I_D)}$$ Equation 2.7

At room temperature, the minimum of S for conventional inorganic metal-oxide-semiconductor field-effect transistors (MOSFETs) is 60 mV/decade.[8] In single-crystal pentacene FETs, S values as low as 300 mV/decade have been reported.[60]
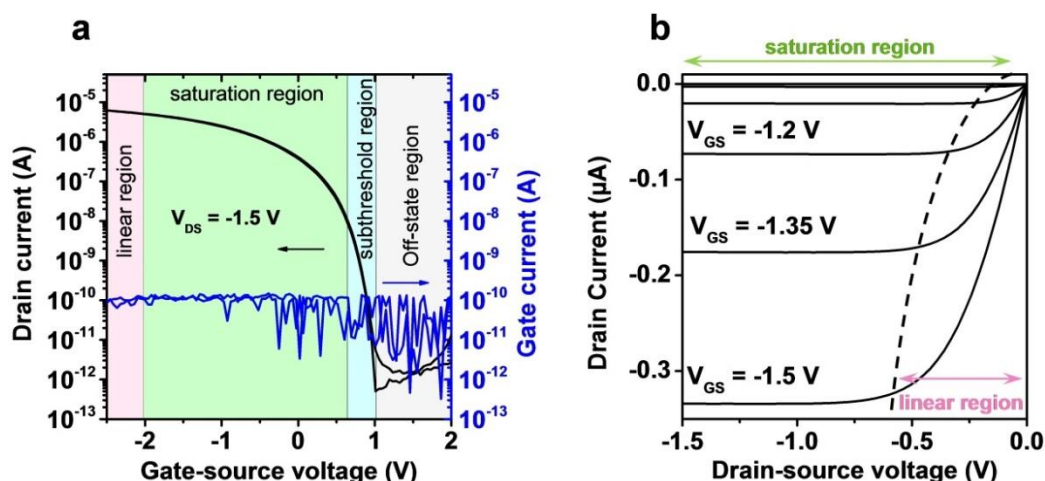
Figure 2.11: Transfer characteristics (a) and output characteristics (b) of a p-channel organic TFT. Different operation regions are marked.

Contact resistance

In previous years, extensive research has been devoted to the minimization of the contact resistance in organic TFTs.[31,61–63] Ideally, the drain current of a transistor is determined solely by the properties of the channel. However, in reality, the presence of parasitic resistances at the source and drain contacts can disrupt the performance of the transistor. This undesired parasitic resistance, known as *contact resistance*, limits the current through the device and the switching speed in integrated circuits. The details of the implications and the measurements of the contact resistance are out of the scope of this thesis.

2.3.5 Threshold voltage extraction methods

In the following, some of the widely-used methods of the extraction of V_{th} in MOSFETs according to the literature[64,65,66] are shown. These methods can be implemented in organic TFTs as well. The different methods have been compared by applying all of them to the transfer characteristic of p-channel organic TFTs fabricated in our laboratory. In the linear regime the TFTs are operated by applying V_{Ds} = -0.1 V and in the saturation regime V_{Ds} = -1.5 V.

Extrapolation in the linear region (ELR)

One of the most widely-used methods for the extraction of V_{th} is the ELR method. In this method, which is employed in the transfer characteristics in the linear regime, V_{th} is estimated by the linear extrapolation of the drain current at its maximum slope point to the intersection with the V_{GS} axis. **Figure 2.12** illustrates the implementation of the ELR method for a p-channel TFT with a channel length of 100 μm which results in a $V_{th, lin}$ value of 0.58 V.

Extrapolation in the saturation region (ESR)

The concept behind the ESR method is similar to the one of the ELR method with a small difference of using the $I_D^{0.5}$–V_{GS} curve in this case instead of the I_D–V_{GS} curve. This dissimilarity comes from the difference between the linear drain current and the saturation drain current. The ESR method determines the threshold voltage from the V_{GS} axis intercept of the $I_{D,sat}^{0.5}$–V_{GS} characteristics linearly extrapolated at its maximum slope as shown in **Figure 2.12** (b). The value of $V_{th, sat}$ in this case is 0.63 V. In this thesis, ELR and ESR are utilized to extract the V_{th}.
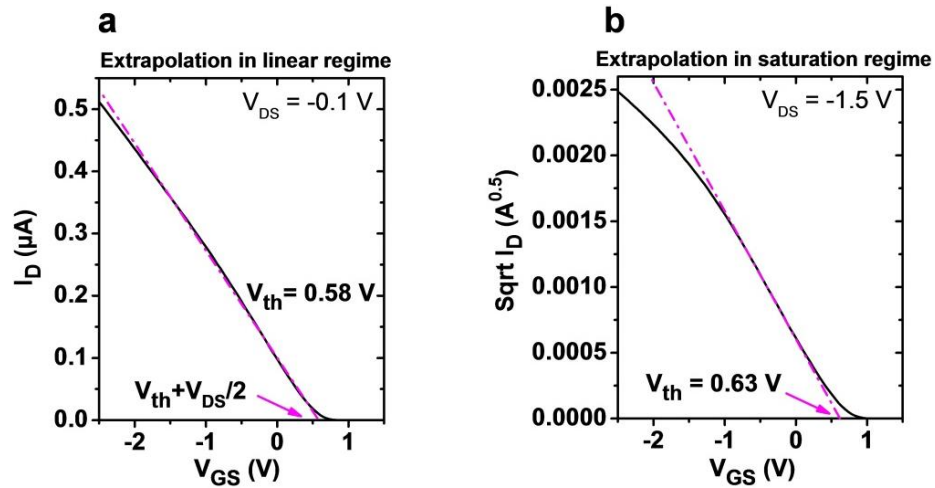
Figure 2.12: (a) ELR method and (b) ESR method implemented on the transfer characteristics of a p-channel organic TFT.

Constant current method

V_{th} in this method is defined as the gate-source voltage for a certain drain current. **Figure 2.13** is an illustration of the implementation of the constant current method in the linear regime of the TFT operation, which shows that for a constant current of 10 nA, $V_{th, lin}$= 0.58 V. While it is a very simple method to use, it has the disadvantage of being strongly dependent on the chosen value of the drain current.
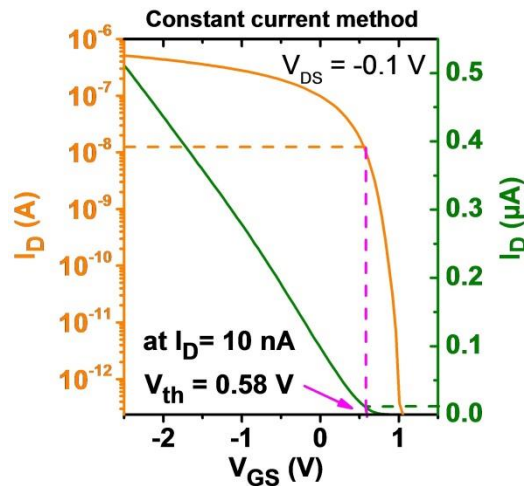
Figure 2.13: Constant current method implemented on the transfer characteristics of a p-channel organic TFT device measured in the linear regime (at V_D = −100 mV).

Second derivative method (SD)

In the SD method, introduced by Wong *et al.*,[64] V_{th} is determined as the gate-source voltage, at which the second derivative of the drain current (the first derivative of the

transconductance*) has its maximum. This method can be employed in transfer curves both in the linear regime and in the saturation regime. The graphical representation of the SD method employed in the linear regime is illustrated in **Figure 2.14**.
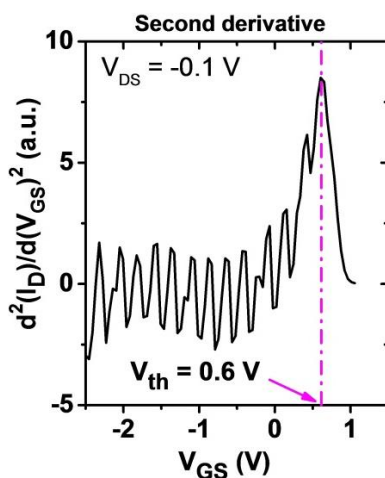
Figure 2.14: SD method implemented on the $d^2I_D/d(V_{GS})^2$ – V_{GS} curve of a p-channel organic TFT device measured in the linear regime (at $V_D = -100$ mV).

2.3.6 Field-effect mobility extraction

Based on Equation 2.5 and Equation 2.6, field-effect mobilities can be extracted simply from the slope of the linear fits to the I_D–V_{GS} curve in the linear regime and to the $I_D^{0.5}$–V_{GS} in the saturation regime, as illustrated in **Figure 2.12**. Often in the literature and also throughout this thesis, the parameter field-effect mobility refers to the effective mobility, which includes the effect of the contact resistance.

2.3.7 Dielectric materials for organic transistors

Historically, amorphous silicon dioxide SiO_2 was the most-commonly used dielectric material in the early organic transistors, due to its good quality and ease of processing by conventional microelectronic technology. The use of SiO_2, however, imposes several limitations on the performance of organic transistors. For example, the relatively low dielectric constant of SiO_2 (k = 3.9)[67] can result in undesirably large operating voltages. Also, amorphous SiO_2 is known to have a large density of electronic defects and a large amount of OH groups on its surface that act as electron traps.[68] Therefore, alternative organic and inorganic dielectric materials have been developed to account for the shortcomings of SiO_2 as the gate dielectric in transistors.

---

* The transconductance curve can be obtained by differentiating the drain current I_D with respect to the gate-source voltage V_{GS}.

Inorganic dielectrics

In addition to the widely-used SiO_2 as the gate dielectric,[69,70] alternative inorganic dielectrics with high dielectric constant (known as high-k materials) have been employed, because of their ability to induce lower operating voltages. Al_2O_3, with a dielectric constant of $k = 9$, which is over 2 times the dielectric constant of SiO_2, has been extensively used as the gate dielectric in organic TFTs in recent years.[71–78] The main reason is that Al_2O_3 forms a good electrical and thermodynamically stable interface with Si, which is a common choice as the gate material. Therefore, Al_2O_3 (formed by atomic-layer deposition or ALD) has been used as the gate oxide throughout this thesis.

Some of the most-commonly used high-k inorganic dielectrics are TaO_2[79–83], ZrO_2[84,85] and TiO_2[86,87], which have k values of 22 for TaO_2, 25 for ZrO_2 and 80 for TiO_2.[67] Although high-k inorganic oxides seem promising for the realization of low-voltage devices, like SiO_2 they suffer from reactivity with water and/or surface defects that can act as traps for the charge carriers.

Ultrathin organic dielectrics

A promising approach to overcome the reactivity and surface defects of the gate oxides is the passivation of the oxide surface with a self-assembled monolayer (SAM). SAMs are ordered monomolecular assemblies that spontaneously form by the chemical adsorption of a molecule onto a solid surface.[88] SAMs are usually formed either in solution, or they are deposited from the gas phase by vapor deposition techniques. Initially, SAMs were explored as ultrathin dielectrics in organic TFTs for the realization of low-voltage organic transistors.[89] Additionally, SAMs can be used in combination with the inorganic oxides as a passivation layer to reduce the density of charge traps at the oxide/SAM interface and, thereby, provide an enhancement of the charge-carrier field-effect mobility for both p-channel[90] and n-channel organic TFTs.[91] SAMs have also been used as the active organic layer in ultra-thin organic TFTs (SAMFETs).[92,93]

The beneficial effects of the passivation of the gate-oxide surface with a SAM in organic TFTs have been reported for a variety of oxides, including SiO_2,[94–97] Al_2O_3,[98–101] HfO_2,[102–105] ZrO_2,[106–108] $ZrTiO_x$[109] and TiO_2,[86,110] and for a variety of SAMs, most notably alkylsilane SAMs[95,111] and alkylphosphonic acid SAMs.[112-114] Typically it is observed that the treatment of the gate-oxide surface with SAMs in organic TFTs would result in (one or more of) the following effects in the device with the SAM treatment compared to the control devices without the SAM treatment: increase in the field-effect mobility, increase

in the I_{on}/I_{off} current ratio, reduction in the subthreshold slope, alteration of the polarity of the majority charge carrier type, and a shift in the threshold voltage (threshold-voltage shift).[115]

The term threshold-voltage shift may also be used in association with the gate-bias induced shifting of the transfer curves. Usually stressing the transistors upon applying a gate bias leads to a modification of the threshold voltage due to the filling of shallow traps with mobile charges at the semiconductor/insulator interface.[116] The shallow traps are usually filled after a few quick sweeps, resulting in a stabilized and more reliable threshold voltage value. Within the scope of this thesis, the term threshold-voltage shift refers to the SAM-induced shift in the threshold voltage.

The threshold-voltage shift is considered one of the most important consequences of functionalizing the gate-oxide surface of organic TFTs with SAMs. The reason behind the threshold-voltage shift induced by the presence of the SAMs has been under debate for over a decade, and despite the fact that several hypotheses have been suggested the community has not come to an agreement on a general mechanism that explains the different aspects of this effect. However, often the change in V_{th} by SAMs has been attributed to the dipolar character of the molecules forming SAMs.

In the present thesis, we have put the focus on the implications of employing SAMs as a surface treatment on an inorganic gate oxide, namely Al_2O_3. In Chapter 6 we present a detailed study on the phenomena associated with the usage of SAMs as a passivation layer on Al_2O_3 gate oxides in TFTs, mainly the threshold-voltage shift.

2.3.8 Gate-dielectric/semiconductor interface

Considerable research in the organic electronics community has been devoted to the impact of the dielectric/semiconductor interface on the performance of the bottom-gate organic transistors, where the semiconductor is deposited directly on top of the gate dielectric. Since charge transport in organic TFTs usually takes place in the first few monolayers of the active organic layer,[117-119] a profound understanding of the interface between the organic semiconductor and the SAM in the gate dielectric is critical for tailoring devices with the desired performance. The phenomena that occur at this interface may be of electrical or morphological nature. The morphological and the electrical aspects of the interfacial effects at the SAM/organic semiconductor interface will be explained in the following.

Morphology

The morphology of the organic semiconductor as the active layer has been shown to play an important role in the performance of TFTs with various organic semiconductors. The dielectric surface, onto which the organic semiconductor is deposited, is known to influence the molecular packing, the degree of crystallinity and in some cases even the molecular orientation. Orientational and structural changes in the morphology of $F_{16}CuPc$ thin films have been demonstrated in the first few layers compared to the subsequent layers as a result of the interaction with the dielectric at the semiconductor/dielectric interface.[120]

One major component which determines the semiconductor growth and hence the final thin-film morphology is the surface energy of the gate dielectric onto which the semiconductor is deposited. The effect of the alteration of the semiconductor morphology on the device performance as a result of different dielectric surface energies has been shown in pentacene TFTs by Yang *et al.* where the mobility of TFTs with a low-surface-energy polymeric gate dielectric appears to be larger by a factor of five, compared to the devices with a high-surface energy dielectric.[121] Modification of the surface energy of the gate oxide can also be achieved by the oxide-surface treatment with SAMs. This alteration of the surface energy results in a change of the thin-film structure (crystallinity, grain size and the density of the grain boundaries) of the polycrystalline organic semiconductor film.[90] Different growth modes have also been reported near the SAM-coated gate-oxide surface compared to growth in the bulk.[98,119] The enhanced field-effect mobilities in TFTs with SAM-treated gate oxides have often been associated with improvements in the thin-film morphology of the organic semiconductor layer, presumably induced by the surface energy of the SAM-functionalized oxide surfaces.[96]

Electrical effects

In addition to the morphological modification of the semiconductor, SAMs can cause electrical modifications to the semiconductor. For example, one of the most frequently discussed electrical effects associated with SAMs is attributed to the dipolar character of the molecules forming the SAMs. The molecular dipole moment of the SAMs creates an electrostatic potential (V_{SAM}) that can lead to charge accumulation in the semiconductor, where the nature of the charges depends on the direction of the dipole.[122] There could also be an electrostatic interaction between the SAM head group (electron-withdrawing or -donating head groups) and the semiconductor that shifts the transport levels of the semiconductor.[123] This effect, which results in either hole or electron accumulation

depending on the SAM/semiconductor combination, will be discussed further in Chapter 06 as *electronic coupling*. Another significant electrical effect associated with the dipolar SAMs in the adjacent organic semiconductor is a broadening of the distribution of charge transport states in the semiconductor.[3,123] This broadening of the density of states, which is a result of the dipole field of the SAM, may reduce or increase the charge-carrier mobility, depending on the nature of the semiconductor.

2.3.9 Electrodes/semiconductor interface

In addition to the gate-dielectric/ organic semiconductor interface, the interface between the charge-carrier injecting contacts and the semiconductor is determinant to the performance of the transistors. Metallic contacts are the most common type of contacts employed in organic TFTs and known to form good ohmic contacts suitable for the charge-carrier injection. Traditionally, it is assumed that the properties of the metallic contact/ organic semiconductor interface are based on the work function of the metal and the energy levels of the organic semiconductor, namely HOMO and LUMO. In small molecules, however, energy alignment can be controlled by a density of states (DOS) at the interface.[3] Electronic alignment at the metallic contact/ organic semiconductor interface is not the only prominent aspect regarding the carrier injection, and the morphology of the semiconductor in the vicinity of the contacts also plays a major role in controlling the charge injection.

2.3.10 Section remarks

In Section 2.3, we have reviewed the general concepts of organic TFTs with the main emphasis on the threshold voltage and the role of the two prominent interfaces in the operation of the organic TFTs. The insulator/ organic semiconductor interface is crucial, because it is, where the conducting channel is formed and the charge transport takes place. Therefore, the quality of this interface, which consists of the gate dielectric and the semiconductor, determines the charge transport in organic TFTs. Recently, the use of ultrathin organic insulating layers (SAMs) has been shown to improve the quality of this interface drastically. The metallic contacts/ organic semiconductor interface is also important, because at this interface the charge transfer into and out of the organic semiconductor takes place. In the following experimental chapters, the importance of the gate-dielectric/ organic semiconductor interface will be further demonstrated.

3. Methods and experimental details

3.1   Preparation of Substrates and self-assembled monolayers

The templates used for the DIP/ PTCDI-C$_8$ systems (Chapter 4) were heavily doped Si (p- or n-doped) substrates with a layer of native oxide. The substrates were cleaned by successive sonication in acetone and ethanol (five minutes per sonication).

Various substrates have been employed as templates for the DNTT thin films. The heavily p-doped silicon substrates for the samples in Chapter 5 and Chapter 7 had a layer of thermally grown silicon dioxide (SiO$_2$), and an additional layer of aluminum oxide (Al$_2$O$_3$) was deposited (Si/SiO$_2$/Al$_2$O$_3$; 100 nm SiO$_2$ + 30 nm or 8 nm of Al$_2$O$_3$) by atomic layer deposition (ALD) at a substrate temperature of 250 °C.

The experiments in Chapter 6 were performed using heavily p-doped silicon substrates (without thermally grown SiO$_2$), onto which a layer of Al$_2$O$_3$ with a thickness of 5 nm, 10 nm, 50 nm, 100 nm or 200 nm was deposited by ALD. For the substrate with the thinnest Al$_2$O$_3$ (5 nm), the native SiO$_2$ was removed in dilute hydrofluoric acid prior to the Al$_2$O$_3$ deposition.

Additionally, in Chapter 7 experiments on two types of flexible polymeric substrates are presented, namely a 125 μm thick flexible polyethylene naphthalate film (PEN; kindly provided by William A. MacDonald, DuPont Teijin Films, Wilton, UK) and a polyimide/benzocyclobutene film (20 μm polyimide + 5 μm BCB fabricated by spin coating onto a Si wafer; kindly fabricated by Ms. Golzar Alavi (at the Institute for Microelectronics Stuttgart, Germany). Unlike the aluminum oxide layer that is used as the gate oxide in the TFTs nearly always throughout the whole thesis, in Chapter 7 a thin layer of AlO$_x$ is formed by oxygen plasma treatment.

Prior to the treatment of the aluminum oxide surfaces with the SAMs, independent of the SAM treatment method and the nature of the aluminum oxide, the surfaces are exposed to an oxygen plasma in order to create a high density of hydroxyl groups on the Al$_2$O$_3$ and AlO$_x$ surfaces and also to improve the quality and increase the thickness of the native AlO$_x$ layer. This process, which is referred to as the oxygen *plasma treatment*, is carried out in an OXFORD reactive ion etch system (treatment parameters: 30 s, 10 mTorr, 30 sccm (standard cubic centimeters per minute) O$_2$, 200 W).

33

Four different phosphonic acids were employed: n-octylphosphonic acid (HC$_8$-PA; kindly provided by Helena Gleskova, University of Strathclyde, Glasgow, UK), n-tetradecylphosphonic acid (HC$_{14}$-PA; purchased from PCI Synthesis, Newburyport, MA, USA), n-octadecylphosphonic acid (HC$_{18}$-PA; purchased from PCI Synthesis) and 12,12,13,13,14,14,15,15,16,16,17,17,18,18,18-pentadecylfluoro-octadecylphosphonic acid (FC$_{18}$-PA; kindly provided by Matthias Schlörholz).[35]

For most of the experiments, the Al$_2$O$_3$-coated silicon substrates were immersed into a 2-propanol solution of either the alkyl- or the fluoroalkylphosphonic acid (dip-coating method), resulting in a uniform coverage of the Al$_2$O$_3$ surface with one particular SAM. After the SAM treatment by dip coating, the standard procedure for stabilizing the monolayers was carried out as follows: the substrates were rinsed in pure 2-propanol, blow-dried with nitrogen, and baked on a hotplate at a temperature of 100 °C for 10 minutes.[124]

In Chapter 5, the microcontact printing method is compared to dip coating, where a polydimethylsiloxane (PDMS) stamp (with a surface area of ~2 cm^2) has been used for the microcontact printing of the FC$_{18}$-PA SAM onto a Si/SiO$_2$/Al$_2$O$_3$ substrate directly after plasma treatment followed by the standard procedure of rinsing and annealing to stabilize the SAMs. Subsequent to the treatment of the aluminum oxide with the SAMs, static contact angle measurements with either water or a non-polar liquid (hexadecane; Chapter 6), are performed, using a Kruess contact angle measurement system, to confirm the quality of the monolayers.

For some of the KPFM measurements described in Chapter 6, we also prepared substrates on which the HC$_{18}$-PA SAM and the FC$_{18}$-PA SAMs are both present. To pattern substrates with both SAMs, we employed a combination of microcontact printing and dip coating. In the first step, a pattern of the FC$_{18}$-PA SAM was produced on the Al$_2$O$_3$ surface by microcontact printing using a PDMS stamp directly after plasma treatment.[124–126] Those areas of the substrate not covered by the FC$_{18}$-PA SAM were then filled with the HC$_{18}$-PA SAM by immersing the substrate into a 2-propanol solution of the HC$_{18}$-PA. The substrates were then rinsed and annealed as explained above.

3.2 Sample preparation

### 3.2.1 Thermal evaporation of organic materials

In the experiments described in Chapter 4, prior to the deposition of the organic semiconductors, the substrates were annealed at a temperature of 300 °C (20 min) upon transferring to the UHV system (pressure $\approx 10^{-8}$ mbar) to remove water molecules (and other pollutants) from the surface. The deposition of DIP and PTCDI-C_8 was done by sublimation in a UHV chamber consisting of a sample heating stage, up to three evaporation sources and a quartz microbalance system to monitor the thickness of the sublimed material in the chamber. For the formation of the DIP and PTCDI-C_8 sub-monolayer samples, ~1 nm of DIP was deposited onto substrates consisting of native SiO2/Si at a substrate temperature of 80 °C and ~ 1 nm of PTCDI-C_8 at a substrate temperature of 130 °C. The fabrication of the heterojunction architectures with DIP and PTCDI-C_8 was done in two sublimation steps, each with only one species of the molecules, and the temperature of the substrate was optimized for each growth accordingly.

The deposition of DNTT (purchased from Sigma Aldrich) thin films discussed in Chapter 5, 6 and 7 was done in a high-vacuum system (pressure $\approx 10^{-6}$ mbar). Partial layers of DNTT were fabricated by the deposition of a 2-nm-thick layer, and the nominal thickness of the DNTT layers used in TFTs was 25 nm. DNTT was deposited at a substrate temperature of 60 °C during the deposition, onto either bare Al_2O_3 surfaces or onto Al_2O_3 decorated with SAMs at a moderate deposition rate of 0.03 nm/s. A higher deposition rate of 0.3 nm/s and a lower deposition rate of 0.007 nm/s were also employed to study the effect of the deposition rate on the morphology of DNTT and on the performance of DNTT TFTs.

In Chapter 7, the SAM treatment using sublimation in vacuum was carried out as follows. Prior to the sublimation of HC$_8$-PA molecules, the Al_2O_3 surface was treated with oxygen plasma and the substrate was mounted directly after the plasma treatment in the vacuum evaporation system. As soon as the vacuum reached the desired pressure (10^{-6} mbar), a thin layer of the HC$_8$-PA (a few monolayers of the molecules ~ 10 nm) at a deposition rate of 0.04 nm/s to 0.05 nm/s was deposited onto the substrate at room temperature. In order to obtain an ordered array of the HC$_8$-PA SAM on the substrate, the substrate was annealed in the vacuum evaporation system (pressure ~ 10^{-6} mbar) at 160 °C for 210 minutes following a procedure optimized recently by Gupta *et al.*.[127]

3.2.2   Fabrication of the TFTs

Subsequent to the deposition of a DNTT layer, the fabrication of bottom-gate, top-contact (inverted staggered) TFTs was completed by the deposition of gold source and drain contacts by thermal evaporation in vacuum through a polyimide shadow mask onto the surface of the organic semiconductor layer. In all the TFTs, highly doped silicon served both as the substrates and a global gate. The gate dielectric (SAM+ Al_2O_3 and/or SiO_2) and the DNTT were also global layers. Only the top gold contacts were patterned, leading to the formation of TFTs with a channel length of 100 μm and a channel width of 200 μm. The TFTs on flexible substrates in Chapter 7 were also fabricated in the inverted staggered configuration using a set of four polyimide shadow masks (fabricated by CADiLAC Laser, Hilpoltstein, Germany). First, a 30 nm thick layer of aluminum was deposited by thermal evaporation in vacuum and patterned through the a mask to define the gate electrodes of all transistors. Next, the aluminum was briefly exposed to the oxygen plasma to create an aluminum oxide (AlO_x) layer with a thickness of about 3.6 nm, followed by immersing the substrate into a 2-propanol solution the phosphonic acid to form the hybrid AlO_x/SAM gate dielectrics. A 25-nm-thick layer of DNTT was then sublimed through another mask. Finally, 30 nm of gold was patterned using the final mask to define the top source and drain contacts with a channel length of 30 μm and a channel width of 100 μm. Different steps of the fabrication of the TFTs are shown in **Figure 3.1** schematically.
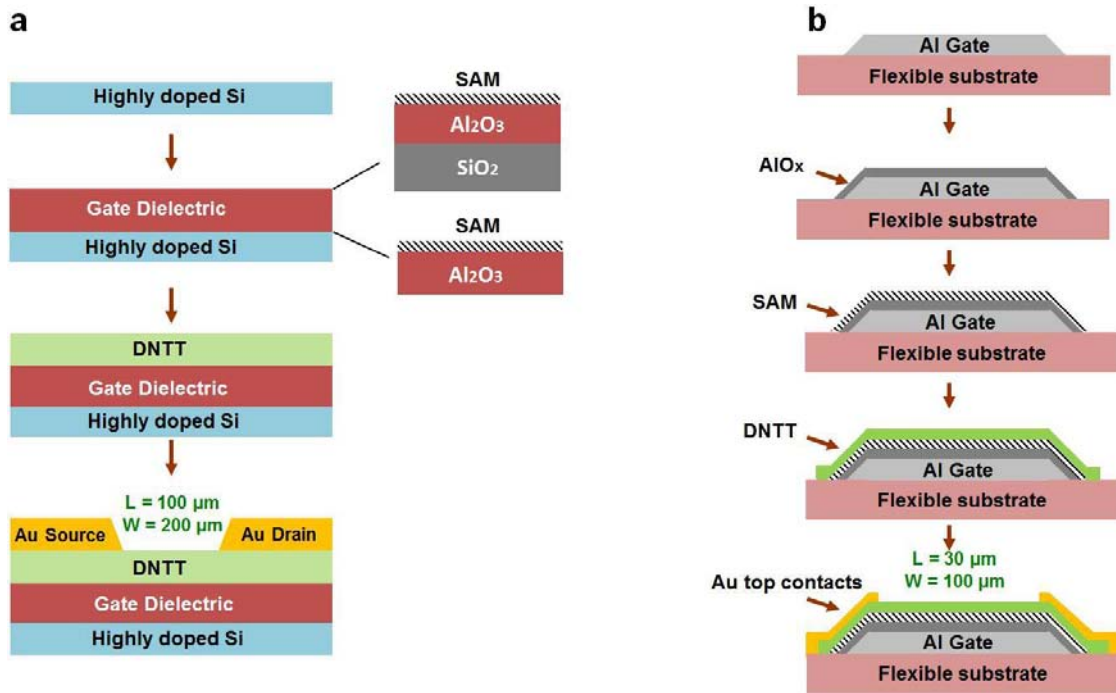
Figure 3.1: Schematic figures of the fabrication steps of TFTs prepared with a) global gate, gate dielectric and semiconductor layers on silicon substrates and b) patterned layers using 3 shadow masks on flexible substrates.

3.3 Characterization techniques

3.3.1 Atomic force microscopy

Atomic force microscopy (AFM) is one of the foremost tools for imaging the topographical features of a surface with lateral resolutions on the nanometer scale. AFM can be employed to investigate any type of sample, whether conductive or non-conductive, *e.g.* metals, graphene, polymers, ceramics, composites *etc..* AFM uses a mechanical probe (a small tip on a cantilever) to scan the sample surface, using the forces between the tip and the surface for the feedback mechanism. The most common AFMs use a laser beam deflection system where the laser beam is reflected from the back of a reflective cantilever attached to the tip. This reflected beam reaches a position-sensitive photodiode in a circular configuration that consists of four quadrants. Prior to the measurement, the calibration of the AFM is done in a way to position the reflected laser beam in the center of the photodiode. When the AFM tip is scanning the sample, the tip senses the attractive or repulsive forces from the sample. As a result, there will be a deflection of the cantilever leading to an offset in the position of the reflected beam from the center of the photodiode. The new position of the reflected beam on the photodiode is then converted into an output signal, which contains information about the height profile of the surface. The working principle of a conventional AFM is shown schematically in **Figure 3.2**.
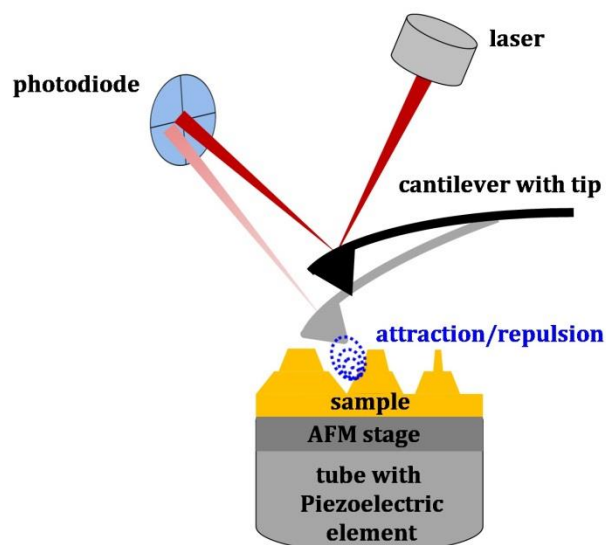
Figure 3.2: Schematic visualization of the working principle of AFM

The two most common AFM modes of operation, known as contact mode and tapping mode (also dynamic mode) follow the same principle as explained above with slight differences that will be explained in the following.

AFM in contact mode

As the AFM tip approaches the surface, different forces are sensed by the tip, which can be of attractive or repulsive character. When the tip-sample distance is large enough, the forces sensed by the tip are negligible. While approaching the surface (the loading process), the tip senses the attractive forces that can be of van der Waals, electrostatic or magnetic nature. At a certain threshold the unloading process takes place and the tip enters the repulsive region of the forces as a result of overlapping electron orbitals according to the Pauli exclusion principle. The different measurement regimes and the force-distance curve during an AFM measurement are shown in **Figure 3.3**.
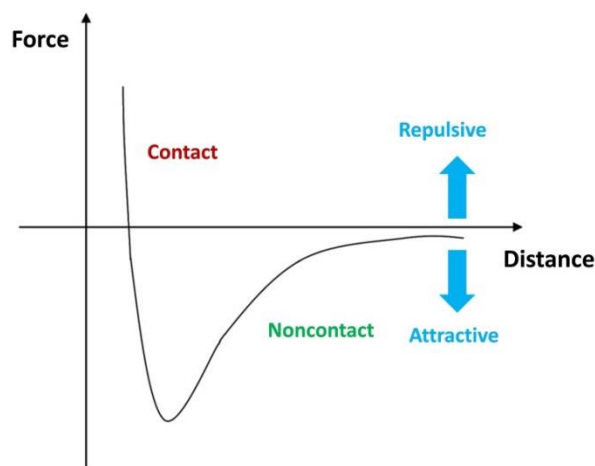
Figure 3.3: Graphical representation of the force-distance curve in an AFM measurement.

Contact mode AFM is performed in the repulsive regime of the force-distance curve where the tip is physically in contact with the surface. Capillary force of a thin water layer is also present under ambient conditions. Contact mode AFM is commonly performed using a constant cantilever force where the deflection of the cantilever is set to a desired value and thereby, topographical features of the surface are recorded. Furthermore, the response of the AFM tip to properties such as the hardness, friction and different surface forces can be analyzed in order to get more insight into the surface properties.

By collecting the data from the trace scans only (in one direction parallel to the sample surface) one can obtain the trace (forward) image and the data from the retrace scans will form the retrace (backward) images. Analysis of frictional forces can be done from the forward and backward images obtained during a lateral force microscopy measurement.

Lateral force microscopy is a method to investigate the forces perpendicular to the cantilever long axis. This technique is used to study the areas of higher and lower friction on the sample by measuring the torsion of the cantilever. The lateral force signal, simultaneously acquired with the topography in contact mode, can "sense" differences in the physicochemical properties and therefore, help distinguish the chemically heterogeneous regions. It is also useful to resolve molecular-periodicity in ordered molecular films. In this thesis, the analysis of the lateral forces is used in Chapter 4 for the characterization of nanostructures of DIP and PTCDI-C_8 molecules.

AFM in dynamic-force mode

Dynamic-force mode AFM (also intermittent-contact mode or tapping mode) is intended to be done above the adsorbed water layer, where the tip operates mostly in the attractive regime of the forces but it also enters the repulsive regime and contacts the surface only briefly during the tapping. Therefore, this method is less destructive compared to contact mode. In this technique the cantilever oscillates at (or slightly below) its resonance frequency ω_0, using a small piezoelectric crystal attached to it, at a large amplitude. As soon as the tip approaches the surface and starts sensing the interactions, its oscillation reduces due to energy loss. The feedback loop in the tapping mode is normally designed to keep the frequency (or the amplitude) of the oscillation constant and it delivers information on the frequency (or the amplitude) and the phase at which the tip is vibrating. As these properties change with the distance from the surface due to the surface-tip interactions, topographical images can be collected. The phase signal can be used to distinguish different species on the surface when they have different phase response to the tip. AFM can also be performed in non-contact mode using an oscillating cantilever in the attractive regime, but never entering the repulsive regime where the tip

touches the surface. AFM in tapping mode has been employed in many of the measurements in this thesis either to reduce the mechanical damage of ultra-thin molecular films or to perform Kelvin probe force microscopy.

Kelvin probe force microscopy

AFM measurements can also be done using electrically-conducting tips. AFM performed in contact mode using a conducting tip, is known as conductive AFM (C-AFM) and is used to obtain current maps of the surface. AFM with a conducting tip can also be performed in dynamic mode to obtain potential maps of the surface. We will focus on the latter, known as Kelvin probe force microscopy (KPFM; also scanning Kelvin probe force microscopy or SKPM), that is one of the essential techniques in the scope of this thesis. The macroscopic Kelvin probe method was developed by Lord Kelvin in 1898.[128] The working principle of the Kelvin probe technique is based on the parallel-plate capacitor concept. In the conventional set up of Lord Kelvin, the sample forms one of the plates of the capacitor while the other plate consists of a known metal which oscillates at a frequency of ω and the two plates are connected in an electrical circuit. The capacitance changes by modulating the distance between the two plates, resulting in an alternating current (AC) in the circuit. The feedback of this system is a direct current (DC) voltage used to nullify the AC-current in the circuit. This voltage corresponds to the contact potential difference (CPD) between the two materials. The KPFM is based on the same idea, with the slight variation that the conducting KPFM tip, with a known work function, acts as the metallic plate of the capacitor (the reference electrode), which is driven to oscillate at its resonance frequency ω_0 by an AC-voltage applied ($V_{AC}(\omega_{AC})$). Unlike the set-up of Lord Kelvin, the controlling parameter in KPFM is the electrostatic force instead of the current. The feedback loop works through applying a voltage to compensate for/minimize the electrostatic interactions between the tip and the sample.

KPFM is performed by scanning in tapping mode and can be implemented through two different modes of operation known as the amplitude-modulation (AM-KPFM) and the frequency-modulation (FM-KPFM) method. In the AM-KPFM the applied DC-voltage is used to nullify the electrostatic interactions by minimizing the amplitude of the mechanical oscillation of the KPFM cantilever at the set AC-frequency. The FM-KPFM, however, minimizes the variation in the frequency shift with respect to ω_0 at the set AC-frequency. [129,130] In both methods, the conventional AFM feedback system is used to map the topography of the surface.

KPFM is an extremely powerful tool that allows for mapping of the topographical and the electronic properties of nanostructures simultaneously with a lateral resolution of a

conventional AFM and the potential resolution of around 10 mV.[130] In addition to mapping the surface potential distribution, this technique can provide quantitative insight into the work function of metals[131] and electrical polarization effects at the surface (interface dipoles)[132] among other applications. Some of the more sophisticated applications of KPFM include the investigations on the performance of optoelectronic and electronic devices such as organic transistors under operation.[133]

AFM experimental details

The AFM data in Chapter 4 were obtained with a commercial instrument from Nanotec Electrónica. KPFM measurements were performed at room temperature in the dark and under illumination using conductive probes (Pt/Cr-coated Si tips) mounted in cantilevers with nominal force constant of ~ 2.8 N/m. Topography and lateral force images were measured in contact mode using AFM probes with nominal force constant of ~ 0.1 N/m. All contact mode measurements were performed with the lowest practicable load (close to pull-off force) to avoid damage of the soft organic layers.

In Chapter 6 and Chapter 7, Contact-mode AFM images were obtained with a Veeco Nanoscope III Multimode in ambient air using soft cantilevers (force constant~ 0.1 N/m). Tapping mode AFM was done using cantilevers with a resonance frequency of ~ 300 kHz. KPFM measurements were carried out in ambient air at room temperature using an Asylum Research Cypher using conducting tips (Ti/Ir-coated with a force constant of 1.7 N/m. The cypher instrument works in *lift mode* consisting of two measurement passes, where in the first pass the topographical data is collected in conventional tapping mode. In the second pass, the tip is *lifted* to a constant height and scans the trajectory of the first pass above the surface. These measurements were performed in the AM-KPFM mode, where a drive amplitude of 1 V and a frequency of 72 kHz (near the nominal resonance frequency of the tip) were used for the electrical tuning of the tip. All the AFM images were analyzed using the WsXM software.[134]

In Chapter 6, for the estimation of the electrostatic potential of the SAMs, the work function of the tip is determined by scanning the surface of freshly cleaved highly-oriented pyrolytic graphite (HOPG) as a reference. The reason is the good and homogenously-distributed electrical conductivity over a large scale due to the crystalline nature of HOPG.[130]

3.3.2 Photoluminescence spectroscopy

Photoluminescence (PL) spectroscopy is a method, in which a substance absorbs light from a monochromatic light source (laser) resulting in the photoexcitation of the photons from the laser followed by a relaxation process and emission of a lower-energy photon. PL spectroscopy is utilized in Chapter 4 to investigate the effect of the relative molecular orientation on the electronic properties of an organic/organic interface. PL measurements in Chapter 4, were kindly carried out by Dr. M. Schmidt (back then at the Material Science Institute of Barcelona, Spain) using a low-intensity green line of an argon laser (2.41 eV or 514 nm) to avoid damage to organic samples. All measurements were performed under nitrogen to reduce the impact of the humidity and to minimize photo-oxidation of the materials. Samples for the PL are prepared as sub-monolayers of one material (DIP or PTCDI-C_8) or mixed films of DIP/PTCDI-C_8 (the two different heterostructure architectures), and they are measured fresh (directly after sublimation).

3.3.3 Ultraviolet photoelectron spectroscopy

Ultraviolet photoelectron (also photoemission) spectroscopy (UPS) is a method used to determine the energetic structure of the occupied electronic states and the position of the occupied levels in solids and at surfaces. This is achieved by shining ultraviolet light on the material that provides enough energy for the emission of bound valence electrons. The kinetic energy of the emitted photoelectrons is measured with a spectrometer with a known work function. With the knowledge of the ultraviolet light energy, the spectrometer's work function, and the measured quantity of the kinetic energy of the photoelectrons, the binding energy can be calculated in the shape of a spectrum. In the binding energy spectrum, the HOMO position can be identified from the low-energy onset that corresponds to the emission of the fastest photoelectrons.[135]

The UPS experiments in Chapter 4 were performed kindly by A. Fernández (back then at the Material Science Institute of Barcelona, Spain) and Dr. G. Sauthier (at the Catalan Institute of Nanoscience and Nanotechnology, Barcelona, Spain) using a SPECS Phoibos 150 hemispherical analyzer with monochromatic HeI radiation (21.22 eV) under ultra-high vacuum. Samples for the UPS were prepared as sub-monolayers of DIP and the two different DIP/PTCDI-C_8 heterostructure architectures deposited onto n-doped silicon substrates with their native oxide. All the samples were measured fresh (directly after sublimation).

3.3.4 Polarized optical microscopy

Polarized light microscopy is a straightforward method to reveal the existence of favorable orientations of crystals. When a sample consists of homogenously-oriented crystallites, it will appear equally bright all over the sample providing the orientation is uniform everywhere. When the crystallites are oriented in different directions, they will exhibit less regular patterns under polarized light. The resolution of best optical microscopes is around 200 nm. Further resolution cannot be achieved through optical microscopes due to the diffraction limit. The characterization can be taken into a more-precise level by means of other tools such as AFM.

Crossed-polarized optical microscopy of the DNTT thin-film presented in Chapter 5 was carried out with a Nikon LV150 polarizing microscope using a 100× objective in ambient air.

3.3.5 Current-voltage measurements

Current-voltage measurements on the TFTs were carried out in ambient air at room temperature under yellow laboratory light, using a Micromanipulator 6200 probe station, low-noise triaxial cables and an Agilent 4156C Semiconductor Parameter Analyzer. For the samples on heavily doped silicon substrates, the silicon served as a common gate electrode. Every measurement was initiated by measuring three transfer curves using a very short integration time in order to obtain a stabilized threshold voltage value. Transfer curves were measured in both forward (on to off) and backward (off to on) directions, and usually the forward curves were used for the extraction of transistor parameters.

3.3.6 Capacitance measurements

The unit-area capacitance of the Al_2O_3/SAM gate dielectrics in Chapter 6 was measured on shadow-mask-patterned Al/Al_2O_3/SAM/Au capacitors with an area of 60 μm × 60 μm for frequencies between 200 Hz to 20 kHz. All measurements were performed in air at room temperature under yellow laboratory light with the same Micromanipulator probe station used for the transistor current-voltage measurements. Other electronic components, such as a Stanford Research Function Generator DS345 (to apply voltages with different frequencies), a low-noise amplifier and a lock-in amplifier are also used in the circuit.

4. Influence of molecular orientation on interfacial charge transfer excitons

Building high-performance OPV devices based on donor/acceptor semiconductors requires a profound understanding of the interface properties of the two organic components such as the wave function overlap across the interface. The properties of the D/A interface has been shown to have a crucial impact on the mechanisms of exciton dissociation and recombination.[2,50]

In this chapter, we address the impact of the relative molecular orientation between donor and acceptor molecules at the D/A heterojunction interface on the exciton dissociation using the two small molecules DIP and PTCDI-C_8.

We start the chapter with a detailed study on the morphology of the polycrystalline DIP and PTCDI-C_8 thin films, deposited onto SiO_2/Si. The substrate of choice throughout the whole chapter is native SiO_2/Si because the thin naturally-grown SiO_2 layer (typically ~ 1.5 nm) decouples electronically the molecules from the Si and allows uniform layered growth of the thin films with the molecules in a nearly upright standing orientation.

The second part of this chapter is devoted to the heterostructures formed by DIP and PTCDI-C_8. Having precise and sufficient control over the sublimation of the two molecules, we were able to fabricate heterojunctions of DIP and PTCDI-C_8 with two different architectures, which exemplify two model interfaces with the π-stacking direction either perpendicular or parallel to the interface. As will become clear in the course of this chapter, such architectures are of significant importance for D/A heterojuctions since the relative orientation of A and D at the interface can influence the efficiency of the wave function overlap and hence modify the charge transfer/charge recombination properties at the D/A interface.

The purpose of this investigation is to highlight the role of the relative molecular orientation on the nature of the physical phenomena occurring at the donor and acceptor interface relevant for the use in organic solar cells.

Aspects related to the morphology of the heterojunctions and charge photogeneration are studied by scanning probe force methods and photoluminescence (PL) spectroscopy. The

occupied energy levels of the heterojunctions have been characterized by ultraviolet photoelectron spectroscopy (UPS).

4.1 DIP submonolayer morphology

Deposition of a sufficiently thin layer of DIP onto SiO_2/Si (substrate temperature 80°C) in vacuum leads to the formation of submonolayer films consisting of isolated islands of DIP. **Figure 4.1** shows the AFM topography and corresponding lateral force signal of DIP islands covering ∼54% of the surface (*i.e.,* 0.54 monolayer (ML)). The measured island height is ∼1.7 nm (see the line profile in **Figure 4.1**), indicating that the DIP molecules stand with their long axis almost perpendicular to the substrate. This observation is in agreement with the standing upright orientation of DIP molecules, which is the favorable growth adopted by DIP in the first layer according to previous studies.[20,21] The lateral force microscopy image shown in **Figure 4.1** indicates that the lateral force on the DIP islands is homogenous and there are no regions where the lateral force on one island differs from the one on the other. The overall lateral force on DIP islands is smaller than the lateral force on the bare regions of the substrate (SiO_2) and, therefore, the DIP island appear darker than their underlying substrate in the lateral force image.
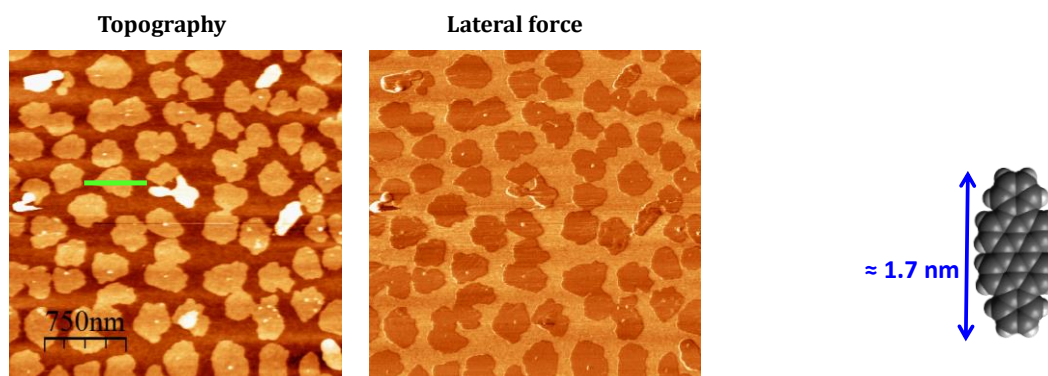
Figure 4.1: AFM topography and lateral force (FW) map of submonolayer isolated islands of DIP grown onto bare SiO_2/Si. The line profile corresponds to one layer of standing DIP molecules as shown by the schematic with the chemical structure of DIP indicating how DIP molecules arrange (standing almost straight upright) on the substrate.

4.2 PTCDI-C$_8$ submonolayer morphology

PTCDI-C$_8$ deposited on SiO_2 substrates exhibits in-plane ordering. Submonolayer island geometries of PTCDI-C$_8$ can also be obtained using the same deposition strategy employed for DIP, *i.e.,* growing a very thin layer of the molecules onto SiO_2/Si (substrate

temperature 130°C). Islands of PTCDI-C_8, seen in the AFM topography image (and lateral force) in **Figure 4.2**, correspond to a surface coverage of ~ 0.48 ML. Unlike the DIP molecules, which stand almost completely perpendicular to the substrate on SiO_2, PTCDI-C_8 molecules typically tend to arrange in tilted stacks[26] and thus the height of the islands is smaller than the full length of a standing straight molecule. This statement is confirmed by the AFM topography image shown in **Figure 4.2**, in which the line height profile indicates a value (~ 2.2 nm), which is lower than the length of the PTCDI-C_8 molecules (~ 3 nm).[26] The measured height fits to the interlayer distance determined by X-ray diffraction (XRD) that corresponds to a tilted orientation of PTCDI-C_8 molecules.[26,27] From the height profiles in **Figure 4.1** and **Figure 4.2**, we conclude that the DIP and the PTCDI-C_8 islands on SiO_2 exhibit very similar heights (1.7 nm *vs.* 2.2 nm) with a height difference of only around 0.5 nm. Depending on the applied load during the AFM scan, it is not always straightforward to distinguish the two molecules once they are brought together to form heterostructures. This issue is further discussed in the next section.

In addition to the information about the height of the PTCDI-C_8 islands, lateral force microscopy (LFM; also found in the literature as frictional force microscopy (FFM)), represented in **Figure 4.2**, can give additional information about the PTCDI-C_8 in the first layer. Some PTCDI-C_8 islands, unlike DIP, exhibit different lateral force signals appearing as a contrast in the area, which is marked on the lateral force image shown in **Figure 4.2**. Extensive LFM studies of organic layers in the literature have reported friction anisotropy or asymmetry, which are associated with crystal anisotropy or molecular tilt.[136–138]
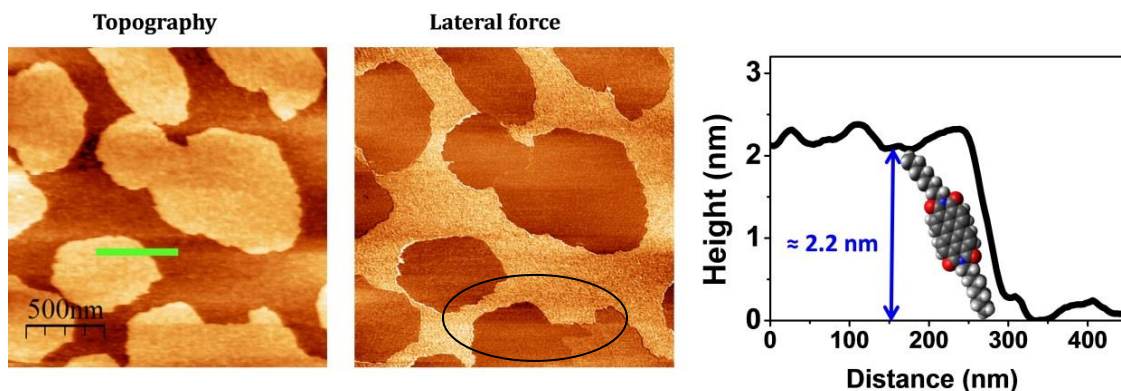
Figure 4.2: AFM topography and LFM map (FW) of submonolayer isolated islands of PTCDI-C_8 grown onto bare SiO_2/Si. The line profile corresponds to one layer of standing PTCDI-C_8 molecules in a tilted orientation as shown in the schematic of the molecule. The marked area in the LFM image, marks the contrast between the domains, which could be an indication of crystal anisotropy.

The idea of exploring the structural properties by means of LFM has been taken further into developing a new mode of lateral force microscopy, in which the scanning is done

transverse to the conventional AFM fast-scan direction and thus, is known as transverse shear microscopy (TSM). TSM translates the torsional deformation and/or twist of the AFM cantilever to a map known as the transverse shear map. This mode has been thoroughly employed by the Frisbie group in the past few years to study thin films of pentacene, showing that the TSM signal is more sensitive to the local structural order compared to the LFM signal and, therefore, it could provide additional information about disorder and anisotropy and help to distinguish domains with different crystalline orientations. High-contrast TSM images of thin films of pentacene have been correlated with differences in the directional orientation of the domains.[139,140]

Figure 4.3 shows the topography and TSM image of islands of PTCDI-C_8 on bare SiO_2/Si. As can be seen, the TSM image of PTCDI-C_8 island exhibit more heterogeneity compared to the lateral force map shown in **Figure 4.2**. In the TSM image, the different contrasts observed in different islands, and also within single PTCDI-C_8, islands are probably due to the presence of molecular domains with different orientations. Although this issue has not been investigated in this thesis, it is here emphasized that lateral force microscopy in its conventional mode and transverse mode may provide additional insight into the grain boundaries, grain size, grain shape and stacking orientation in ultrathin polycrystalline films. These properties are difficult to visualize by any other microscopy technique.
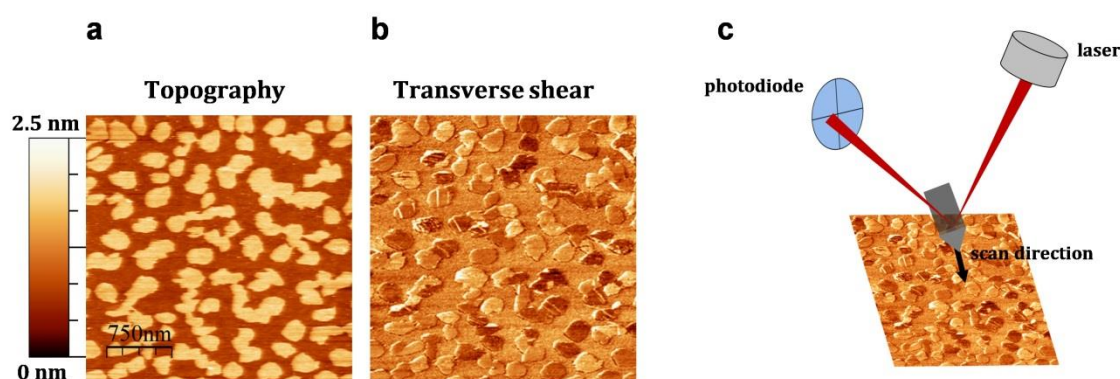
Figure 4.3: (a) AFM topography and (b) TSM map (FW) of submonolayer isolated islands of PTCDI-C_8 grown onto bare SiO_2/Si and (c) schematic of the working mechanism of the TSM technique.

4.3   DIP/PTCDI-C_8 heterostructure submonolayer morphology: horizontal heterojunctions

In this section a heterostructure configuration of DIP/PTCDI-C_8 with a side-by-side stacking configuration of the DIP and the PTCDI-C_8 molecules at the interface between the

two molecules is discussed, which will be referred to as the "horizontal heterojunction". In order to achieve such a configuration, sub-monolayer islands of PTCDI-C_8 were deposited onto SiO_2 using the optimized conditions for the PTCDI-C_8 growth (130°C substrate temperature). Subsequent to the growth of PTCDI-C_8, the substrate temperature was reduced to 80°C to meet the conditions for the growth of DIP. The deposition of DIP was initiated as soon as the substrate temperature reached 80°C through a different crucible cell of the vacuum evaporation system. The presence of PTCDI-C_8 islands on the substrate influences the growth of DIP in the way that the DIP molecules reaching the substrate surface from vapor phase nucleate around the existing PTCDI-C_8 islands to form isolated (or interconnected) islands, which consist of both types of molecules. **Figure 4.4** shows the morphology of such tailored nanostructure referred to as the horizontal heterojunction. The line profile in the topography image shows that the height difference between the PTCDI-C_8 islands and the DIP islands nucleated around them is approximately 0.5 nm which is in agreement with the difference between the heights of the islands of DIP and PTCDI-C_8 in their standing configuration as shown previously in Sections 4.1 and 4.2 for their single-component islands.
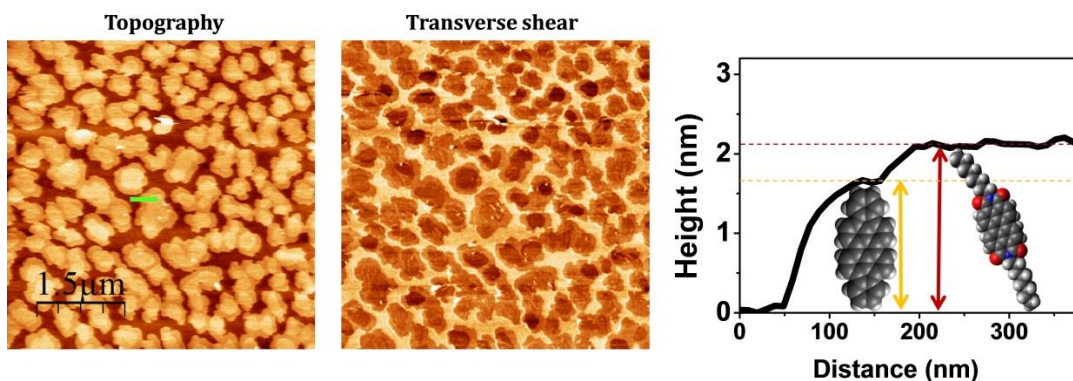
Figure 4.4: AFM topography and TSM map (FW) of submonolayer islands of DIP/PTCDI-C_8 grown onto SiO_2/Si in the horizontal heterojunction configuration. The line profile indicates that the stacking of both molecules is in the same manner as for the single-component submonolayer islands of DIP and PTCDI-C_8.

Figure 4.4 shows that from both topography and TSM images the two molecules can be easily distinguished. However, the height difference between the two species cannot always be distinguished from topography, especially when there is an intermixing due to co-evaporation of the molecules or simply smaller nucleation points induced by different growth conditions. In those heterostructures, the contrast between the DIP and the PTCDI-C_8 islands in the LFM or TSM maps can be used to identify the molecules.

Another important parameter that can be obtained from lateral force microscopy images is the molecular periodicity. Obtaining an image that contains information on the

molecular periodicity requires performing the measurement on a small area with a high scanning velocity. Such lateral force images obtained on an area consisting of both molecules in the heterostructures allows for the identification of the crystalline domains formed by each molecule. This application of the lateral force microscopy will be further discussed in the Section 4.6. **Figure 4.5** shows that the PTCDI-C$_8$ exhibits a striped structure with a periodicity of 1.04 nm in agreement with the slip-stacked face-to-face arrangement.[26]
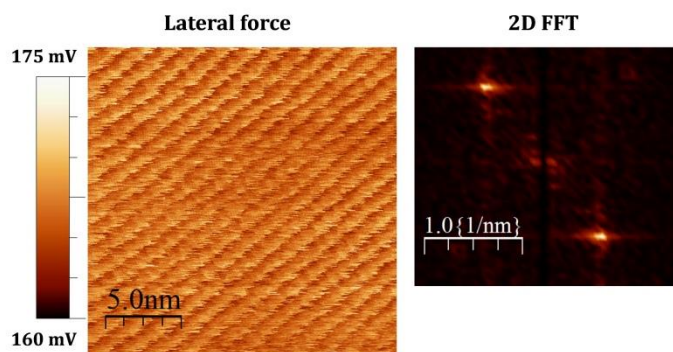
Figure 4.5: Lateral force image (FW) of a PTCDI-C$_8$ island showing the molecular periodicity. The image on the right shows the two-dimensional fast Fourier transform (2D FFT) pattern from the corresponding lateral force image.

The horizontal heterojunction consisting of DIP and PTCDI-C$_8$ can also be fabricated with a different architecture when the depositions of the two molecules are done in the reverse order, *i.e.,* a submonolayer of DIP is deposited, followed by sublimation of a submonolayer of PTCDI-C$_8$ which results in the nucleation of the PTCDI-C$_8$ molecules around the existing DIP islands. The morphology of such a configuration is shown in **Figure 4.6**. The line profile across an island, consisting of DIP and PTCDI-C$_8$ with DIP core, indicates that the height measured across the double-component island is in good agreement with the previous results suggesting that both species are in standing-upright structure. The lateral force image shows a contrast between the areas covered with DIP and PTCDI-C$_8$.
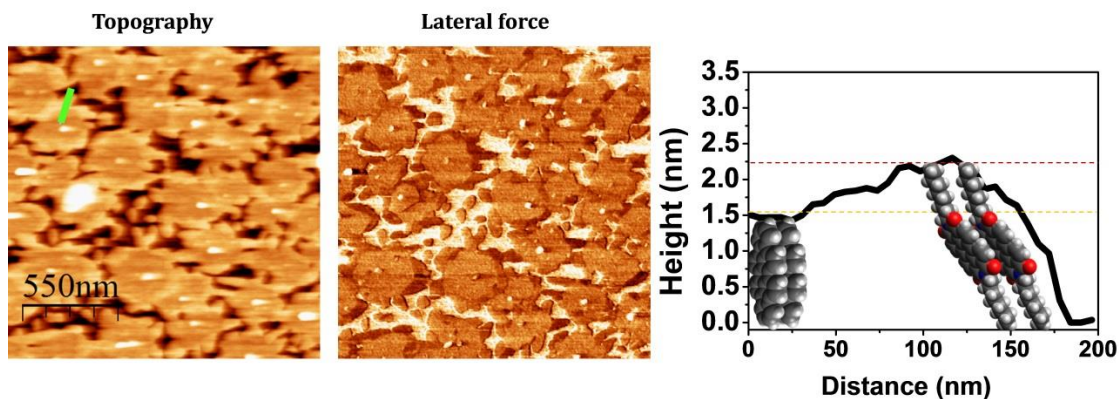
Figure 4.6: AFM topography and lateral force (FW) image of a horizontal heterojunction with DIP core and a line profile across an island (right) of submonolayer islands of DIP/PTCDI-C_8.

4.4 DIP/PTCDI-C_8 heterostructure submonolayer morphology: vertical heterojunction

The second heterojunction configuration, referred to as the "vertical heterojunction", will be discussed in this section. The name vertical heterojunction originates from the way the two molecules stack with respect to each other in a heterojunction consisting of DIP and PTCDI-C_8 molecules. For this purpose, a complete monolayer of DIP was deposited onto SiO_2/Si. Deposition of precisely one complete layer of DIP requires very good calibration of the quartz microbalance in the vacuum evaporation system. PTCDI-C_8 was then deposited on top of the existing monolayer of DIP. The morphology of the resulting vertical heterojunction is indicated in the AFM topography image in **Figure 4.7**. Since the presence of the DIP monolayer prevents imaging of the underlying SiO_2 substrate as a reference for the height calibration, the organic layer consisting of the two molecules was removed using the AFM probe by applying a high load to the tip in contact mode. The dark square in the topography image in **Figure 4.7** represents the area where the organic layer has been scratched away, leaving the SiO_2 substrate underneath visible. The line profile across the scratched square and the area around it, indicate that the growth of the vertical heterojunctions, with DIP as the bottom layer and PTCDI-C_8 on top of DIP, has been done successfully. The height of the organic structure on the substrate is ∼ 4nm, corresponding to the added layer heights of DIP and PTCDI-C_8 from Section 4.1 and 4.2.

The reverse architectures of the vertical heterojunction, *i.e.,* DIP on top of a PTCDI-C_8 layer, could not be successfully achieved because the DIP molecules tend to intercalate in between the crystalline domains of the underlying PTCDI-C_8 layer.
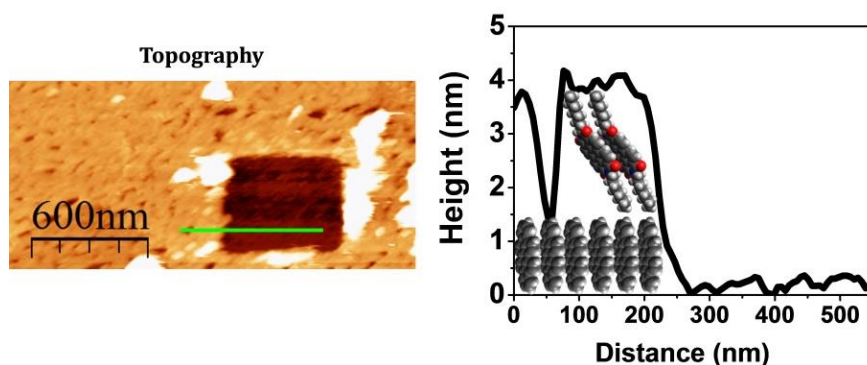
Figure 4.7: AFM topography of a vertical heterojunction of DIP/PTCDI-C$_8$ grown onto SiO$_2$/Si. The line profile indicates that the PTCDI-C$_8$ molecules stack on the existing layer of DIP in a standing-upright arrangement.

The π-orbitals of DIP and PTCDI-C$_8$ molecules do not overlap efficiently in the vertical configuration, because, besides their nearly-parallel orientation with respect to the heterointerface, the alkyl chains of the PTCDI-C$_8$ molecules produce a separation between the aromatic cores of DIP and PTCDI-C$_8$ molecules and, thereby, electronically decouple the two molecules.

4.5 Electronic phenomena at the DIP/SiO$_2$ interface and the PTCDI-C$_8$/SiO$_2$

To investigate the photo-induced charging phenomena at the interface between either DIP or PTCDI-C$_8$ and SiO$_2$ and at the interface between the two organic species in the heterojunctions, a nanoscale characterization of the surface potential (SP) was carried out by KPFM. We first focus on samples consisting of only one type of molecule. The topography and the simultaneously measured SP maps for the single-component samples (consisting only of DIP or PTCDI-C$_8$) grown onto p-doped SiO$_2$/Si are shown in **Figure 4.8**-a&b (DIP) and **Figure 4.8**-d&e (PTCDI-C$_8$).
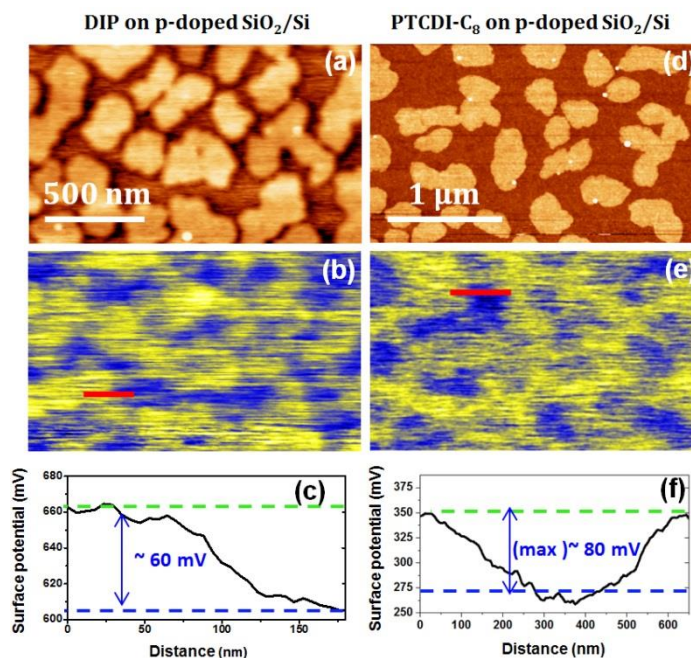
Figure 4.8: Topography and SP images of single-component submonolayers of DIP (left) and PTCDI-C$_8$ (right) grown onto SiO$_2$. The line profiles in the bottom mark the contact potential difference between SiO$_2$ and the organic islands on top of it.

As can be seen in the SP image of a submonolayer of DIP (**Figure 4.8**-b), DIP islands appear brighter than the bare surrounding SiO$_2$ substrate, indicating a larger surface potential with the value of the surface potential difference being Δ_{SP}(DIP-SiO$_2$)=0.06 ± 0.01 eV. PTCDI-C$_8$ islands, on the other hand, appear darker than the underlying substrate with Δ_{SP}(PTCDI-C$_8$-SiO$_2$)= -0.05 ± 0.03 eV.

The observed SP contrast between the PTCDI-C$_8$ molecular islands and the SiO$_2$ substrate could have originated from polarization effects. The two alkyl side-chains of the PTCDI-C$_8$ create a permanent dipole that could appear as a contact potential difference (CPD) in the SP maps. DIP, however, does not bear a permanent dipole moment that could explain the observed CPD. Interfacial dipoles originated from direct charge transfer between the molecules and the substrate can also be ruled out by the energetically unfavorable position of the energy levels of DIP and PTCDI-C$_8$ with respect to the Fermi level of the underlying silicon substrate.[141,142] Furthermore, similar contrast in KPFM images is observed using either p-doped or n-doped silicon as the substrate as illustrated in **Figure 4.8** and **Figure 4.9**. **Figure 4.9** shows the topography and SP image of a submonolayer of DIP grown onto n-doped SiO$_2$/Si. Similar to the case, where DIP was grown on p-doped silicon (**Figure 4.8**-b), DIP islands have a more positive surface potential compared to their underlying SiO$_2$/Si surface with a value in the same range as the one obtained from DIP islands deposited on the p-doped substrate (~ 0.06 V).
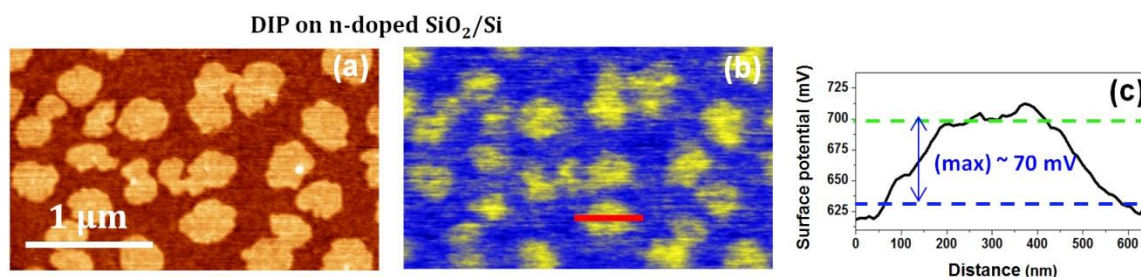
Figure 4.9: Topography (a) and SP (b) images of a single-component submonolayer of DIP grown onto n-doped SiO_2. The line profile indicates that $\Delta_{SP}(DIP\text{-}SiO_2) \approx 0.07$ V.

Another possibility that could play a role in the creation of the observed interfacial dipole (detected as contrast in SP images) between the molecules and their underlying substrate, is doping in air by environmental factors such as moisture, oxygen and/or contaminants. Although the KPFM measurements were done in a controlled environment (N_2 atmosphere) to minimize the effect of water adsorption, the samples were transferred through air from the vacuum evaporation system to the KPFM equipment. Therefore, the above-mentioned environmental factors might influence the measured SP values to a certain degree.[143]

4.6 Electronic phenomena at the DIP/PTCDI-C$_8$ interface in the horizontal heterojuctions

4.6.1 Kelvin probe force microscopy studies

The topography and surface potential maps of the two different configurations of the horizontal heterojunctions are shown in **Figure 4.10** for the case of PTCDI-C$_8$ surrounded by DIP (**Figure 4.10**-a,b,c) and DIP surrounded by PTCDI-C$_8$ (**Figure 4.10**-d,e,f). The sign of the surface potential for DIP and PTCDI-C$_8$ is the same as the ones observed in single-component samples, but the difference between DIP and PTCDI-C$_8$ in horizontal heterojunctions is a few tens of mV higher in some samples, which could be a hint of hole and electron trapping in DIP and PTCDI-C$_8$, respectively, caused by charge photogeneration originated from the exposure to ambient light.
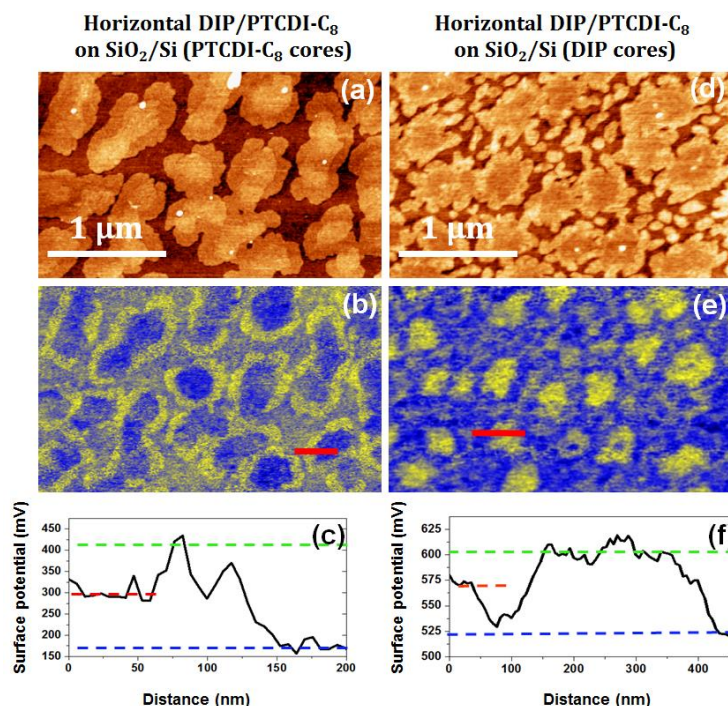
Figure 4.10: Topography and SP images of horizontal heterojunctions of DIP/PTCDI-C$_8$ grown onto SiO$_2$. The line profiles shown in (c) and (f) mark the contact potential difference between SiO$_2$ and the organic islands and also between the two organic components.

The effect of light exposure in a DIP/PTCDI-C$_8$ horizontal heterojunction was investigated by measuring the SP on the samples in dark and under illumination. The fresh samples were transferred to the KPFM setup in dark, the SP was compared to the SP of the same area of the sample when the KPFM is being performed under wide-band illumination. **Figure 4.11** shows the SP images obtained from the same region on the sample in dark and under illumination. The corresponding SP histograms indicate slight changes in the distribution and magnitude of the surface potential.
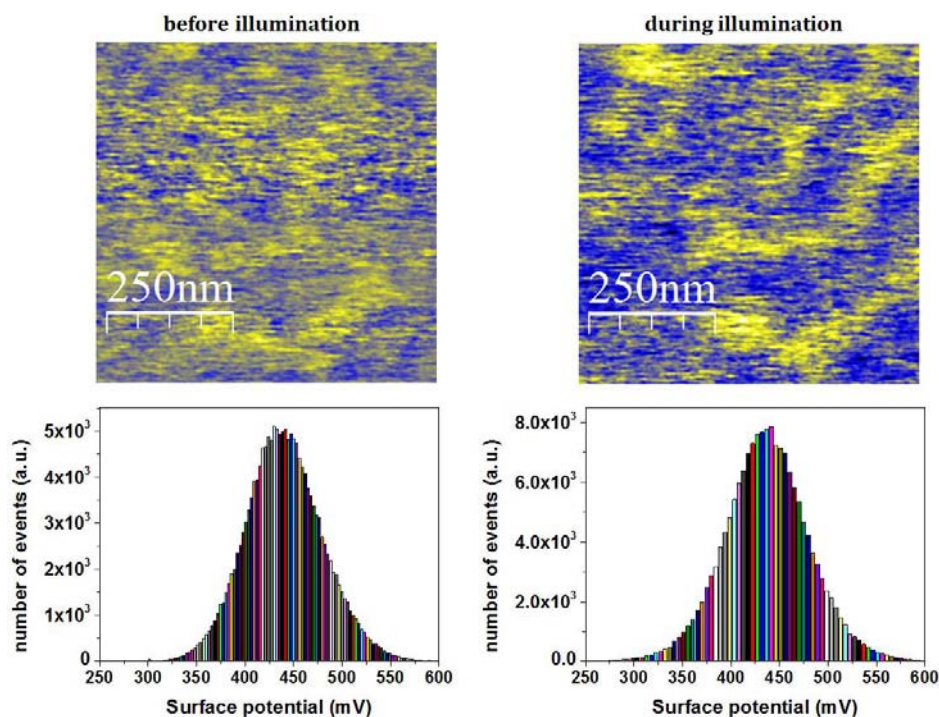
Figure 4.11: Surface potential maps of a DIP/PTCDI-C_8 horizontal heterojunction before exposure to light and under wide-band illumination. The SP histograms are indicated in the second row.

The observed variation in the magnitude of the Gaussian distribution between the two SP histograms shown in **Figure 4.11**, could be a sign for the presence of photocharging effects induced by the exposure to the light in the environment. However, large variations in the Δ_{SP}(PTCDI-C_8/DIP) values in different samples, refrains us from considering the KPFM results from the illumination experiment as a conclusive evidence for photocharging phenomena.

4.6.2 Photoluminescence spectroscopy studies

Further insight into the electronic interfacial phenomena in D/A heterojunctions or, more precisely, the effects of the structure of the D/A interface in exciton dissociation can be obtained using PL spectroscopy. In this section, in addition to PL investigations on horizontal and vertical heterojunctions of DIP/PTCDI-C_8, single component submonolayers of DIP and PTCDI-C_8 have been studied as reference. **Figure 4.12** shows the normalized PL spectra of a horizontal and a vertical heterojunction configuration along with the spectra from the pristine molecules. The corresponding AFM topography images indicate the morphology of the samples which were subject to our PL study.

The horizontal configuration (**Figure 4.12**-d) consists of islands of DIP surrounded by a rim of PTCDI-C_8 and the vertical configuration is made out of 0.8 ML of PTCDI-C_8 grown on

top of 1 ML of DIP. Note that the green laser light (λ=514 nm), employed in this PL measurement, is absorbed by both DIP and PTCDI-C$_8$ and therefore that region of the spectra is not illustrated.

The PL spectrum of DIP shows characteristic well-defined peaks at ~ 575 nm and 625 nm in accordance to previous PL measurements in DIP thin films,[144] while PTCDI-C$_8$ shows a broader PL emission centered at around 650 nm. The PL spectrum of the vertical heterojunction shows contributions of the emission of the single components due to recombination from singlet excitons. In contrast, the PL of the horizontal heterojunction, in which the appearance of an additional longer wavelength emission peak at ~ 737 nm is evident, differs drastically from the one of the vertical heterojunction. This pronounced peak dominates the PL spectrum for the horizontal configuration, while it is only very weak (appearing as a small shoulder) for the vertical heterojunction. The observation of a high wavelength/low energy peak in blends have been reported for different combination of donor and acceptor materials and is considered a signature of radiative recombination from a charge transfer (CT) exciton to the ground state across the D/A interface.[2,144–149]
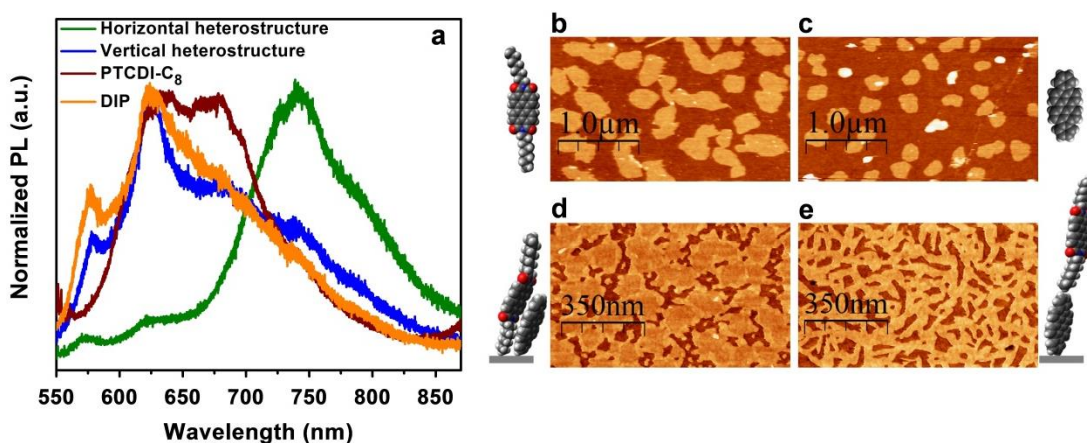
Figure 4.12: Photoluminescence spectra of DIP (orange), PTCDI-C$_8$ (brown), horizontal heterojunction (green) and vertical (blue) heterojunction and the corresponding AFM topography images (b-e). The emission peak around 737 nm, dominant for the horizontal heterojunction, is assigned to recombination from a charge transfer state.

The energy of the CT emission estimated from the PL peak observed in the horizontal heterojunction is $E_{CT} \approx 1.7$ eV. **Figure 4.13** indicates that the PL spectrum of the vertical heterojunction can be reproduced by the superposition of the PL spectra of the pristine DIP and the pristine PTCDI-C$_8$ with an additional (but small) contribution of the CT peak. Note that the CT peak appears much weaker in the vertical architecture and only as a shoulder to the PL spectrum. This is most likely due to the existence of adjacent stacking

of DIP and PTCDI-C$_8$, meaning that the sample does not entirely consist of vertically-stacked molecules, due to the error of the quartz microbalance calibration. Since such an error in our vacuum evaporation system is inevitable, the DIP coverage may differ by ±5% from 1 ML and, therefore, the DIP layer may contain few pinholes where PTCDI-C$_8$ could nucleate in a side by side configuration and this interface can give rise to the observed shoulder peak at the position of the CT state emission peak.
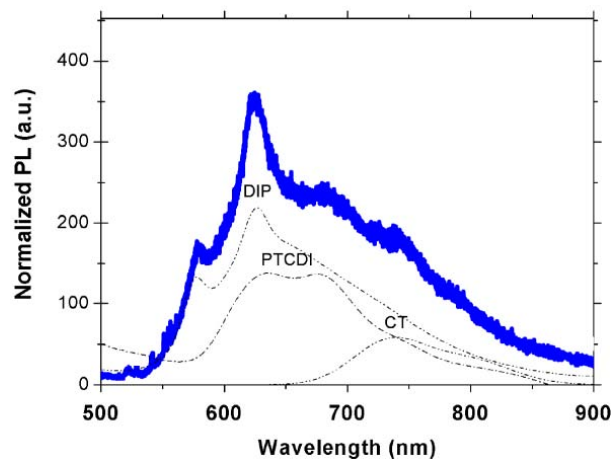
Figure 4.13: The photoluminescence spectrum of the vertical heterojunction fitted to the spectra from pristine DIP and PTCDI-C$_8$ and the CT emission (dashed lines). The PL of DIP and PTCDI-C$_8$ were independently modeled and fitted. The CT was fitted as two Gaussian components.

Up to this point, in all of the PL spectra which have been presented and discussed, the intensity of the peaks were normalized to one of the peaks and therefore, we have only commented on the position of the peaks (in wavelength) and not on their absolute intensities.

A general remark about PL spectra is that it is rather difficult to make a quantitative assessment based on the PL peak intensities. However, in some cases the PL peak intensities can be compared when using a well-calibrated setup with good control over the measurement conditions. Using such conditions, it was possible for us to identify a trend of stronger CT emission, when there is a larger interfacial area involved.

Two different horizontal heterojunctions were precisely tailor-made in order to have different amounts of shared interfacial area between DIP and PTCDI-C$_8$. **Figure 4.14** shows the AFM topography images of the two different configurations.

Configuration 1 was fabricated with a nominal coverage of 0.7 ML of PTCDI-C$_8$ plus 0.2 ML of DIP. The corresponding AFM topographic image of configuration 1 shows that this heterojunction consists of islands of PTCDI-C$_8$ with the lateral dimension of ~100 nm and a small rim of DIP surrounding them. The next heterojunction configuration, configuration

2, consists of 1.25 ML of PTCDI-C$_8$ plus 0.11 ML DIP. Although it might be expected that 1.25 ML of PTCDI-C$_8$ forms a flawlessly complete and closed layer in addition to some islands on top, in reality this is not the case. It turns out that configuration 2 consists of small DIP domains intercalated within the first almost-complete monolayer of PTCDI-C$_8$ and a second-layer islands of PTCDI-C$_8$ on top. **Figure 4.14** also includes an AFM topography image of the configuration 2.
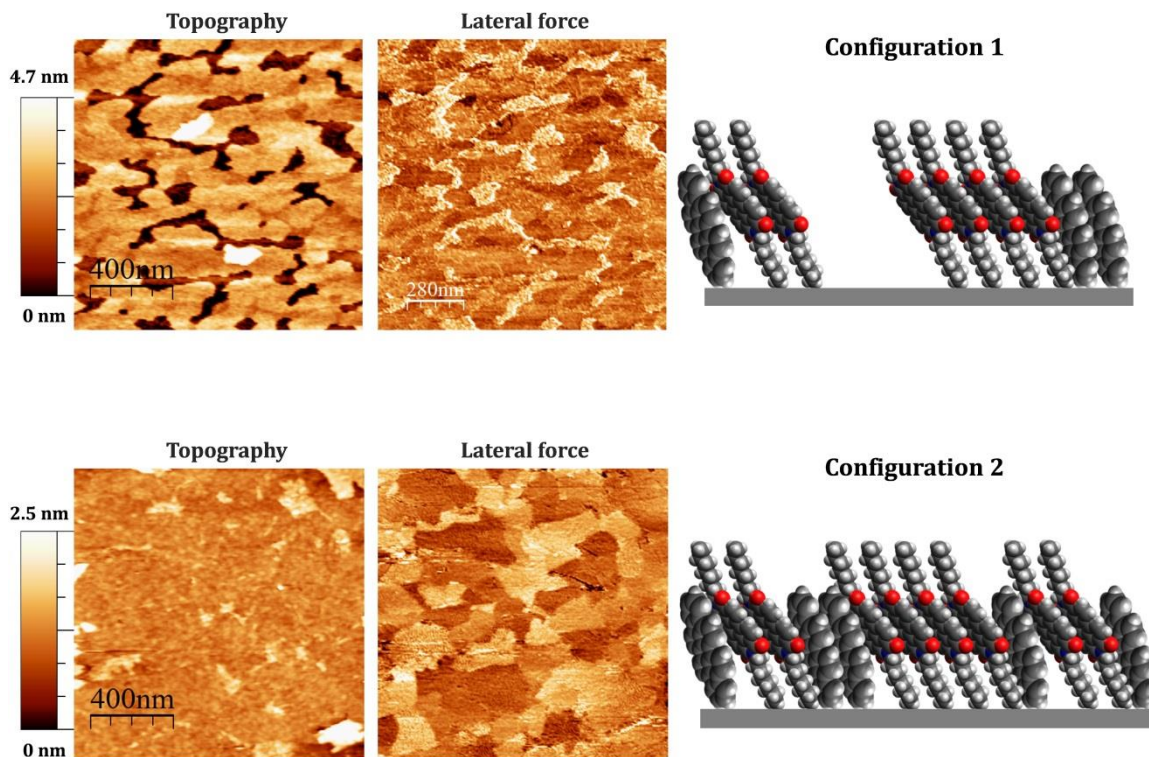
Figure 4.14: The AFM topography and lateral force maps (FW) of two horizontal heterojunctions with different degree of interfacial area between DIP and PTCDI-C$_8$ and a corresponding schematic showing the arrangement of the molecules.

Even though, due to the small size of the DIP domains in this sample, the DIP domains cannot easily be distinguished in the topographic image, molecular resolution images can provide evidence for the presence of the DIP molecular arrangement. For instance, the lateral force image shown in **Figure 4.15** was taken by scanning across the line boundary between DIP and PTCDI-C$_8$ domains in the horizontal heterojunction in configuration 2. In **Figure 4.15** two distinct periodic structures are observed that are characteristic of the molecular stacking of DIP and PTCDIC$_8$.
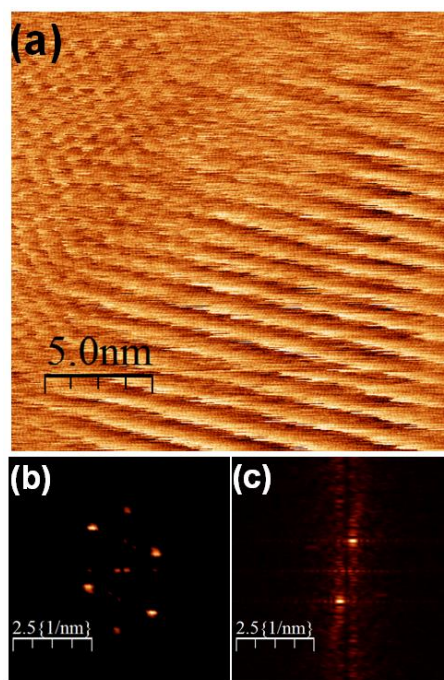
Figure 4.15: Top: (a) Lateral force image, taken at the domain boundary between DIP (left) and PTCDI-C_8 (right) in a horizontal heterojunction, showing the molecular periodicity at each domain: pseudo hexagonal for DIP and striped for PTCDI-C_8. Bottom: the two-dimensional fast Fourier transform (2D FFT) patterns from corresponding areas of DIP (b) and PTCDI-C_8 (c).

The pseudo hexagonal periodicity observed for DIP with an average lattice of ~0.6 nm (left-upper part in **Figure 4.15**-a) corresponds to the nearest-neighbor distance between DIP molecules ordered in a herringbone pattern.[150] PTCDI-C_8 exhibits a slip-stacked face-to-face arrangement appearing as a striped structure with a periodicity of 1.05 nm (**Figure 4.15**-c).

To sum up, the molecular periodicity study using lateral force microscopy reveals a very high degree of intercalation of small domains of DIP between PTCDI-C_8 domains in the horizontal heterojunction in configuration 2. The PL spectra of the two heterojunction configurations are shown in **Figure 4.16** where the PL intensities, unlike the ones in **Figure 4.13**, were not normalized and therefore, the graphs are plotted with different scales on the Y-axis. From the comparison between the two PL spectra shown in **Figure 4.16**, the significant difference between the intensities of configuration 1 and 2 is clear, *i.e.,* the PL intensity of the configuration 2 is almost an order of magnitude larger than the one of the heterojunction configuration 1. Due to the higher degree of intermixing of DIP and PTCDI-C_8, the configuration 2 seems to have a larger interfacial area ("interfacial perimeter") and this correlates well with the larger intensity of the interfacial CT emission observed in the PL spectrum.
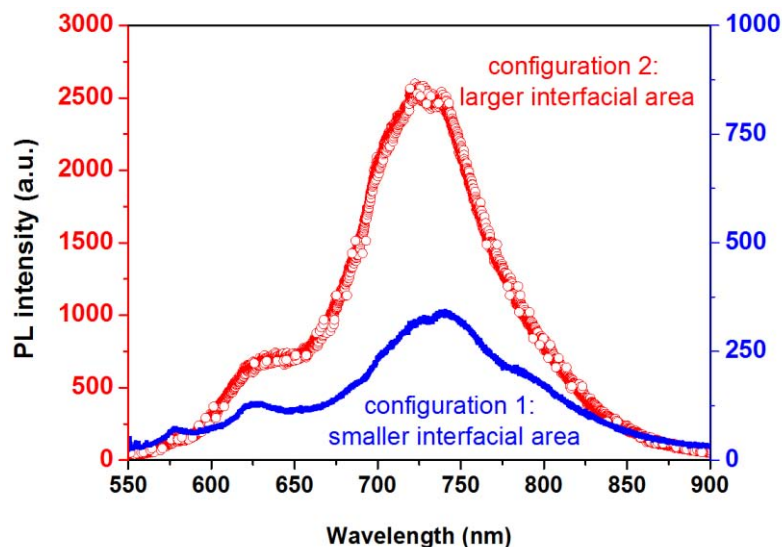
Figure 4.16: The photoluminescence spectra of two horizontal heterojunctions with different degree of interfacial area between DIP and PTCDI-C_8.

The energy of the CT state, $E_{CT} \sim 1.7$ eV, can be compared to the difference between the HOMO of the donor and the LUMO of the acceptor. The HOMO(D)–LUMO(A) difference is usually defined as the effective band gap energy (E_G) of the heterosystem. The value of the HOMO with respect to the vacuum level, referred to as ionization potential (IP), is $IP_{DIP} = 5.2$ eV for ultra-thin layers of DIP on SiO_2.[141] On the other hand, the estimated electron affinity (LUMO with respect to the vacuum level of PTCDI-C_8 is ~ 3.9 eV.[25] Therefore, the estimated E_G of HOMO(DIP) – LUMO(PTCDI-C_8) ~ 1.3 eV, which is clearly smaller than the energy of the CT exciton (E_{CT}). However, the energy band offsets at D/A heterojunctions may differ from the single components cases, even in absence of charge transfer.[151–153]

To explore this possibility, ultraviolet photoemission spectroscopy (UPS) experiments for the two model heterojunctions, the horizontal and the vertical heterojunctions with the same configuration were carried out, as shown in **Figure 4.12**-d and **Figure 4.12**-e, and for a submonolayer coverage of DIP for comparison.

4.6.3 Ultraviolet Photoemission Spectroscopy studies

The UPS spectra of the pristine DIP and the two heterojunctions are plotted in the **Figure 4.17**. For the DIP sample the onset of the HOMO is at 1.07 eV below the Fermi-level (E_F) of the SiO_2/n-Si substrate (*i.e.,* 4.1 eV below the vacuum level), an observation which is in excellent agreement with the previously reported UPS studies in the literature.[141] For both heterojunctions there is a shift of ~ 0.2 eV of the HOMO towards larger binding energies, with a slightly larger shift for the horizontal heterojunction. The shift of the

HOMO position in the heterojunctions can be attributed to decreased polarization energy, which, as reported by Akaike *et al.*, can lower the HOMO and raise the LUMO, causing an effective increase of the E_G of 0.2 eV to 0.5 eV.[152] An enlarged E_G in the heterojunctions agrees with an energy picture in which the E_{CT} is similar or slightly lower than E_G.
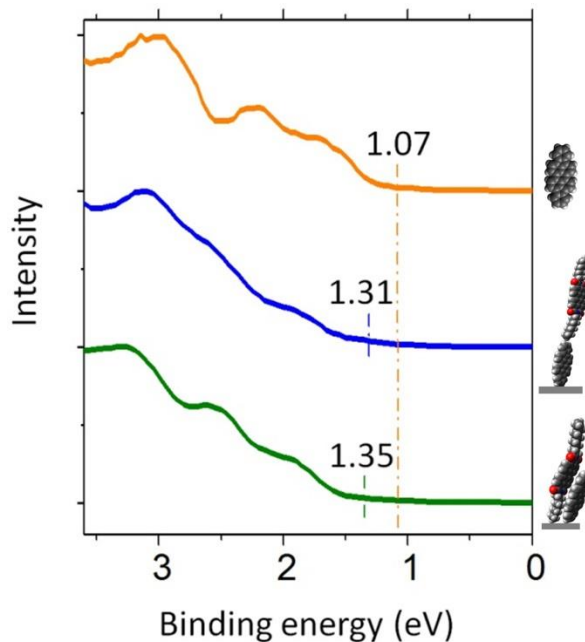
Figure 4.17: UPS spectra for islands of DIP (orange) and for a vertical (blue) and a horizontal (green) heterojunctions. The dashed lines indicate the onset of the HOMO.

4.7   Chapter conclusions

In this chapter we have put the emphasis on the profound impact of the different relative orientations of donor/acceptor molecules on the electronic properties of the interface by identifying the molecular orientation as a significant factor governing the exciton dissociation/recombination mechanisms through interfacial states.

The investigations in this chapter are based on two different model interfaces with different degrees of orbital overlap between the two molecules, namely a horizontal heterojunction (with more efficient π-orbital overlap) and a vertical heterojunction (with less efficient π-orbital overlap). Results from the PL spectroscopy indicate that the exciton dissociation is influenced by the different relative molecular orientations of DIP and PTCDI-C_8 across the D/A interface. We found that for the configuration with stronger orbital overlap between DIP and PTCDI-C_8 at the interface, the exciton dissociation is dominated by the recombination from an interfacial CT state. The second interesting observation is that the PL from singlet excitons, both in DIP and PTCDI-C_8, is not quenched, when the molecules assemble in a vertical configuration. Thus, in spite of the fact that the energy offsets are expected to be favorable for the exciton dissociation and the larger D/A interfacial area for this architecture, charge transfer across the D/A interface is hindered by the unfavorable orientation of the π-orbitals with respect to the heterointerface and the presence of the insulating alkyl chains.

Furthermore, the UPS study revealed that the specific local structure of the heterointerface also affects the position of the energy levels, resulting in a shift of the energy levels with respect to the values of the individual materials.

The present chapter emphasizes the importance of achieving local nanoscale control over the structure of organic/organic interfaces by means of molecular design and growth engineering as a step towards the fabrication of photovoltaic devices with improved performances.

5. Thin-film morphology of DNTT and performance of DNTT transistors

This chapter is devoted to the fundamental aspects of the fabrication and performance of DNTT thin-film transistors. Initially, three different methods of treating the gate oxide with SAMs will be presented, and the performance of TFTs fabricated using different SAM treatment methods will be compared.

A major part of this chapter is devoted to the detailed investigations of the morphology of the polycrystalline DNTT thin films deposited onto three different phosphonic acid SAMs by AFM.

Furthermore, the effect of different DNTT deposition rates on the thin-film morphology of DNTT will be investigated. More importantly, the impact of the DNTT morphology on the performance of DNTT TFTs will be studied by the measurement of the field-effect mobilities of TFTs with different DNTT nanostructure morphologies.

5.1 SAM treatment methods

In Chapter 2 we have introduced SAMs as ultrathin organic dielectrics/a passivation layer for the gate-oxide surfaces for the realization of high-performance organic transistors. In the present and the following chapters, different aspects of the use of SAMs as gate-oxide passivation layers will be discussed. In this section, the 3 most common SAM-treatment methods, namely dip coating, microcontact printing and sublimation in vacuum, will be studied in detail. DNTT TFTs were fabricated with the 3 different SAM treatment methods on the gate oxides and the results are compared in terms of field-effect mobilities and threshold voltages.

The chemical structure of the three different phosphonic acids for the formation of SAMs, which have been employed almost always throughout this thesis, namely, pentadecylfluoro-octadecylphosphonic acid (FC$_{18}$-PA), octadecylphosphonic acid (HC$_{18}$-PA) and tetradecylphosphonic acid (HC$_{14}$-PA), can be seen in **Figure 5.1**.
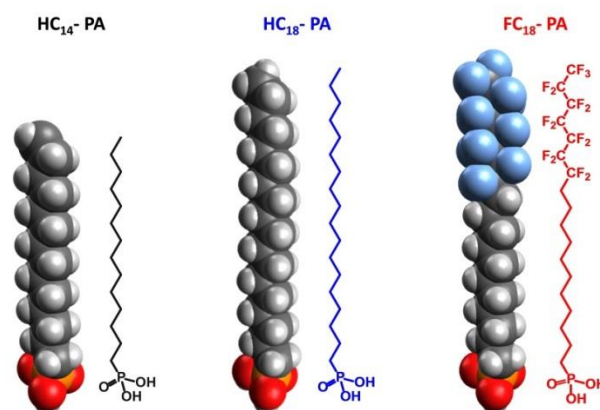
Figure 5.1: The 2D and 3D depiction of the chemical structure of HC$_{14}$-PA, HC$_{18}$-PA and FC$_{18}$-PA molecules.

5.1.1 Microcontact printing *vs.* dip coating

A PDMS stamp has been used for the microcontact printing of the FC$_{18}$-PA SAM onto a Si/SiO$_2$/Al$_2$O$_3$ (100 nm SiO$_2$ + 30 nm Al$_2$O$_3$) substrate directly after plasma treatment. The substrate was sufficiently large and the SAM has been stamped only onto a small part of the substrate. Therefore, on the same substrate there was an area left without the SAM. A nominally 25 nm thick layer of DNTT was deposited onto the whole substrate, followed by the deposition of source and drain gold contacts through a shadow mask. The shadow mask for patterning the source and drain contact was aligned in a way to fabricate transistors on the same substrate with two different gate dielectrics: one with the SAM

treatment and one without the SAM treatment. A schematic of this procedure is shown in **Figure 5.2**.
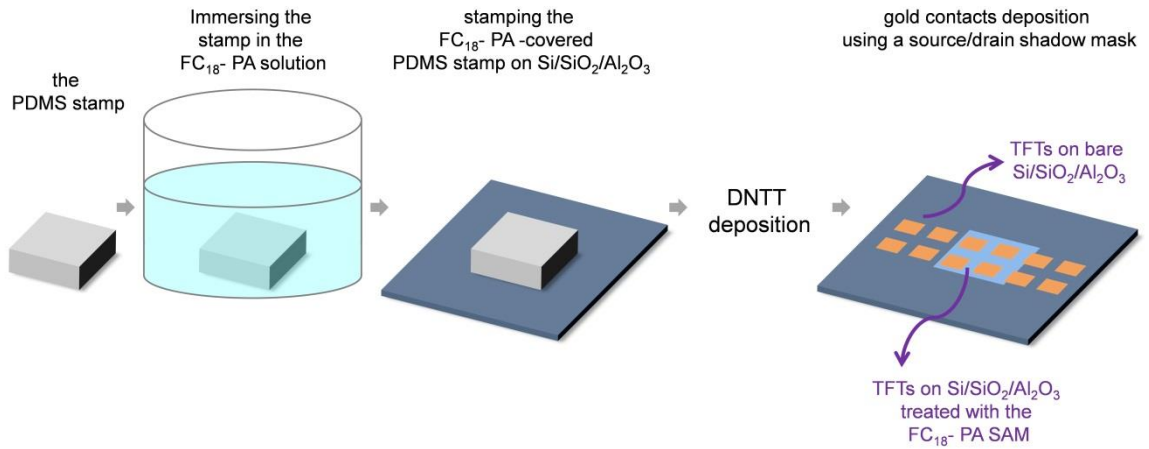
Figure 5.2: The procedure for microcontact printing of the FC_{18}-PA SAM and fabricating DNTT TFTs on the substrate partially covered with the SAM.

Additionally, a set of TFTs on a $Si/SiO_2/Al_2O_3$ substrate uniformly covered with the FC_{18}-PA SAM using the dip-coating method was fabricated for the purpose of comparison. The transfer curves corresponding to the 3 mentioned sets of TFTs (with microcontact-printed and with dip-coated FC_{18}-PA SAM and without SAM) in the linear regime are shown in **Figure 5.3**.
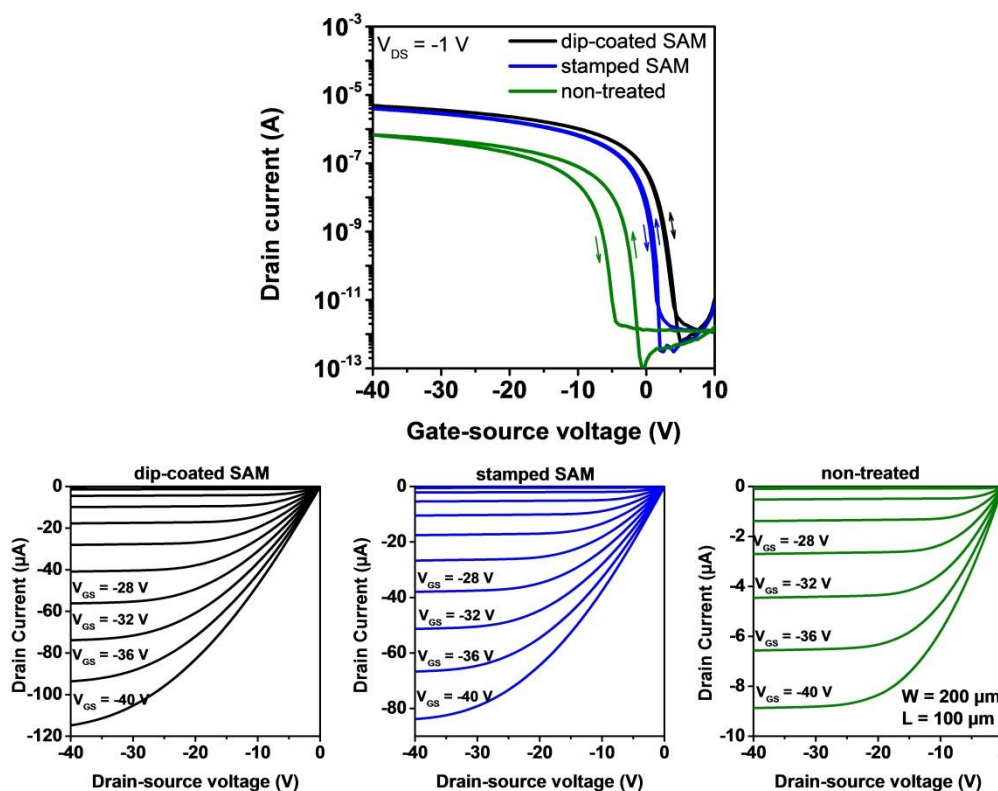
Figure 5.3: Transfer characteristics (linear regime $V_{DS} = -1$ V) and output characteristics of DNTT TFTs deposited onto bare Si/SiO$_2$/Al$_2$O$_3$ and Si/SiO$_2$/Al$_2$O$_3$ decorated with the FC$_{18}$-PA SAM by means of microcontact printing and dip coating.

Table 5.1 represents the TFT parameters from the devices discussed in **Figure 5.3** and the water contact angles of each substrate prior to the DNTT deposition.

Substrate treatment	Threshold voltage (V)	Field-effect mobility (cm^2/Vs)	Subthreshold swing (mV/decade)	Water contact angle (°)
dip coating	3.2	2.2	932	116
microcontact printing	1	1.9	869	112
none	-5.6	0.45	789	20

Table 5.1: The TFT parameters from **Figure 5.3** and the substrate water contact angles after the SAM treatment.

All devices exhibit a steep subthreshold swing as well as large on/off current ratios. However, the drain current in the device with a microcontact-printed SAM is around one order of magnitude larger than the drain current in the device without the SAM treatment on the dielectric. In addition, the effect of microcontact printing the SAM on the dielectric manifests itself with a more positive threshold voltage (1 V for a device with the microcontact-printed SAM *vs.* -5.6 V for the untreated device).* The field-effect mobility in

---

* Modulation of the threshold voltage towards more positive values, which is a typical outcome of treating the gate-oxide surface with the FC$_{18}$-PA SAM, will be discussed further in the next chapter.

the TFTs with a microcontact-printed SAM is 1.9 cm²/Vs which is significantly larger than 0.45 cm²/Vs for the untreated TFTs. These observations confirm an effective SAM treatment. The effectiveness of the SAM treatment using microcontact printing can be further evaluated by the comparison between the performance of the TFTs fabricated with the microcontact-printed SAM (the blue curve in **Figure 5.3**) and the ones manufactured with a dip-coated SAM on the dielectrics (the black transfer curve in **Figure 5.3**). The drain current in TFTs with dip-coated SAM treatments appears to be slightly larger than the one with a microcontact-printed SAM treatment and clearly larger than in the TFTs without the SAM treatment. The most positive threshold voltage (3.2 V) corresponds to TFTs with a dip-coated SAM treatment. The field-effect mobility of the TFTs fabricated with the microcontact printed SAM (1.9 cm²/Vs) is in the same range as the mobility of the TFTs with the dip-coated SAM (2.2 cm²/Vs). This observation is in agreement with a recent report by Hirata *et al.*, stating that patterning of a FC_8-PA SAM results in carrier mobilities comparable to those obtained with the dip-coated SAM and that the microcontact printing of the SAM does not impair the mobility of the TFTs.[154] Furthermore, the transfer curves of the devices treated with the SAMs exhibit almost no hysteresis between the forward and backward sweeps, independent of the SAM-treatment method, while the device without any treatment has considerable hysteresis. As discussed earlier in Chapter 2, hysteresis in the transfer curves is often associated with charge carrier trapping in the semiconductor close to the dielectric interface.[54] Therefore, it appears that by treating the gate-oxide surface with the FC_{18}-SAM, we can exclude hysteresis and probably an undesired trapping of charges.

Additionally, water contact angle measurements on the 3 substrates prior to the DNTT deposition shows that the water contact angle on the substrate without the SAM (20°) is substantially smaller than the ones on either one of the 2 substrates treated with the FC_{18}-SAM (116° for the dip-coated SAM and 112° for the microcontact-printed SAM). From the water contact angle values, the comparison between the 3 transfer curves shown in the **Figure 5.3** and the result obtained in the literature,[154] we deduce that microcontact printing and dip coating are both effective methods of treating the Al_2O_3 dielectric surface with a fluoroalkylphosphonic acid SAM. However, the improvement in the performance of the transistors by the SAMs appears to be more pronounced when the dip-coating method is employed. This is most probably associated with a less dense packing of the molecules in the microcontact-printed SAMs in comparison to the dip-coated SAMs.

5.1.2 Sublimation *vs.* dip coating

Another way of functionalizing the gate-dielectric surfaces with SAMs, which is distinguished from the two previous methods by its dry nature, is the sublimation of the SAM from the solid phase onto the substrate. The dry SAM treatment method has been used previously for silane-based SAMs by Halik *et. al.*,[155] and more recently for alkyl-phosphonic acid SAMs by Gupta *et. al.*[127] This method has the advantage of avoiding the wet procedure of immersion of the substrate in the solution (the case in the dip-coating method) or stamping from the solution (in the microcontact printing method). Therefore, it can be considered a *cleaner* technique, which avoids possible impurities (introduced by the solvent and other impurities in the environment), and it avoids the exposure to the ambient atmosphere between the SAM treatment and the semiconductor deposition.

In the following, we will discuss TFTs in which Al_2O_3 is used as the gate oxide in combination with SiO_2 on Si/SiO_2 substrates (100 nm SiO_2 + 8 nm Al_2O_3). The choice of the molecule for the SAM in this section was adapted from the work of Gupta *et al.* and it is octylphosphonic acid (HC_8-PA).[127] This molecule is an alkyl-terminated molecule, similar to the HC_{18}-PA and the HC_{14}-PA molecules shown in **Figure 5.1** but with a shorter alkyl chain. Two different treatment methods have been employed, sublimation in high vacuum and dip coating in the solution of the HC_8-PA in 2-propanol. Prior to the sublimation of HC_8-PA molecules, the Al_2O_3 surface was treated with oxygen plasma immediately, followed by mounting the substrates in the vacuum evaporation systems where a 10 nm thick layer of the HC_8-PA was deposited onto the substrate. The deposition of such a thick layer could potentially lead to disordered arrangement of the molecules, where they would form more than a monolayer. Post-annealing of the substrate in vacuum can serve for removing the physisorbed molecules and leaving an ordered chemisorbed monolayer of the HC_8-PA on the substrate. Therefore, the substrate was annealed in the vacuum evaporation system following the procedure used by Gupta *et al.*[127] The water contact angle of this SAM after being transferred to the ambient atmosphere was measured to be around 100° which is very similar to the one of the SAM formed by dip coating (103°). **Figure 5.4** shows the chemical structure of the HC_8-PA and the transfer characteristics of the two different sets of TFTs: one with a dip-coated SAM on the gate oxide (the red curve) and the other with a sublimed SAM (the black curve).
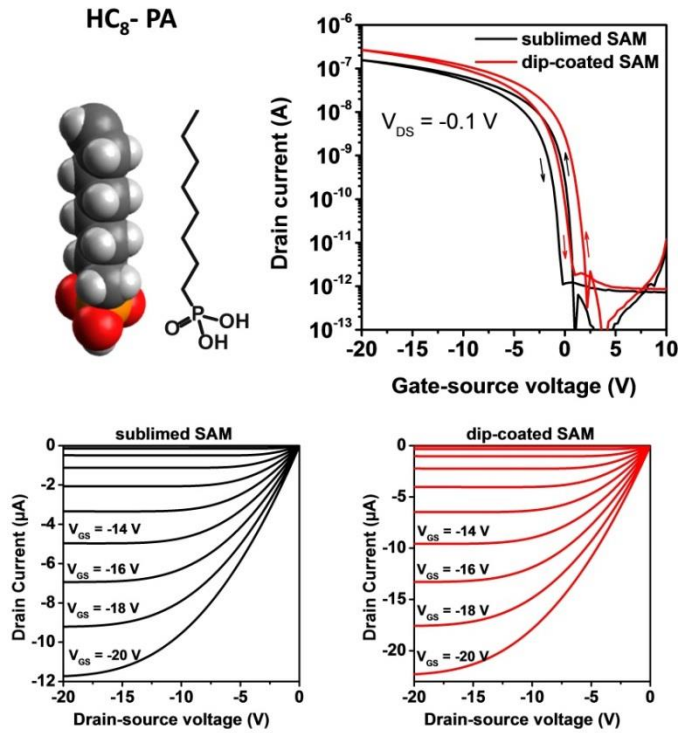
Figure 5.4: The chemical structure of HC$_8$-PA molecule, the transfer characteristics (linear regime V$_{DS}$ = −0.1 V) and the output characteristics of DNTT TFTs on Si/SiO$_2$/Al$_2$O$_3$ decorated with the HC$_8$-PA SAM by means of vacuum sublimation and dip coating.

Substrate treatment	threshold voltage (V)	field effect mobility (cm^2/Vs)	Subthreshold swing (mV/decade)	Water contact angle (°)
dip coating	-2	2.3	724	103
sublimation	-2.6	1.4	685	100

Table 5.2: The TFT parameters extracted from the transfer curves in **Figure 5.4** and the substrate water contact angles after the SAM treatment.

Both of the devices exhibit a large on/off current ratio, a steep subthreshold swing and an equally small hysteresis between the forward and backward sweeps. The drain current in TFTs with the dip-coated SAM at the gate dielectric appears to be slightly larger than the one in TFTs sublimed SAM. The threshold voltages and field-effect mobilities have been extracted from the transfer curves. The field-effect mobilities of the TFTs with the dip-coated SAMs are noticeably larger than that of the TFTs with the sublimed SAMs. As can be seen in **Table 5.2**, the threshold voltages of the TFTs with the sublimed SAM are slightly more negative compared to the threshold voltages of the TFTs, in which the SAM was formed using dip coating. Since the main focus of this experiment was to evaluate the effectiveness of a dry SAM process by sublimation, only devices with the sublimed SAM and the ones with a dip-coated SAM were fabricated and compared. Hence, we do not have a quantitative measure of the threshold voltage of the TFTs, in which the gate oxide is not treated with the SAMs. However, based on the results which will be presented in the

following section, the threshold voltage of a TFT with a gate oxide not treated with the SAMs is more negative than the threshold voltage of the devices treated with the alkyl-SAMs. Therefore, we assume from this observation that the more negative threshold voltage measured in the TFTs with the sublimed SAMs compared to the one in the TFTs with a dip-coated SAM signifies that the dip-coating method leads to a better electrical performance and, thus, is more effective. In other words, the dip-coating method leads to a more pronounced effect, which we expect from the alky-terminated phosphonic acid SAMs.

From the results and the discussions in Section 5.1, we conclude that the most effective method for the treatment of the Al_2O_3 gate-oxide surface with phosphonic acid SAMs (namely FC_{18}-PA and HC_8-PA) in terms of achieving the highest field effect mobilities and also the most effective threshold voltage modification from each SAM (according to the nature of the SAM), is dip coating *i.e.* immersion in the dilute solution of the molecules in 2-propanol. Therefore, the dip-coating method will be used as the SAM treatment method in the following chapters.

5.2 Performance of DNTT TFTs with dip-coated SAMs

In this section, we discuss the performance of DNTT TFTs on Si substrates with a combination of SiO_2 and Al_2O_3 as the gate-oxide layer (100 nm SiO_2 + 30 nm Al_2O_3), with and without SAM treatment. Four devices will be compared; in three of which the gate dielectric has been treated with phosphonic acid SAMs namely: the HC_{14}-PA SAM, the HC_{18}-PA SAM and the FC_{18}-PA SAM. In all four devices discussed in the following, a nominally 25 nm thick layer of DNTT has been deposited (all in the same deposition), followed by the deposition of gold top contacts. **Figure 5.5** shows the transistor characteristics of the four devices, which were introduced above.
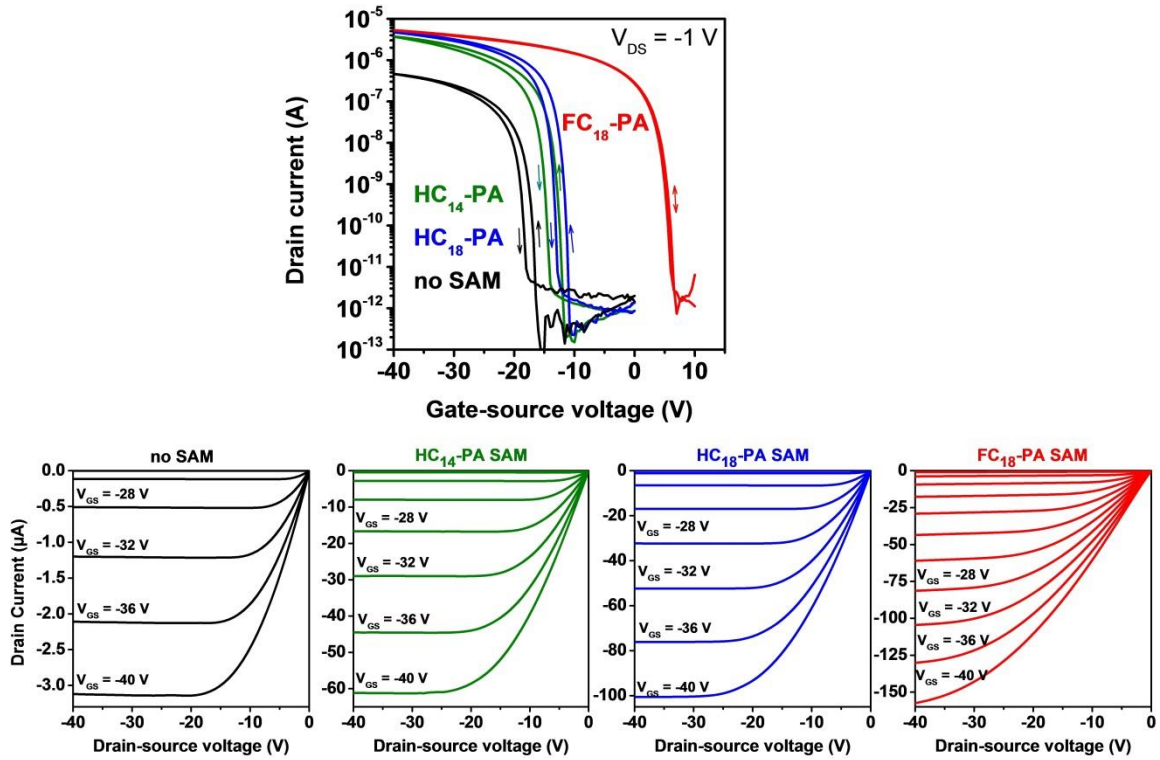
Figure 5.5: Transfer characteristics (in the linear regime with $V_{DS} = -1\,V$) and output characteristics of DNTT TFTs on bare $Si/SiO_2/Al_2O_3$ and on $Si/SiO_2/Al_2O_3$ decorated with the HC_{14}-PA SAM, the HC_{18}-PA SAM and the FC_{18}-PA SAM.

All TFTs exhibit a large on/off current ratio, a steep subthreshold swing and either a small or no hysteresis between the forward and backward sweeps. The maximum drain currents in the TFTs with the SAMs appear to be considerably larger than the one in the device without the SAM treatment.

The TFT parameters are shown below in the **Table 5.3**. According to the values indicated in **Table 5.3**, the SAM treatment improves the field-effect mobilities significantly.

SAM treatment	μ_{eff} (cm^2/Vs)	V_T (V)	On/off ratio	Subthreshold swing (mV/decade)
FC_{18}-PA-SAM	2.1	1.7	10^7	771
HC_{14}-PA-SAM	2.8	-16.7	10^7	764
HC_{18}-PA-SAM	3.3	-13.2	10^7	589
–	0.42	-19.6	10^7	1058

Table 5.3: The TFT parameters of DNTT TFTs fabricated on bare $Si/SiO_2/Al_2O_3$ and on $Si/SiO_2/Al_2O_3$ decorated with the HC_{14}-PA SAM, the HC_{18}-PA SAM and the FC_{18}-PA SAM, extracted from the transfer curves in **Figure 5.5**

Figure 5.5 and **Table 5.3** also indicate that treating the gate-oxide surface with the phosphonic acid SAMs results in a modification of the transfer characteristics compared to the transfer curve of the untreated device. This modification appears as a shift of the

threshold voltage towards more positive values. The TFTs with the HC_{14}-PA SAM and the HC_{18}-PA SAM have a more positive threshold voltage than the untreated device, with their threshold voltage values still being negative. The TFTs with the FC_{18}-PA SAM, on the other hand, have a positive threshold voltage. The impact of the SAMs on the threshold voltage will be discussed in detail in Chapter 6.

5.3   First stages of growth

In this section we focus on the first stages of the DNTT growth, *i.e.*, the first monolayer(s) of vacuum-sublimed DNTT films. The first stages of the growth are of particular importance, because the morphology of the active organic layer in the first few monolayers is the most determinant morphology for the charge transport in the TFTs consisting of organic thin films.[117–119] Four substrates with different surface properties have been selected for conducting the DNTT morphology experiments, namely a $Si/SiO_2/Al_2O_3$ substrate without the SAM treatment and $Si/SiO_2/Al_2O_3$ treated with the HC_{14}-PA SAM, the HC_{18}-PA SAM and the FC_{18}-PA SAM.

The AFM topography images of the silicon substrates ($Si/300$ nm SiO_2) coated with a 4 nm thick layer of Al_2O_3 (deposited by ALD) prior to the SAM treatment and upon treatment with the HC_{14}-PA SAM, the HC_{18}-PA SAM and the FC_{18}-PA SAM along with their corresponding root mean square (RMS) roughness values are shown in **Figure 5.6**. The AFM topographical maps show that all the substrates are almost morphologically identical and no inhomogeneity or defects can be resolved in these images. The surface roughness values of the substrates with the SAMs are all similar within the range of 0.37 nm to 0.38 nm RMS, which is comparable to the RMS roughness of the $Si/SiO_2/AL_2O_3$ without the SAMs.
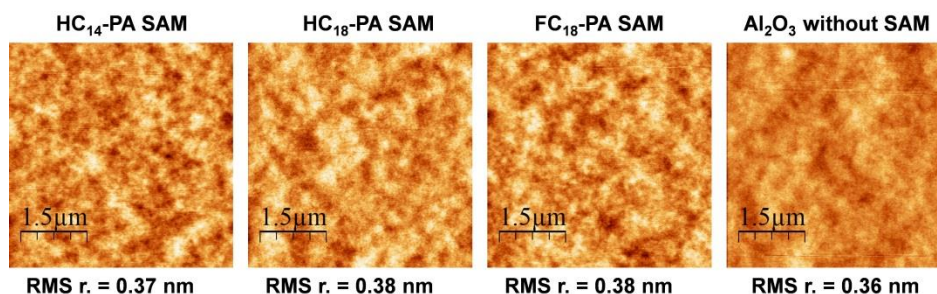
Figure 5.6: AFM topography of $Si/SiO_2/Al_2O_3$ functionalized with 3 different SAMs and also the Al_2O_3 without the SAMs with their corresponding RMS roughness values.

In order to further characterize the Al_2O_3 surface modified by the SAMs, wettability of the surfaces has been investigated by liquid contact angle measurements. The liquid contact angle is in direct correlation with *surface energy*. The smaller the wettability of a surface, the larger the liquid contact angle and the smaller the surface energy. In pentacene TFTs the surface energy of the gate dielectric has been reported to influence the thin-film morphology of pentacene and, as a result, the performance of the TFTs.[121,156,157] Contact angle measurements with different liquids can be used to estimate the surface energy of solids. In this context, the Owens- Wendt equation (Equation 5.1)[158] has been used to calculate the surface energies of the three SAMs (HC_{14}-PA, HC_{18}-PA and FC_{18}-PA SAM) using the contact angles measured with two different liquids, namely water and hexadecane (a non-polar liquid). This equation is based on the contact angle of a liquids and three interfacial surface energies, namely the liquid–vapor surface energy γ_{LV}, the solid–vapor surface energy γ_S and the solid–liquid surface energy γ_{SL}.

$$(1 + \cos(\theta))\, \gamma_{LV} = 2\sqrt{(\gamma_S^D \gamma_{SL}^D)} + 2\sqrt{(\gamma_S^P \gamma_{SL}^P)} \qquad \text{Equation 5.1}$$

Using the contact angles shown in **Table 5.5** and the known values of the liquid–vapor surface energies (γ_{LV}) of water and hexadecane obtained from the literature (shown in **Table 5.4**),[159] the dispersive and the polar components of the surface energies for the three SAMs have been obtained and represented in the table.

liquid	γ_{LV} total (mN/m)	γ_{LV} dispersive (mN/m)	γ_{LV} polar (mN/m)
hexadecane	27.5	27.5	0
water	72.8	21.8	51

Table 5.4: Liquid–vapor surface energies of water and hexadecane obtained from reference [159].

The water contact angle of an Al_2O_3 surface without the SAMs and directly after the plasma treatment is around 20°. The hexadecane contact angle of the untreated Al_2O_3 could not be precisely measured due to a complete wetting of the surface with the liquid. The large water contact angles of the SAM-decorated surfaces compared to the untreated Al_2O_3 surface confirm the modification of the surface through the SAM formation.

SAM treatment	water contact angle (°)	hexadecane contact angle (°)	γ_{SV} dispersive (mN/m)	γ_{SV} polar (mN/m)
HC_{14}-PA	104	35	22.75	0.56
HC_{18}-PA	106	40	21.44	0.44
FC_{18}-PA	116	70	12.38	0.32

Table 5.5: Water and hexadecane contact angles of $Si/SiO_2/Al_2O_3$ functionalized with 3 different SAMs and their corresponding estimated surface energies.

The polar components of all three SAMs are negligible compared to their dispersive components. The surface energies of the Al_2O_3 treated with the HC_{14}-PA SAM and the HC_{18}-PA SAM are very similar, while the surface energy of the Al_2O_3 treated with the FC_{18}-PA SAM is significantly smaller. Furthermore, since the water contact angle on the untreated Al_2O_3 surface is dramatically smaller than those on the Al_2O_3 surface treated with the SAMs, a much larger surface energy can be assumed for this surface. Therefore, it is plausible to expect different thin-film morphologies, when DNTT is deposited onto the substrates without the SAM treatment and those with a phosphonic acid SAM treatment.

Previous results on thin-films of DNTT have shown crystalline order with the DNTT molecules standing with their long axis approximately perpendicular to the substrate surface.[160] This molecular orientation with respect to the neighboring molecules leads to an efficient π-orbital overlap between the neighboring molecules (as discussed in Chapter 2) and facilitates in-plane continuous pathways for charge transport. With a reported layer spacing of 16.21 Å in the c-direction,[34] the height of the islands in a thin layer of DNTT is expected to be around 16.21 Å.

The growth of DNTT was studied in its primary stages *i.e.*, before the substrate was fully covered with a complete layer of the molecules. Deposition of a very thin layer of DNTT with a nominal thickness of 2 nm results in a partial surface coverage on a bare Al_2O_3 surface and on Al_2O_3 decorated with SAMs. The corresponding AFM topography images are shown in **Figure 5.7**. From the topography images it can be seen that, unlike our presumption made from the surface energies, using the SAMs has a minor impact on the morphology of DNTT in the first layer. **Figure 5.7** shows that the deposition of DNTT onto all three SAMs results in the formation of two-dimensional (2D) islands, with the islands on the alkyl-SAMs being slightly larger than those on the FC_{18}-PA SAM. The less compact shape of the DNTT islands on the FC_{18}-PA SAM could be related to a reduced surface diffusion on the surface due to the more disordered nature of the FC_{18}-PA SAM as a result of the repulsion of the fluorinated substituents head group of these molecules.[161] DNTT deposition onto the bare Al_2O_3 surface leads to the typical 2D islands similar to the case, when DNTT is deposited onto the SAMs. There is a low distribution of 3D islands present in all the four substrates. On the bare Al_2O_3 surface, a ribbon-like aggregate as high as 30 nm can be seen, with a height that corresponds to several layers of DNTT molecules stacked in the upright and/or lying-flat orientation.

On the whole, from the similarities in the DNTT island shape and densities independent of the surface of the substrate, we gather that the surface energy is not the dominant factor

to determine the DNTT growth. Therefore, the observed improvements in the performance of DNTT TFTs upon functionalizing the gate-oxide with SAMs (see **Table 5.3**), cannot be associated with changes in the morphology of DNTT.*

The substrate temperature and the deposition rate, however, are parameters that can be used to influence the island geometry and density, as reported for pentacene monolayer islands grown onto SiO_2 and Al_2O_3.[162] The influence of the DNTT deposition rate on the morphology of the thin films of DNTT and on the performance of DNTT TFTs will be investigated in the following sections.

The line profiles on the DNTT islands in **Figure 5.7** show that the height of one 2D island in the first layer is around 3.2 nm. Assuming that the DNTT molecules adopt an upright position on the substrate surface, the height of 3.2 nm corresponds to the height of **two** layers of standing-upright DNTT molecules.
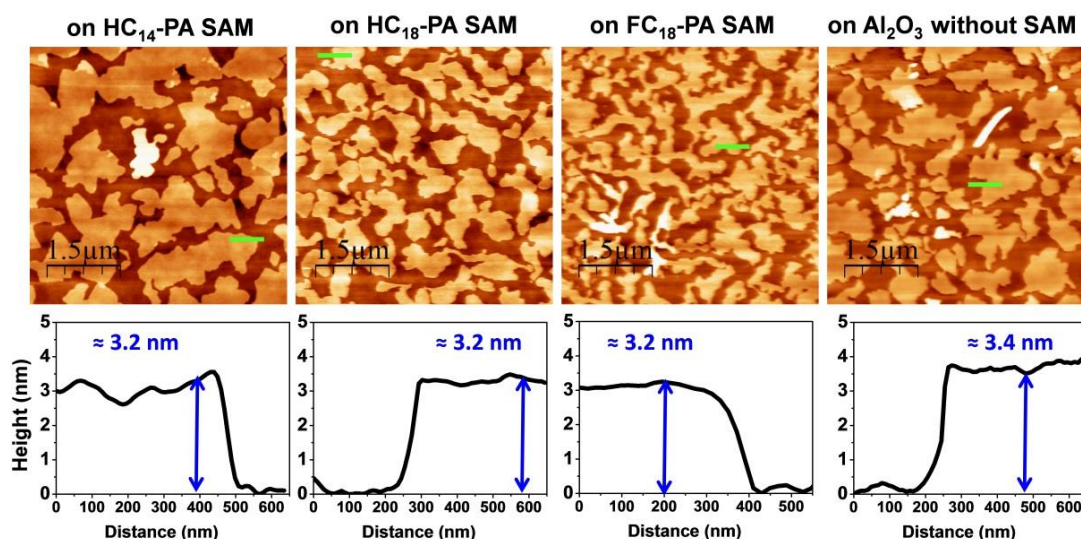
Figure 5.7: AFM topography of a nominally 2 nm thick layer of DNTT grown on 3 different SAMs and also the Al_2O_3 without SAM representing the nanostructure thin film morphology of DNTT islands in the first layer.

This outcome has been reproducibly observed for several samples, *i.e.* depositing DNTT at a moderate deposition rate (0.03 nms^{-1}) leads to the formation of compact islands with a thickness of at least 2 molecular layers in the first layer. The growth of bilayer islands instead of single-molecular islands is not usually observed for other vacuum-deposited organic small molecules to the best of our knowledge. This observation suggests a significant interlayer interaction in DNTT molecules, where the molecules could adapt a

---

* The enhancement of the field-effect mobility has been associated with the suppression of trap sites on the gate-oxide.

different packing during the formation of the first complete molecular layer. Thorough surface x-ray diffraction investigations could help to determine the molecular structure of DNTT thin films in their primary stage of growth. Such studies would not have been possible given the time frame of this dissertation, but could be carried out as future work.

5.4   Thin film morphology

In this section we move our focus to the morphology of DNTT beyond the first layer and investigate the morphology of multi-layered DNTT thin films that are employed as active layers in TFTs. Initially, the thin-film morphology of DNTT deposited onto the HC_{14}-PA SAM is introduced. Later the thin-film structure of DNTT grown on top of the HC_{18}-PA and the FC_{18}-PA SAM will be investigated in the following sections. **Figure 5.8** shows a cross-polarized optical micrograph of the microstructure of a nominally 25 nm thick DNTT layer deposited onto $Si/SiO_2/Al_2O_3$ functionalized with a HC_{14}-PA SAM. This image confirms the polycrystallinity of the DNTT thin film, since the cross-polarized optical microscopy of an amorphous film would lead to a featureless and dark image. As can be seen in **Figure 5.8**, the thin films of DNTT consist of micrometer-sized crystallites of various sizes and orientations. The difference in the emission of DNTT grains in terms of light intensity from different grains and also their different colors can be attributed to different crystallographic orientations.
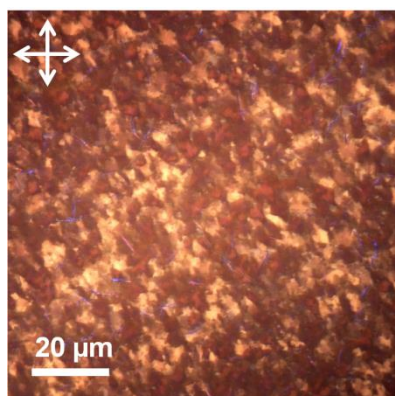
Figure 5.8: Cross-polarized optical micrograph of a nominally 25 nm thick layer of DNTT grown on the HC_{14}-PA SAM representing the microstructure thin film morphology of DNTT.

Figure 5.9 shows the AFM topography of the sample used in **Figure 5.8** measured in dynamic mode and its corresponding amplitude map. In both the topography and the amplitude image, it can be clearly seen that the DNTT forms multilayered mounds. The line profile shows that each terrace has the same height with a value that corresponds to the height of a single-molecule layer of standing-upright DNTT (1.6 nm).
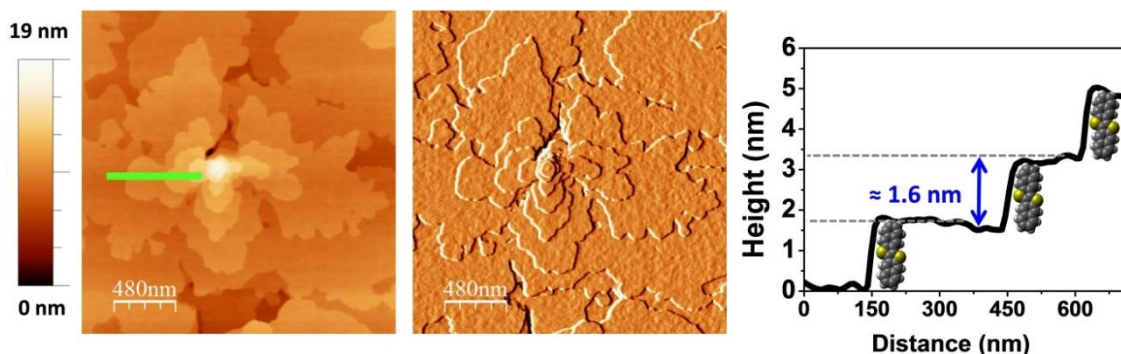
Figure 5.9: AFM topography and amplitude image of a nominally 25 nm thick layer of DNTT grown on the HC_{14}-PA SAM representing the thin film morphology of DNTT with several layers. The line profile across the DNTT molecular layers shows that the height of each terrace corresponds to one molecular layer of DNTT.

In addition, DNTT tends to form ribbon-shaped aggregates as can be seen in the AFM topography image shown in **Figure 5.10**. Regardless of the SAM, onto which the DNTT films are deposited, the ribbons are present on top of the terraced DNTT structures. The presence of such additional elongated ribbon-like structures has been reported for the growth of DIP thin films on SiO_2 substrates by Dürr *et al.,* where the ribbons are identified as a metastable phase that occurs beyond a certain DIP coverage and not in the first few monolayers.[163] The line profile on such a ribbon-like aggregate in the AFM topography image shows that each ribbon is around 30 nm high, a height which corresponds to a stack consisting of several layers of upright-standing (or flat-lying) DNTT molecules.[*] Similar structures have been observed on top of DIP thin films and they were identified as lying-down molecules on the substrate.[163]
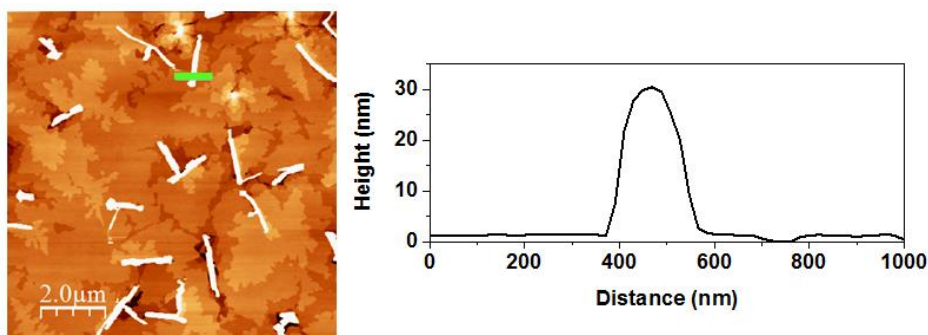
Figure 5.10: A larger AFM topography of a nominally 25 nm thick layer of DNTT grown on the HC_{14}-PA SAM consisting of 30 nm high ribbons (as shown in the line profile graph) in addition to the several-layered interconnected islands.

---

[*] The multilayer thin-film morphology of DNTT deposited onto the HC_{18}-PA SAM and the FC_{18}-PA SAM will be shown in the next section.

5.5   Deposition rate studies: Morphology and TFT performance

It has been shown that the deposition parameters, such as the substrate temperature during growth and the deposition rate, can influence and regulate the crystal structure and the thin-film morphology of organic semiconductors such as pentacene.[164,165] Following this idea, we have altered the DNTT deposition rate and studied its impact on the thin-film morphology of DNTT. The purpose of this investigation was to verify the impact of the DNTT morphology on the performance of the TFT devices.

For this study, DNTT has been deposited with different deposition rates, and the morphology has been studied by means of AFM, both for an early stage of the growth and for multilayered thin films (used as the active layer in TFT devices). The topographical images of a partial layer of DNTT (with nominal thickness of 2 nm using a low deposition rate of 0.007 nm/s and a moderate rate of 0.03 nm/s) deposited onto HC_{14}-PA SAM can be seen in **Figure 5.11**. The two AFM images indicate that varying the DNTT deposition rate influences the island geometries significantly: The partial layer of DNTT deposited with a low rate mainly consists of 2D islands in addition to a low density of 3D islands. The 2D islands have mostly a distinct dendritic shape, which is not the case for the islands grown using a moderate deposition rate. In addition to the dissimilar shape of the islands, depositing an incomplete layer of DNTT with a low deposition rate has another interesting outcome: some DNTT islands are 1.6 nm high, a height that corresponds to 1 molecular layer of standing DNTT molecules (line profile in **Figure 5.11**-b). However, as can be seen in **Figure 5.11**-a (and also as discussed in Section 5.3), DNTT tends to form islands with a double-molecular-layer height. In spite of the presence of some DNTT islands with single-molecular-layer height, the height of the majority of the DNTT islands seen in **Figure 5.11**-b corresponds to two DNTT molecular layers. Furthermore, the morphology has been investigated by AFM four weeks after the deposition. During this time, the substrate was stored in ambient air at room temperature. The AFM topography image (**Figure 5.11**-c) indicates that the morphology of the DNTT film has evolved during this time with an apparent trend of the rearrangement of the single molecular layer islands into two molecular layers. This suggests that single DNTT layers are unstable and the morphology evolves towards a bilayer structure over time. The evolution of the DNTT single-layered islands into bilayer islands has been previously reported by the Frisbie group, where they have associated this effect with the equilibration of the inhomogeneously distributed strain within the first and second molecular layers.[166]
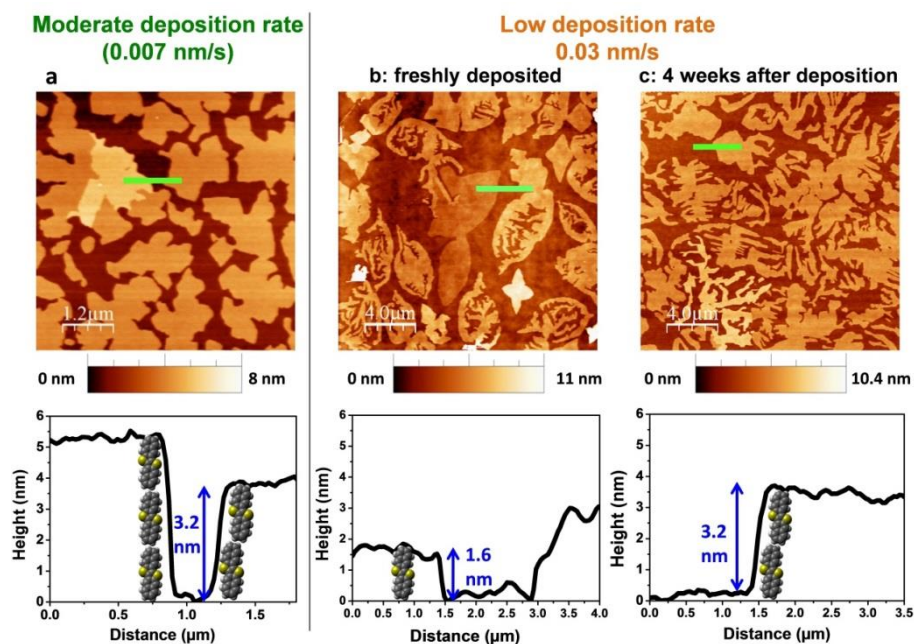
Figure 5.11: AFM topography images of a nominally 2 nm thick layer of DNTT deposited onto Si/SiO$_2$/Al$_2$O$_3$ functionalized with the HC$_{14}$-PA SAM with a moderate deposition rate (a) and a low deposition rate freshly after deposition (b) and four weeks after deposition (c). The height line profiles indicate that single-molecular layer DNTT islands evolve into bilayer islands after four weeks.

Further investigations on the nucleation and growth mechanism of DNTT are out of the scope of this thesis. The main focus of the following chapters will be the performance of the DNTT TFTs.

Since the deposition rate of DNTT influences the island geometries during the first stages of growth, it could inherently determine the multilayered thin-film morphologies consisting of several molecular layers, which is the morphology used as the active organic layer in the TFTs. The effect of the deposition rate on the morphology of thicker films of DNTT is discussed in the following. In order to conduct a systematic study, from this point of the thesis onwards, the HC$_{18}$-PA SAM and the FC$_{18}$-PA SAM will be utilized. The molecules forming these SAMs have the same chain length while being distinguished by their chain terminations. Therefore, the effect of the chain length (different chain length in the HC$_{14}$-PA SAM) can be excluded in the following chapters.

Figure 5.12 and Figure 5.13 show the multilayer thin-film morphologies of DNTT (used as the active organic layer in DNTT TFTs), deposited onto the HC$_{18}$-PA SAM and the FC$_{18}$-PA SAM, with a low deposition rate of 0.007 nms^{-1}, a moderate deposition rate of 0.03 nms^{-1} and a high deposition rate of 0.3 nms^{-1}. The multilayer morphologies of DNTT on the HC$_{18}$-PA SAM appear rather similar when the DNTT layer is deposited with a low deposition rate or a moderate deposition rate. In both cases the DNTT layer consists of

moundlike layered structures. This morphology is similar to the one of DNTT grown on the FC_{18}-PA SAM, when a moderate deposition rate is employed, as shown in **Figure 5.13**. However, when DNTT is deposited with a low deposition rate onto the FC_{18}-PA SAM, the morphology looks rather different, consisting of inhomogeneously distributed crystal-like structures with large gaps (where the substrate is not covered by DNTT) in between the structures that are clearly marked in the line profile. These structural variations in the DNTT thin-film morphology can potentially influence the shape and density of the grain boundaries. Independent of the SAM onto which the DNTT is deposited, the high deposition rate results in a much larger density of the ribbon-like structures (also observed earlier in **Figure 5.10**) and in a larger density of mounds. Even though we do not have control over the presence of such aggregates, **Figure 5.12** and **Figure 5.13** provide evidence that it is possible to vary the density of these ribbons by modifying the deposition rate. As can be seen, the ribbons appear as the highest features in all of the AFM topography images. Although neither the origin of the formation of such ribbon-like features nor their nature (whether it is a different growth phase of DNTT) is known to us, the contribution of these aggregates to the charge-transport efficiency in transistors can be identified by studying the field-effect mobilities in DNTT TFTs with different densities of these ribbons in the semiconductor layer.
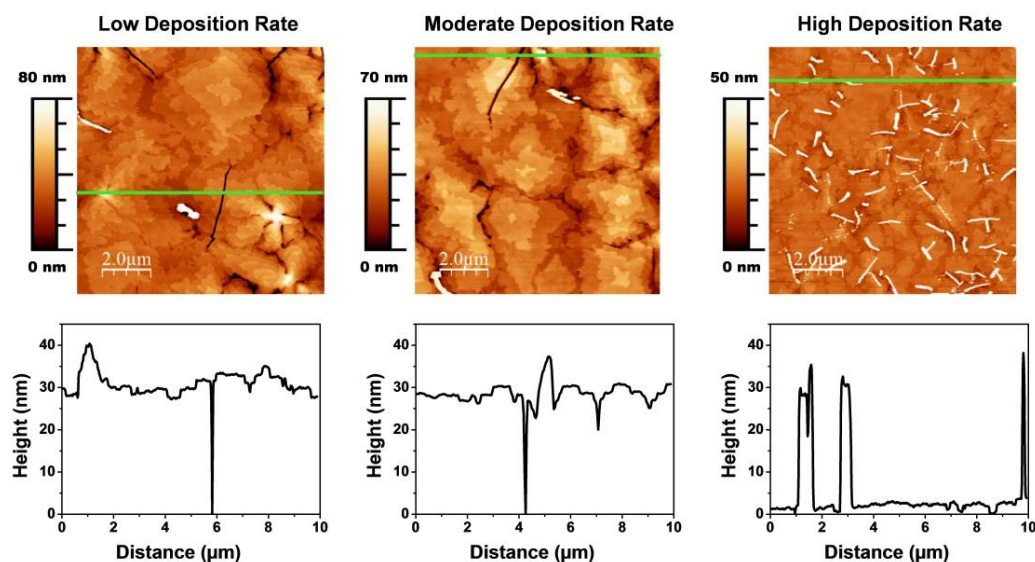
Figure 5.12: AFM topography images of multilayers of DNTT deposited with 3 different deposition rates onto the HC_{18}-PA SAM (top row) and the corresponding line profiles (bottom row).
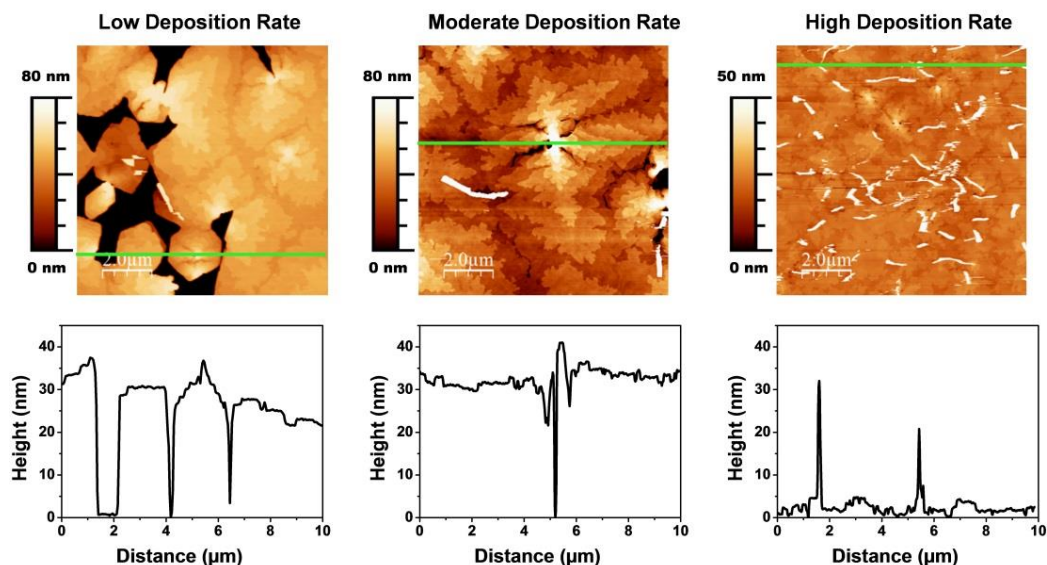
Figure 5.13: AFM topography images of multilayers of DNTT deposited with 3 different deposition rates onto the FC_{18}-PA SAM (top row) and the corresponding line profiles (bottom row).

The influence of the deposition rate on the performance of the transistors was investigated in the TFTs, in which the DNTT layer was deposited with the three different deposition rates. The thin-film structures of the DNTT layers in these transistors were shown and discussed above in **Figure 5.12** and **Figure 5.13**.

Figure 5.14 shows the transfer characteristics of the three sets of DNTT devices in which the DNTT layer was deposited using three different deposition rates. The corresponding field effect mobilities are shown in **Table 5.6** and in a graph over the deposition rate in **Figure 5.14**.
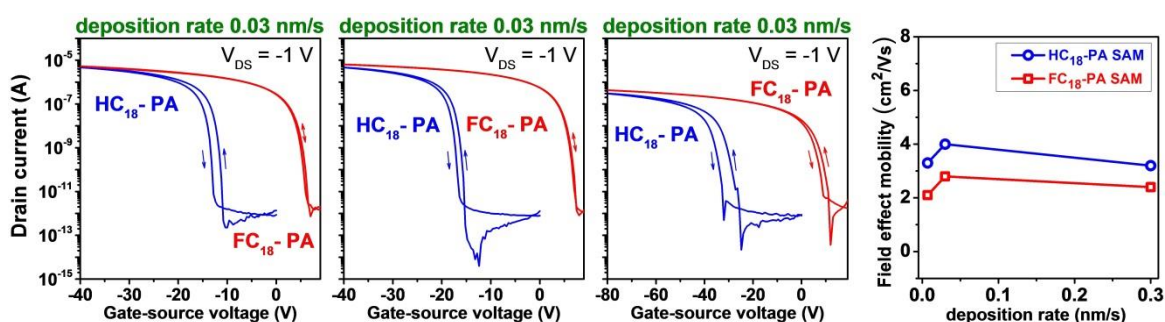
Figure 5.14: Transfer characteristics (in the linear regime) of DNTT TFTs with the DNTT layer deposited with three different deposition rates onto a HC_{18}-PA SAM (the blue curves) and a FC_{18}-PA SAM (the red curves). The field effect mobilities are also shown over the deposition rate.

SAM type	Low rate (0.007 nms^{-1})	Moderate rate (0.03 nms^{-1})	High rate (0.3 nms^{-1})
HC$_{18}$-PA	3.3 cm²/Vs	4 cm²/Vs	3.2 cm²/Vs
FC$_{18}$-PA	2.1 cm²/Vs	2.8 cm²/Vs	2.4 cm²/Vs

Table 5.6: Field effect mobilities corresponding to the DNTT TFTs extracted from the transfer curves shown in **Figure 5.14**.

The DNTT TFTs with their active layer deposited at different rates exhibit minor variations in the field-effect mobilities (3.2 cm²/Vs to 4 cm²/Vs for the devices with the HC$_{18}$-PA SAM and 2.1 cm²/Vs to 2.8 cm²/Vs for the devices with the FC$_{18}$-PA SAM).

The overall conclusion from the investigations conducted in this section is that despite the significant differences in the DNTT morphology, all TFTs exhibit rather similar carrier mobilities *i.e.*, neither the grain geometry nor the grain boundary density nor the density of the ribbons affect the field-effect mobilities significantly. In fact, it is likely that the ribbons are distributed only on the upper surface of the DNTT layer and, hence, they neither contribute to nor disrupt the charge transport (the conducting channel is usually formed within the first few molecular layers the semiconductor). The outcome of this observation is that the field-effect mobilities of DNTT TFTs do not depend on the DNTT morphology.* We assume from this observation that neither the grain boundaries nor the ribbon-like aggregates in polycrystalline DNTT films form high-resistivity barriers that pose a significant limitation to the carrier mobility. This finding differentiates DNTT from a large number of small-molecule organic semiconductors, such as pentacene, for which the grain size has a direct influence on the field-effect mobility,[167] and the grain boundaries limit the charge transport and the overall device performance drastically.[168,169]

---

* Since in the measurements in this section not all of the TFTs are measured using the same V_{DS}, these measurements are not a reliable basis for the comparison between the threshold voltages in the devices and the on/off current ratios. A thorough study on the threshold voltage is presented in the next chapter.

5.6 Chapter conclusions

In this chapter three different methods of treating the Al_2O_3 surface (used as the gate oxide in DNTT TFTs) with the phosphonic acid SAMs, namely dip coating, microcontact printing and vacuum sublimation, have been studied and compared. The comparison of the performance of TFTs prepared with different SAM treatment methods allowed for a clear determination of dip coating as the most effective SAM treatment method. It was also shown that treating the gate oxide with the SAMs enhances the performance of DNTT TFTs compared to the untreated device.

A series of investigations were conducted to characterize bare Al_2O_3 and Al_2O_3 functionalized with three different phosphonic acid SAMs in terms of different surface properties, namely surface roughness, liquid contact angles and the surface energies. No clear correlation between the morphology of the DNTT islands in the first stages of the thin-film growth and the surface energies was found. DNTT TFTs made with bare Al_2O_3 and Al_2O_3 functionalized with SAMs exhibit an enhancement in the TFT parameters for the devices with the SAMs: modification of the gate-oxide surface with the phosphonic acid SAMs utilized in this chapter, resulted in improved field-effect mobilities and subthreshold swings and a more positive threshold voltage compared to the untreated devices.

Unlike the surface energy of the gate dielectric, the deposition rate of DNTT was found to influence the morphology of DNTT islands and thin films significantly. Interestingly, the differences in DNTT thin-film morphology induced by the various DNTT deposition rates do not have a noticeable effect on the electrical characteristics of the TFTs.

The main message of the present chapter, therefore, is discarding the impact of the DNTT morphology as a dominant factor on the performance of the DNTT TFTs.

Next chapter is devoted to a systematic study on the operating voltage of the TFTs, in which the gate oxides are selected precisely for this purpose.

6. Threshold-voltage shifts in DNTT transistors due to self-assembled monolayers

This chapter is about a prominent aspect of organic TFTs with SAMs at their gate-dielectric known as the *threshold-voltage shift*, which is the modification of the threshold voltage due to the presence of SAMs. The mechanisms behind the threshold-voltage shift by SAMs have been under debate for over a decade, and different explanations have been proposed. Although several hypotheses as the reason behind this phenomenon have been suggested, the community has not yet come to an agreement on a general mechanism and more importantly, some of the suggested hypotheses contradict each other.

The first section of this chapter consists of a detailed literature review on the topic with the purpose of building a complete picture of the mechanisms leading to the threshold-voltage shift phenomenon. The literature review is wrapped up with a comprehensive method, which decouples the impact of the different mechanisms that could be involved and thereby helps settle the debate. This method, which involves the investigation of the dependence of the threshold voltage on the gate-dielectric capacitance, will be employed systematically in two systems consisting of DNTT TFTs with the HC_{18}-PA SAM and the FC_{18}-PA SAM in combination with different gate-oxide thicknesses. KPFM measurements are performed to study the electrostatic potential originating from the SAMs as well as to gain insight into the electronic interactions between the SAMs and the DNTT.

6.1 Literature review

The mechanisms behind the threshold-voltage shift in organic transistors due to functionalizing the gate dielectric with SAMs are still under debate. Kobayashi *et al.* were among the first to introduce this effect by using various SAMs on a SiO_2 gate oxide in combination with pentacene and C_{60} as the semiconductors in p-channel and n-channel organic TFTs.[170] In a similar study, Pernstich *et al.* showed that functionalizing the SiO_2 gate oxides with different SAMs induces different threshold voltages in pentacene TFTs.[171] The mechanisms responsible for this phenomenon have been subject to intense discussions and investigations, and different explanations have been suggested.

Kobayashi *et al.* proposed that the threshold-voltage shift is related to the dipolar character of the SAM molecules, suggesting that the intrinsic dipole moment of the molecules that form the SAMs creates an electrostatic potential difference across the SAM, and this leads to charge accumulation at the interface between the organic semiconductor and the dielectric. These SAM-induced charges are compensated by an electric field externally applied across the gate dielectric. The electric field inside the SAM is expressed as the electrostatic potential difference across the SAM divided by its thickness (E_{SAM} = V_{SAM}/t_{SAM}), with V_{SAM} given by the Helmholtz equation as follows:

$$V_{SAM} = \frac{N_{SAM} \cdot P_z}{\varepsilon_0 \cdot \varepsilon_{SAM}}$$

Equation 6.1

where N_{SAM} is the molecular density of the SAM (the number of molecules per unit area), P_z is the perpendicular component of the dipole moment of the SAM, ε_0 is the vacuum permittivity, and ε_{SAM} is the relative permittivity of the SAM.

Following this line of argumentation, and assuming that the density of the dipole-induced charges accumulated at the semiconductor/dielectric interface, which has to be compensated by a gate field, is given by Q_{SAM} = $V_{SAM} \cdot C_{SAM}$, a general relation between the electrostatic potential of the SAM and the SAM-induced change in the threshold voltage (V_{th}) has been proposed:[171–174]

$$V_{th} = \frac{-Q_{SAM}}{C_{diel}} + \varphi = -\frac{C_{SAM} \cdot V_{SAM}}{C_{diel}} + \varphi$$

Equation 6.2

with C_{diel} being the capacitance per unit area of the oxide capacitor and the SAM capacitor connected in series (C_{diel} = $(1/C_{ox} + 1/C_{SAM})^{-1}$). Thus, for large oxide thicknesses, when $C_{diel} << C_{SAM}$, V_{th} can be drastically larger than V_{SAM}. The negative sign in the equation stands for the fact that the threshold-voltage shift is in fact the gate-voltage used for the

compensation of the SAM-induced charges (Q) or, in other words, for the induction of equal amount of charges with the opposite polarity (−Q). The term φ is introduced here to account for any contribution to the threshold voltage arising from parameters not related to the gate dielectric, such as the difference in workfunction between the gate electrode and the semiconductor.[175] In organic TFTs, φ is usually much smaller than the first term in Equation 6.2 and therefore it is often ignored. Any additional contribution from residual carriers or trapped charges are also assumed to be negligible in Equation 6.2.[172]

A conceptually different interpretation was proposed by Possanner *et al.*, who argued that actually two different physical effects of the SAMs must be considered. In the first case, a SAM composed of dipolar molecules can be modeled as an ideal parallel-plate capacitor, where the electric field only exists across the SAM and not outside. Therefore, the impact of the SAM manifests itself as an offset of the gate bias (approximately) equal to the absolute value of the electrostatic potential of the SAM, but opposite in sign, a situation equivalent to achieving flat-band condition:[176]

$$V_{th} = -V_{SAM}$$
<div align="right">Equation 6.3</div>

This view, which is shared by Chung *et al.*,[122] cannot account for the observation that the threshold voltages of TFTs based on certain SAMs can be several tens of volts,[170,171,174] while values for V_{SAM} are never greater than a few volts.[174,177] The second effect therefore, discussed by Possanner *et al.* is the SAM-induced formation of a space-charge layer at the semiconductor-dielectric interface that is compensated by a gate bias $V_{GS} = V_{th}$ with the following value:

$$V_{th} = -\frac{\sigma}{C_{diel}}$$
<div align="right">Equation 6.4</div>

The interfacial charge density σ can originate from charge transfer or a chemical reaction between the SAM and either the organic semiconductor or the oxide,[178–180] or from a modification of the density of states in the semiconductor,[123] and it may also include a contribution from interface trap states. **Figure 6.1** summarizes the three most widely-discussed explanations on the threshold-voltage shift that were introduced above.
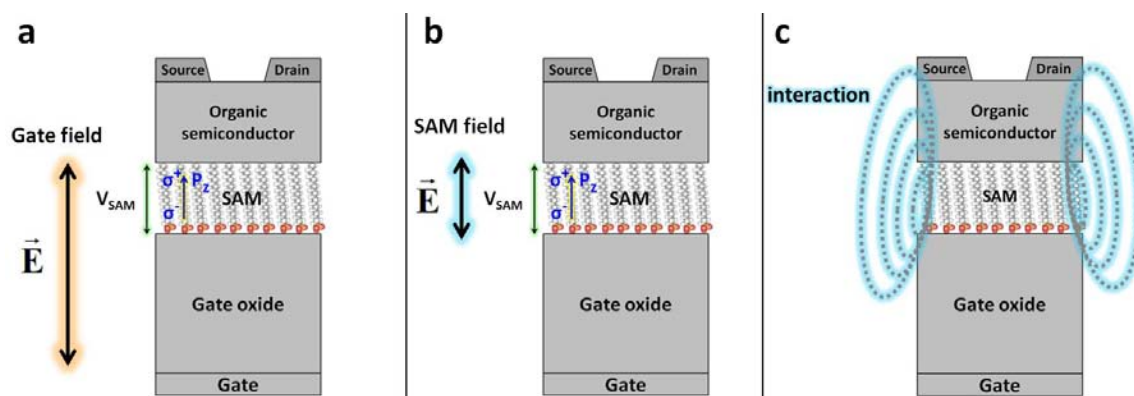
Figure 6.1: Schematic cross section of an organic TFT summarizing the impact of the SAMs on the threshold-voltage shift when a) the SAM-induced charges are compensated by an electric field across the gate (Equation 6.2), b) the SAM acts as an ideal parallel-plate capacitor leading to an electric field only across the SAM (Equation 6.3), c) there is an interaction at the organic semiconductor/SAM/gate-oxide interface leading to the formation of a space-charge layer (Equation 6.4).

The presence of a space-charge layer implies the dependence of the threshold voltage on the capacitance of the entire gate dielectric ($V_{th} \propto 1/C_{diel}$), analogous to Equation 6.2 and in stark contrast Equation 6.3. But unlike Equation 6.2 and Equation 6.3, Equation 6.4 does not include an explicit relation with the dipolar character of the SAM.

All of the above-mentioned interpretations are based on the common ground that the SAM changes the carrier density in the semiconductor and thereby it shifts the threshold voltage. The controversy pertains to the physical or chemical mechanism(s) by which the SAM produces the observed changes in carrier density and the threshold voltage, and to the question, whether the threshold voltage depends on the gate-dielectric capacitance (Equation 6.2 and Equation 6.4), or it is independent of it (Equation 6.3). A common approach to investigate the effect of the SAMs on the threshold voltage is to fabricate TFTs with SAMs based on dipolar molecules and analyze the dependence of the threshold voltage on the calculated molecular dipole moment or the interfacial charge density expected from the calculated dipole moments.[122,172–174,179,181] One limitation of this approach is that the actual dipole moment of a SAM may differ from the dipole moment calculated for an individual free molecule, and that depolarization effects may be important. In addition, more than one mechanism may be involved when SAMs with different characteristics (*e.g.,* chain length, chemical nature of the anchor group and/or the functional group) are employed.

Detailed investigations on the relation between the threshold voltage and the dipole moment of the SAMs and other mechanisms involved in the threshold-voltage shift induced by SAMs will be discussed in the following sections.

6.2 Transistor characteristics and threshold voltage

In order to find out by which mechanism(s) the SAMs shift the threshold voltage, we have investigated TFTs with different gate dielectric capacitances. The TFTs were fabricated in a bottom-gate, top-contact architecture on silicon substrates with Al_2O_3/SAM gate dielectrics with Al_2O_3 thicknesses of 5 nm,* 10 nm, 50 nm, 100 nm or 200 nm deposited by ALD. The oxide surfaces were functionalized with either the HC_{18}-PA SAM or the FC_{18}-PA SAM SAMs by dip-coating. **Figure 6.2** shows schematics of the two sets of dielectrics used in this work.

As introduced in the previous chapter, the HC_{18}-PA the FC_{18}-PA molecules are composed of a chain length of 18 carbon atoms but the functional (head) groups are different. The different chain terminations lead to different dipole moments that could induce different carrier densities in the semiconductor by affecting the chemistry at the SAM/semiconductor interface. However, since the height of the molecules, the nature of the anchor group and the processing conditions are identical, the two types of SAMs have very similar insulating characters. Therefore, the effects of the different chain terminations (hydrogenated *vs.* fluorinated) can be decoupled from factors such as thickness of the layer and bonding to the gate oxide.
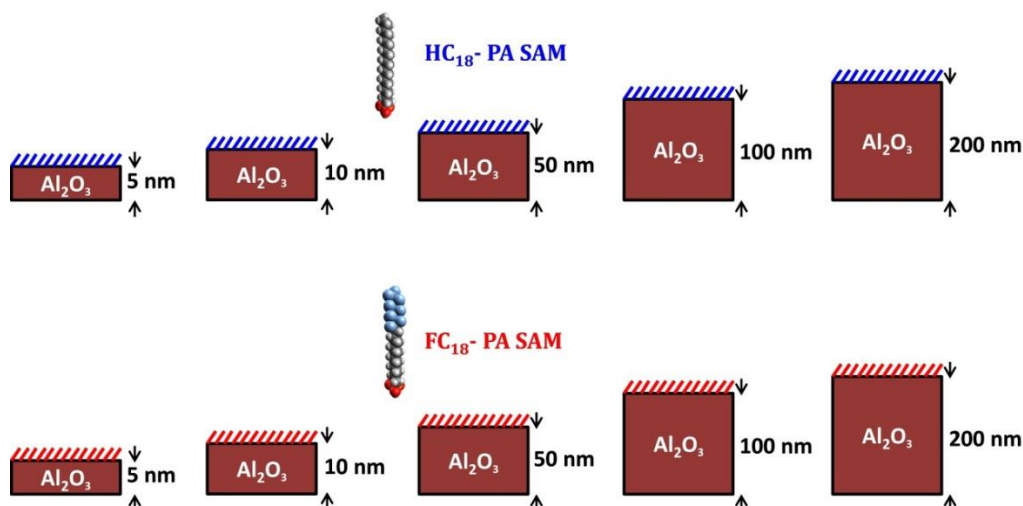
Figure 6.2: Schematic of two sets of dielectrics consisting of five different Al_2O_3 thicknesses and two different phosphonic-acid SAMs (the HC_{18}-PA and the FC_{18}-PA).

A successful SAM treatment results in a hydrophobic gate-dielectric surface (as seen in the previous chapter), which provides the additional benefit of preventing the adsorption of

---

* For the 5 nm thick oxide, the native silicon dioxide was removed in dilute hydrofluoric acid prior to the Al_2O_3 deposition.

dipolar water molecules. **Table 6.1** and Figure 6.3 indicate that the water contact angles of Al_2O_3 surfaces treated with the HC_{18}-PA and the FC_{18}-PA SAM are determined by the type of the SAM and that it is independent of the oxide thicknesses. This observation confirms that these substrates provide a good basis for comparison.

In addition to the water contact angle measurements, hexadecane (a non-polar liquid) contact angle measurements (see **Table 6.2**), confirm the formation of closely-packed SAMs of alkyl and fluoroakyl molecules exposing, respectively, the CH_3 and the CF_3 groups to the air/film interface.[182] The measured hexadecane contact angles shown below are in good agreement with the previously reported values in the literature.[161,182]

Al_2O_3 thickness	Water contact angle obtained from HC_{18}-PA SAM	Water contact angle obtained from FC_{18}-PA SAM
5 nm	107°	119°
10 nm	108°	119°
50 nm	107°	118°
100 nm	108°	118°
200 nm	108°	119°

Table 6.1: Water contact angles measured on silicon substrates coated with a 5 nm, 10 nm, 50 nm, 100 nm or 200 nm thick layer of Al_2O_3 and treated with the HC_{18}-PA SAM or the FC_{18}-PA SAM.
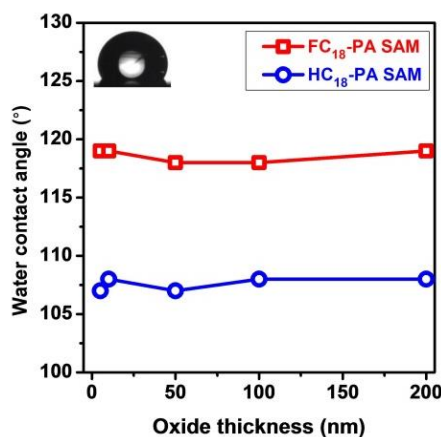
Figure 6.3: Water contact angle *vs.* oxide thickness, showing that the water contact angle does not depend on the oxide thickness.

Substrate	Water contact angle	Hexadecane contact angle
Bare Al_2O_3 directly after plasma treatment	N/A*	10°
Al_2O_3 treated with HC_{18}-PA SAM	107°	41°
Al_2O_3 treated with FC_{18}-PA SAM	118°	71°

Table 6.2: Water and hexadecane contact angles on silicon substrates coated with a 10 nm thick layer of Al_2O_3 before and after the SAM treatment. (*not applicable: the contact angle measurement is not possible due to a complete wetting of the substrate)

The SAM-treated substrates are used as gate dielectrics and coated with a 25 nm thick layer of DNTT deposited in vacuum and the TFT devices are finished up by the deposition of the gold source and drain contacts patterned using a shadow mask. The schematic cross-section of the TFTs with 5 different Al_2O_3 thicknesses is shown in **Figure 6.4**.
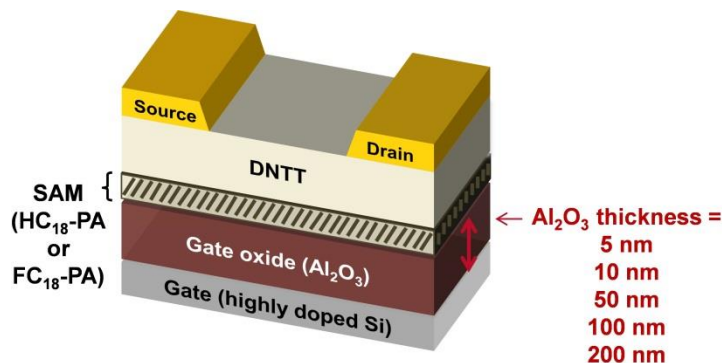
Figure 6.4: Schematic cross-section of the TFTs, fabricated with five different Al_2O_3 thicknesses and two different phosphonic-acid SAMs (the HC_{18}-PA or the FC_{18}-PA).

The effect of the oxide thickness (also the oxide capacitance) and the SAM type on the threshold voltage of the TFTs can be analyzed by measuring the current-voltage characteristics of the devices. The field-effect mobilities were extracted from the transfer characteristics in the linear regime ($V_{DS} = -0.1$ V). **Figure 6.5** shows a plot summarizing the corresponding carrier mobilities. As can be seen, regardless of the oxide thickness and the type of the SAM, all TFTs exhibit field-effect mobilities ranging from nearly 2 cm^2/Vs to 3.5 cm^2/Vs, similar to the highest field-effect mobilities obtained for DNTT TFTs in the previous chapter and the ones reported in the literature.[33,183,184]
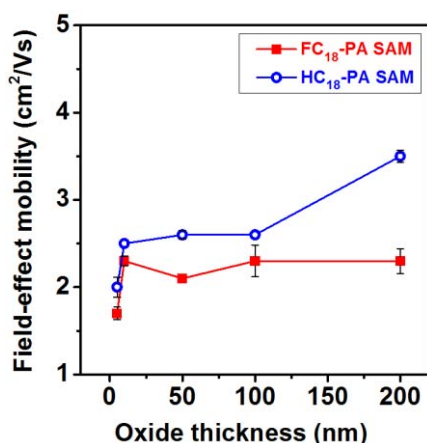
Figure 6.5: The field-effect mobilities obtained from ten sets of TFTs based on five different Al_2O_3 thicknesses and two different SAMs (the HC_{18}-PA and the FC_{18}-PA) plotted as a function of the Al_2O_3 thickness (with statistical error bars from 5-10 TFTs for each set of samples).

To obtain the threshold voltages of the TFTs, the measured transfer curves were fitted to the basic FET equation (Equation 2.5). Employing this equation, in addition to the use of known parameters such as the field-effect mobility, the TFT channel dimensions, the gate-source voltage and the drain-source voltage (here −0.1 V), requires knowing the value of the gate-dielectric capacitance for each oxide thickness. A precise and reliable measurement of the gate-dielectric capacitance is possible by patterning the substrate with a special geometry using a shadow mask in a way that the active capacitance area is influenced during the measurement procedure. Using ALD-deposited Al_2O_3 oxides poses the limitation of such patterning of the substrate since ALD is deposited as a global layer and thus cannot be patterned. Therefore, the gate-dielectric capacitance (C_{diel}) was calculated using the equation below:

$$C_{diel} = \left(\frac{1}{C_{ox}} + \frac{1}{C_{SAM}}\right)^{-1} = \varepsilon_0 \left(\frac{t_{ox}}{\varepsilon_{ox}} + \frac{t_{SAM}}{\varepsilon_{SAM}}\right)^{-1}$$

Equation 6.5

where t_{ox} is the oxide thickness (5 nm, 10 nm, 50 nm, 100 nm or 200 nm), ε_{ox} is the relative permittivity of Al_2O_3 (ε_{ox} = 9),[67] t_{SAM} is the thickness of the SAM (2.1 nm),[185] and ε_{SAM} is the relative permittivity of the SAM (ε_{SAM} = 2.5 for the HC$_{18}$-PA SAM, ε_{SAM} = 2.2 for the FC$_{18}$-PA SAM).[186] The calculated gate-dielectric capacitance values are shown below in **Table 6.3**. For the smallest oxide thickness (5 nm), the calculations were confirmed by frequency-dependent capacitance measurements shown below in **Figure 6.6**. The suitable layout for this capacitance measurement is also indicated in the optical micrograph shown in **Figure 6.6**, with the capacitor active area consisting of a square of 60 μm × 60 μm dimensions. Such a layout with an ALD-deposited Al_2O_3 oxide is only achievable when the thinnest Al_2O_3 oxide is employed. The reason is that the alignment of the shadow mask for the top electrodes of the capacitor is only possible when the bottom electrodes are visible to the eye, *i.e.,* when the Al_2O_3 layer is sufficiently thin (= 5 nm).

Al_2O_3 thickness [nm]	Al_2O_3/HC$_{18}$-PA SAM capacitance [nFcm^{-2}]	Al_2O_3/FC$_{18}$-PA SAM capacitance [nFcm^{-2}]
5	650	580
10	450	430
50	140	140
100	74	73
200	38	38

Table 6.3: The gate-dielectric capacitance values (calculated using Equation 6.5) based on five different Al_2O_3 thicknesses and the HC$_{18}$-PA SAM or the FC$_{18}$-PA SAM.
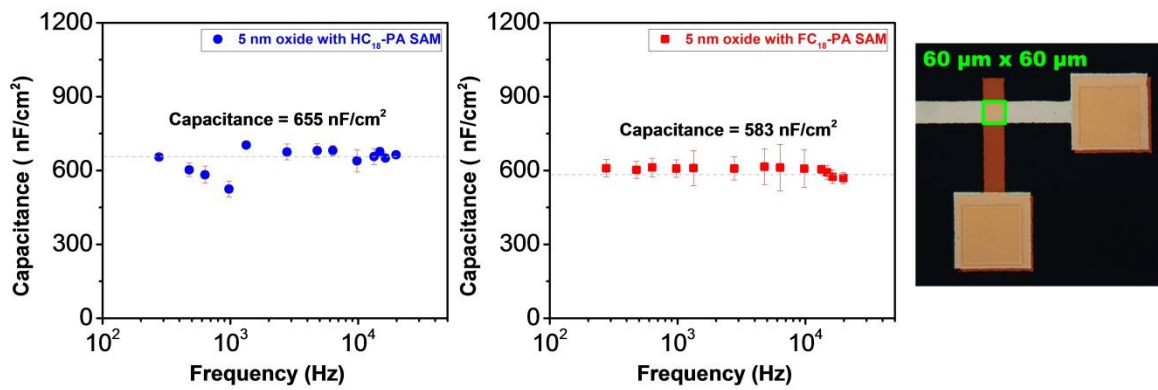
Figure 6.6: Frequency-dependent capacitance plots (with standard deviations) measured on capacitors formed by a sandwich of $Al/Al_2O_3/SAM/Au$ patterned using two different shadow masks. The active capacitor area is marked in the optical micrograph.

With the capacitance values, the threshold voltage from the transfer curves were estimated and shown in **Figure 6.7**. In each transfer curve, the threshold voltage is indicated and marked with a vertical line.

Table 6.4 shows the parameters of the transistors with the HC_{18}-PA SAM and the FC_{18}-PA SAM. The threshold voltages are indicated with statistical error bars from measuring 5 to 10 TFTs for each set of samples.
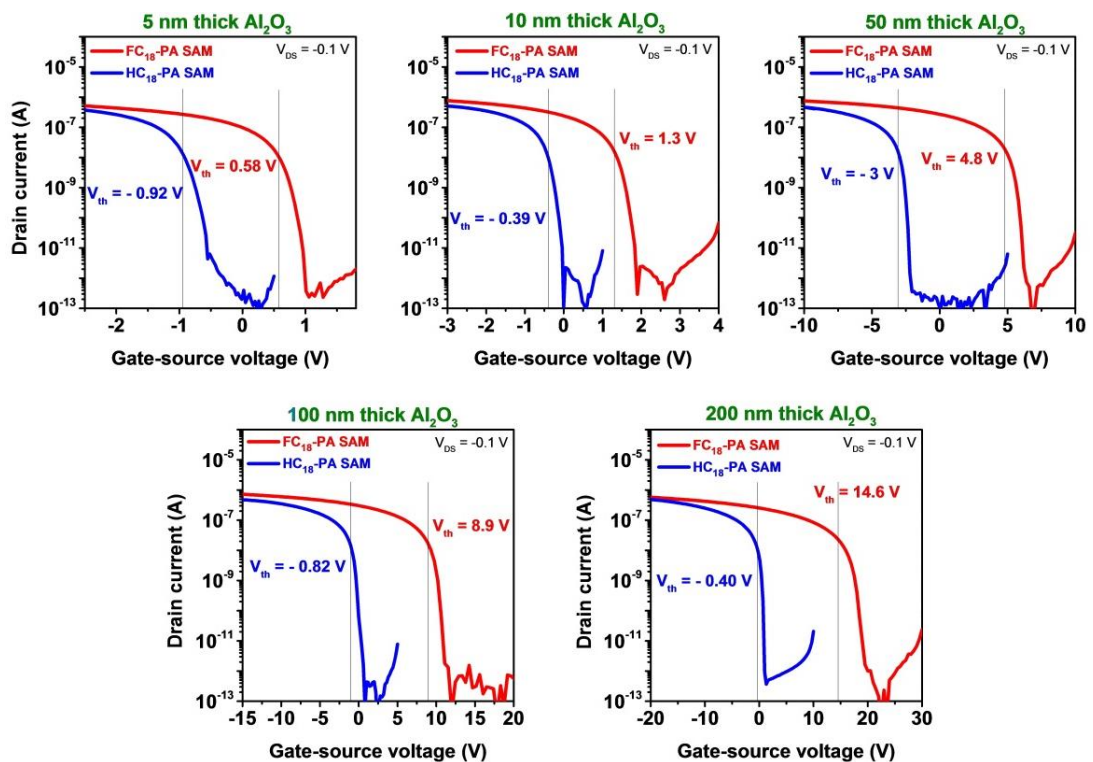
Figure 6.7: Transfer characteristics of DNTT TFTs (linear regime $V_{DS} = -0.1$ v) based on five different Al_2O_3 thicknesses and the HC_{18}-PA SAM and the FC_{18}-PA SAM.

Al_2O_3 thickness (nm)	threshold voltage (V)	field-effect mobility (cm^2/Vs)	subthreshold swing (mV/decade)	On/ off current ratio
HC$_{18}$-PA SAM				
5	−0.92 ± 0.02	2	97	10^6
10	−0.39 ± 0.03	2.5	98	10^6
50	−3.0 ± 0.07	2.6	275	10^6
100	−0.82 ± 0.07	2.6	320	10^6
200	−0.40 ± 0.18	3.5	313	10^6
FC$_{18}$-PA SAM				
5	+0.58 ± 0.01	1.6	104	10^6
10	+1.3 ± 0.01	2.3	139	10^6
50	+4.8 ± 0.07	2.1	386	10^6
100	+8.9 ± 0.18	2.4	1203	10^6
200	+14.6 ± 0.14	2.3	764	10^6

Table 6.4: Parameters from TFTs based on five different Al_2O_3 thicknesses and two different SAMs (top HC$_{18}$-PA SAM, bottom FC$_{18}$-PA SAM)

The threshold voltages of the TFTs based on the five different oxide thicknesses and the two different SAMs (extracted from the transfer curves of **Figure 6.7**) have been plotted versus the gate-dielectric capacitances as shown in the **Figure 6.8**. This figure shows that the threshold voltages of the TFTs with the HC$_{18}$-PA SAM do not exhibit any systematic dependence on the gate-dielectric capacitance. In contrast, it appears that in the TFTs with the FC$_{18}$-PA SAM increasing the dielectric thickness leads to more positive V_{th}, where a linear dependence on the inverse of the gate-dielectric capacitance ($V_{th} \propto 1/C_{diel}$) can be seen. The chain terminations in the two types of SAMs (hydrogenated *vs.* fluorinated) that may develop different characteristics (such as dipole moments and electrostatic potentials induced by SAM dipoles) could lead to a clue about the difference between the two plots in **Figure 6.8**.
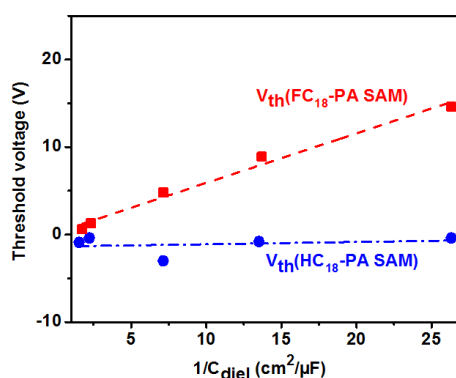
Figure 6.8: Threshold voltage *vs.* inverse of the gate-dielectric capacitance for TFTs based on five different Al_2O_3 thicknesses and the HC$_{18}$-PA SAM or the FC$_{18}$-PA SAM.

Note that the main emphasis in this chapter is the impact of SAMs on the threshold voltage and therefore devices with different Al_2O_3 thicknesses without the SAMs were not investigated. In **Figure 6.9**, the transfer characteristic of DNTT transistors based on a 10 nm thick layer of Al_2O_3 gate-dielectric without the SAMs are represented. The devices were measured directly after fabrication over a short period of time. As can be seen, it is not feasible to assign a threshold voltage value to these set of TFTs, because of the evolving threshold voltage values with a tendency to shift towards more positive values. These devices exhibit an ongoing shift of the threshold voltage that can reach around 0.7 V during the measurement. The reason is that oxide surfaces without the SAM passivation are characterized by a significant density of hydroxyl groups and hence a significant density of charge traps. They are also hydrophilic and thus, usually covered with a thin layer of water and air-borne contaminants. This character of the untreated oxide surfaces can also influence the field-effect mobilities in the untreated devices. The mobilities in the devices discussed in **Figure 6.9** are around 0.2 cm^2/Vs to 0.3 cm^2/Vs, which is an order of magnitude lower than the ones obtained from the devices with the SAMs. The performance of the DNTT TFTs shown below is the evidence that the characteristics of the TFTs with oxide surfaces without the SAM passivation are ill-defined and not a good basis for comparison.
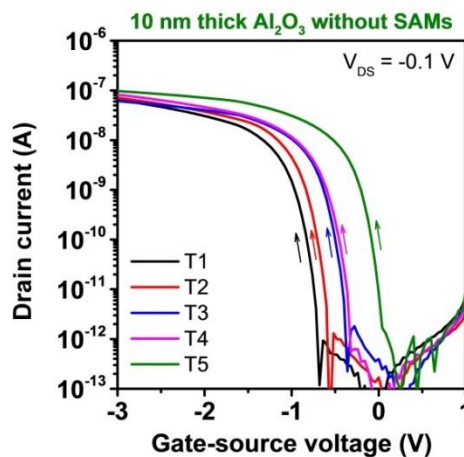
Figure 6.9: Transfer characteristics of five DNTT TFTs (forward sweeps in the linear regime V_{DS} = −0.1 V) on 10 nm thick Al_2O_3 without SAMs measured directly after fabrication. The figure clearly marks the instability of the threshold voltage as a result of the non-passivated Al_2O_3 surface.

6.3   Electrostatic potential measurements on the SAMs

In order to understand the impact of the SAM on the threshold voltage, it is important to have a measure of the electrostatic potential generated by the SAM (V_{SAM}).

Table 6.5 indicates the values for the dipole moments and relative dielectric constants taken from a work by Jedaa *et al..*[186] The molecular packing densities are taken from the literature either directly or were calculated for a close hexagonal packing of the molecules using the van der Waals radius of the chains.

SAM type	Molecular dipole moment [D]	Molecular density of the SAM [$\times 10^{14}\,cm^{-2}$]	Relative dielectric constant	Electrostatic potential predicted by Equation 6.1 [V]
HC$_{18}$-PA	−1.07	4.55 ([122]) to 5.4 ([187])	2.5	+0.74 to +0.88
FC$_{18}$-PA	2.79	3.33 ([188]) to 3.7 ([189])	2.2	−1.6 to −1.77

Table 6.5: Dipole moments of individual HC$_{18}$-PA and FC$_{18}$-PA molecules, and molecular density, relative dielectric constants and electrostatic potentials of the HC$_{18}$-PA and FC$_{18}$-PA SAMs calculated from Equation 6.1.

Since the actual electrostatic potential may differ from the value predicted by Equation 6.1 due to charge rearrangements, depolarization effects (dipole-dipole interactions) and substrate-molecule interactions,[190] we employed KPFM, as a non-invasive method, to obtain the electrostatic potential on the surface. Since KPFM measures the contact-potential difference (CPD) between the surface and the probe tip, a quantitative determination of electrostatic potential independent of tip effects requires using a surface reference. Moreover, the same tip must be used for the comparison between different KPFM measurements. We have measured a freshly-cleaved highly oriented pyrolytic graphite (HOPG) specimen subsequent to each measurement as a reference to make sure the probe tip has not changed. The topography and the electrostatic potential maps of the bare Al$_2$O$_3$ surface as well as those obtained after the treatment with the two SAMs, are shown in **Figure 6.10**.
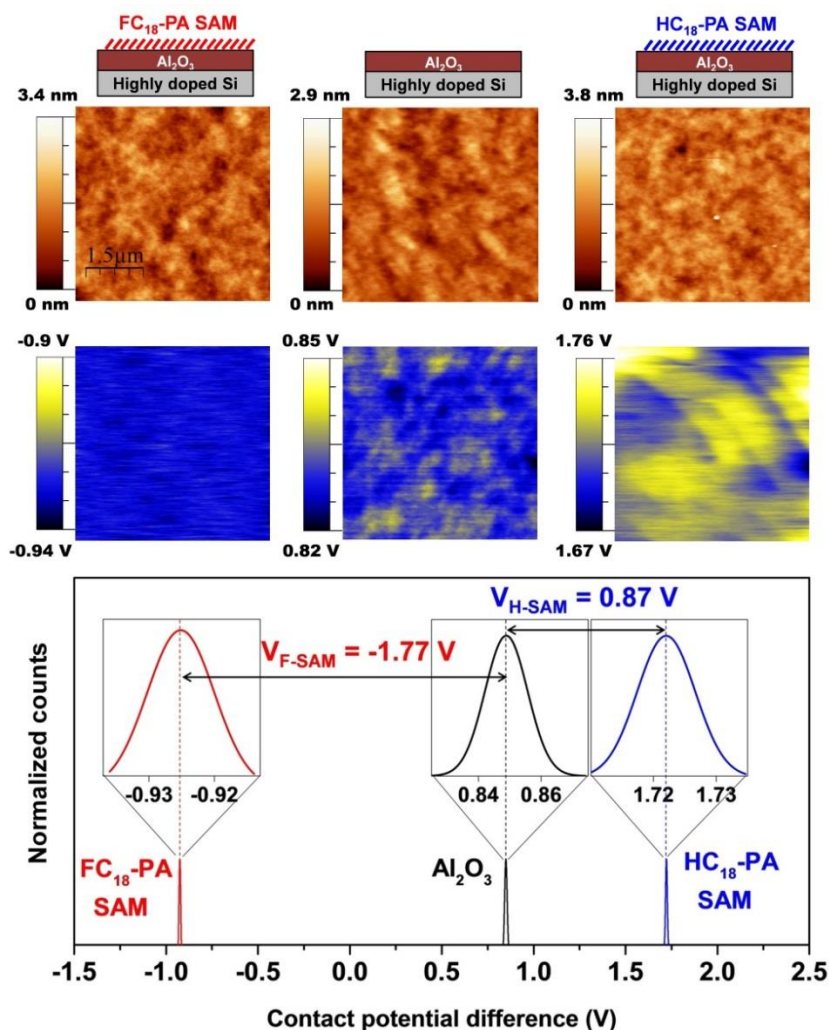
Figure 6.10: Estimation of electrostatic potential of the SAMs: Topography images measured by AFM (first row) and electrostatic potential maps measured by KPFM (second row) of an Al_2O_3 surface without SAM (center), of an Al_2O_3 surface covered with a FC_{18}-PA SAM (left), and of an Al_2O_3 surface covered with a HC_{18}-PA SAM (right) (all images are 5 μm × 5 μm). The graph shows the CPD histograms obtained from the three KPFM images.

Note that in **Figure 6.10** there is no correlation between the morphology in the topography images and the contact potential maps, indicating no crosstalk between the two, allowing for the surface potential determination as the average value of the whole image in each case. The figure also represents the histograms obtained from the surface potential maps of the bare Al_2O_3 surface as well as those obtained after the functionalization with the two SAMs. From the surface potential histograms shown in **Figure 6.10**, electrostatic potentials (relative to the Al_2O_3 surface) of +0.87 V for the HC_{18}-PA SAM and −1.77 V for the FC_{18}-PA SAM are obtained. Comparison between the experimentally-determined V_{SAM} values measured by KPFM and the values indicated in **Table 6.4** suggests a good agreement between the measured values and the V_{SAM}

calculated using Equation 6.1 for the densest packing of the chains according to the literature.

A cross-check experiment was performed using grounded gold contacts on each SAM as the reference for the calibration of the work function of the probe tip, making sure that no charging or discharging of the samples occurs via the probe tip. In this measurement, an Au electrode was deposited onto each substrate and connected to ground potential. This grounded Au contact served as an in-situ reference for the workfunction of the tip. The results are summarized in **Figure 6.11**.

The graph in **Figure 6.11** indicates that the difference between the potentials of the two SAMs obtained from the CPD histograms (ΔV_{SAM} = 3.1 V) is slightly larger in magnitude than the one obtained from the measurements in which HOPG served as a reference in **Figure 6.10** (ΔV_{SAM} = 2.6 V). However, we believe the values measured relative to the HOPG reference are more reliable, since the deposited gold contact may affect the local electronic properties of the SAM underneath.

Note that in this section up to this point, the substrate consists of Si (the native oxide was removed in HF solution) coated with 5 nm of ALD-deposited Al_2O_3. A valid question that might arise here is, if the presence of the SAMs on the 5 nm oxide leads to the same magnitude of V_{SAM} as it does on the thicker oxides. Although it seems rather clear that the electrostatic potential of the SAMs originates from the dipole moment of the SAM and thus it does not depend on the capacitance of the substrate underneath, this assumption will be confirmed on the basis of experimental evidence in the following.
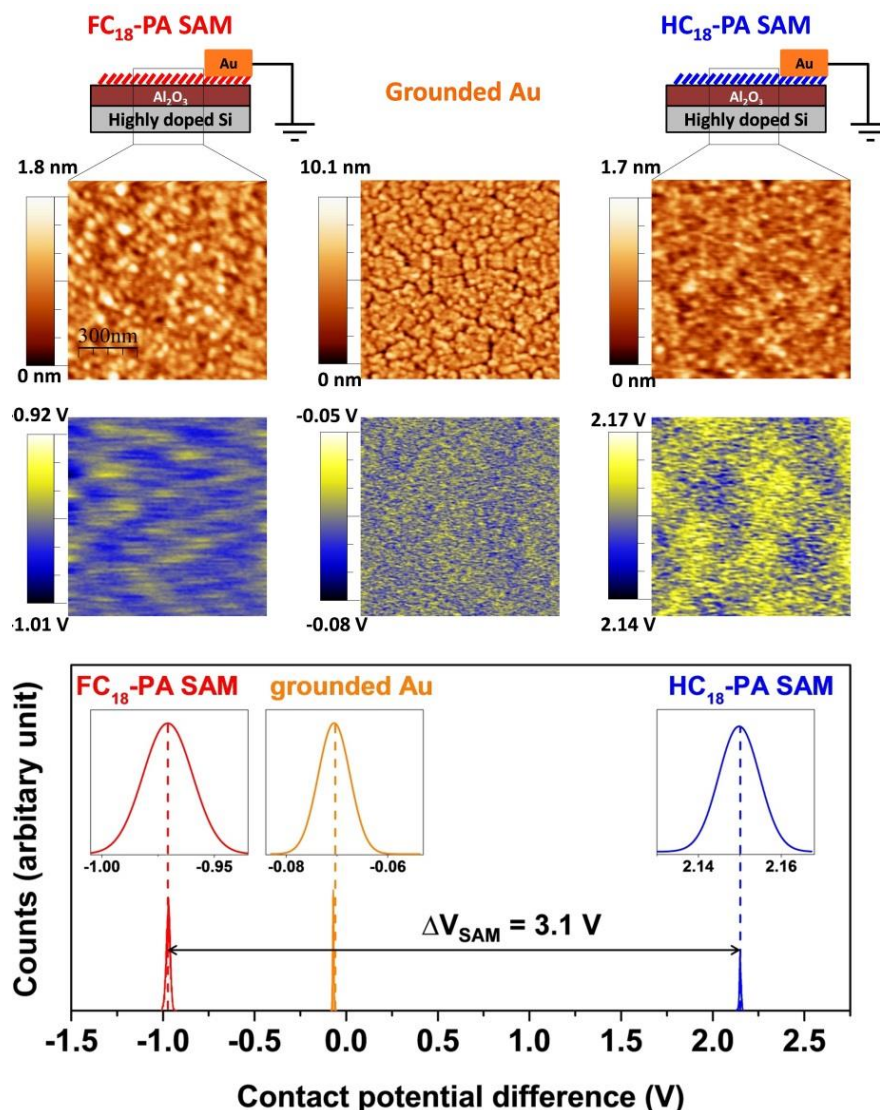
Figure 6.11: Estimation of electrostatic potential of the SAMs: The AFM topography images (first row) and KPFM electrostatic potential maps (second row) of an Al_2O_3 surface covered with a FC_{18}-PA SAM, of an Al_2O_3 surface covered with a HC_{18}-PA SAM and of a grounded Au electrode (all images are 1 µm × 1 µm). The V_{SAM} values are illustrated with the CPD histograms.

Two substrates have been employed with the lowest Al_2O_3 layer thickness (5 nm) and the highest Al_2O_3 layer (200 nm) functionalized with arrays of both SAMs which were produced by a combination of microcontact printing (of the FC_{18}-PA) and dip coating (for the formation of the HC_{18}-PA SAM). Using this method, the CPD between the two SAMs can be measured in uninterrupted single measurements.

The difference between the electrostatic potentials produced by the two SAMs (indicated by the line profiles in the **Figure 6.12**) is about 0.6 V on both substrates. This observation confirms the assumption that the potential of the SAM, produced by the dipole moment of the array of molecules that form the SAMs, is independent of the thickness of the gate

oxide underneath the SAMs. On that ground, we can use the measured V_{SAM} for the thickness of 5 nm oxide (indicated in **Figure 6.10**) for all TFTs in this study despite the different oxide thicknesses.
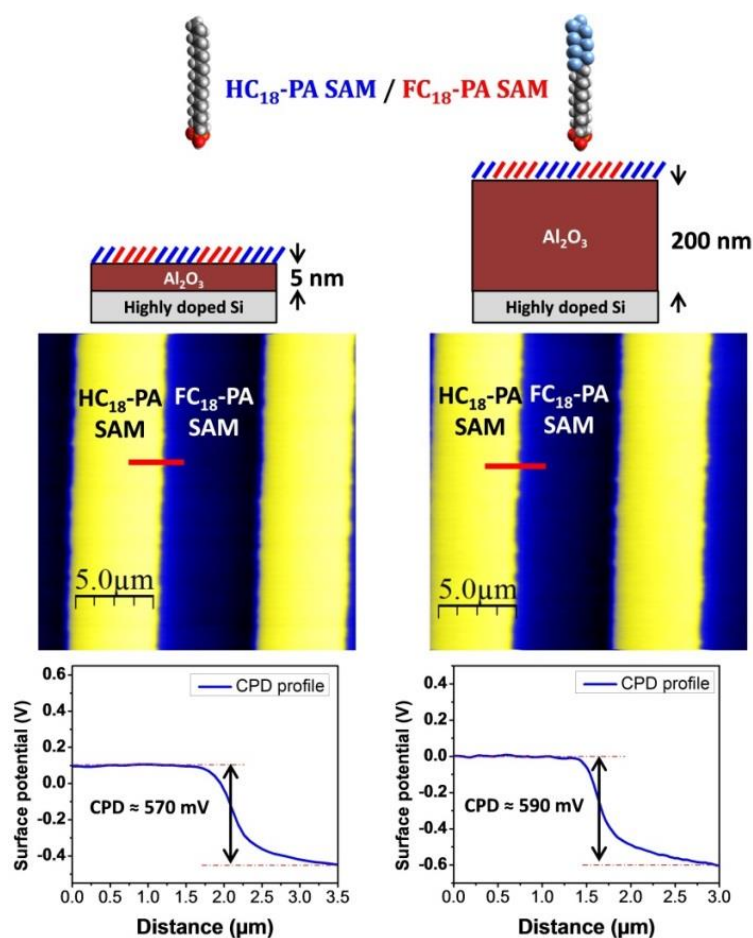
Figure 6.12: KPFM potential maps of 2 substrates (with 5 nm oxide and 200 nm oxide) patterned with the HC_{18}-PA SAM and the FC_{18}-PA SAM. The line profiles indicate that the CPD between the two SAMs is independent of the oxide thickness.

Note that the potential difference obtained here (~ 0.6 V) is significantly smaller than the potential difference measured in **Figure 6.10** and **Figure 6.11**. This discrepancy is possibly related to the fact that the experiments illustrated in **Figure 6.10** and **Figure 6.11** were performed on dense monolayers, while the substrate investigated here, consist of a microcontact-printed SAM. As discussed in the previous chapter, in Section 5.1, microcontact-printing is likely to result in less densely-packed monolayers in comparison to the SAMs formed by dip coating (samples in **Figure 6.10** and **Figure 6.11**).

Comparing the measured threshold voltages (**Table 6.4**) with the measured electrostatic potentials of the SAMs, it is clear that the threshold voltages of the TFTs with the FC_{18}-PA SAM are significantly larger than the electrostatic potential of this SAM, at least when the oxide thickness is greater than a few tens of nanometers. For example, for an oxide

thickness of 200 nm, the absolute value of the threshold voltage of the TFTs with the FC_{18}-PA SAM ($\sim$ +15 V) is almost an order of magnitude larger than the absolute value of the measured electrostatic potential of this SAM (1.77 V). This shows that for TFTs with the FC_{18}-PA SAM, Equation 6.3 does not hold.

6.4 Relationship between threshold voltage and gate-dielectric capacitance

In addition to the measured threshold voltages of TFTs with the HC_{18}-PA SAM or the FC_{18}-PA SAM, the threshold voltages can be calculated using Equation 6.2. Therefore, Equation 6.2 has been employed to calculate the threshold voltages of the TFTs with the two SAMs using the measured electrostatic potentials by KPFM and the gate-dielectric capacitances represented in **Table 6.5**. With these experimentally-determined values and the predicted values, we investigate the dependence of the threshold voltage on the gate-dielectric capacitance. The summarized results are plotted and shown in **Figure 6.13**, where **Figure 6.8** is merged together with data calculated using Equation 6.2 for comparison.
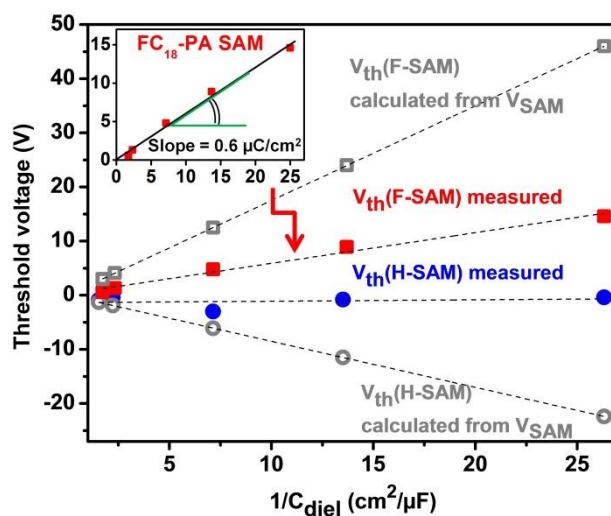
Figure 6.13: Measured threshold voltages (see **Table 6.4**) and threshold voltages calculated from V_{SAM} using Equation 6.2 (using the electrostatic potentials measured by KPFM, *i.e.,* +0.87 V for the HC_{18}-PA SAM and −1.77 V for the FC_{18}-PA SAM plotted as a function of the inverse of the gate-dielectric capacitance. The inset illustrates how the charge density σ is obtained from the slope of the linear fit using Equation 6.4.

As can be seen, for both SAMs there is a significant disagreement between the measured and the theoretically predicted values. The measured threshold voltages of the TFTs with the HC_{18}-PA SAM (blue circles) exhibit an average value of −0.64 V without any systematic

dependence on the gate-dielectric capacitance, in contrast to the predicted threshold voltages from Equation 6.2 ($V_{th} \propto 1/C_{diel}$) where the calculated values are shown by the grey open circles. This value is close to the measured electrostatic potential of the HC$_{18}$-PA SAM (0.87 V), but with opposite polarity ($V_{th} \approx -V_{SAM}$), a result that is in agreement with the dipole-layer scenario proposed by Possanner et al.[176] and the experimental results from Chung et al..[122] We infer from this observation that the main effect of the oxide functionalization with the HC$_{18}$-PA SAM is the passivation of the charge traps at the oxide surface.[91]

Unlike the threshold voltages of the TFTs with the HC$_{18}$-PA SAM, which are independent of the gate-dielectric capacitance, the measured threshold voltages of the TFTs with the FC$_{18}$-PA SAM (red squares) show a linear dependence on the inverse of the gate-dielectric capacitance ($V_{th} \propto 1/C_{diel}$). However, the slope of this linear relationship is only 0.6 µCcm^{-2} (shown as inset to **Figure 6.13**), which is significantly smaller than the slope obtained from a linear fit to the calculated values by Equation 6.2 (1.8 µCcm^{-2} for $C_{SAM} = 1$ µFcm^{-2} and $V_{SAM} = -1.77$ V).

Thus, for both SAMs it is clear that Equation 6.2 does not apply in practice, which raises the question whether there is a general relation between the dipole moment of the SAM and the threshold voltage of the TFTs, and whether this relation applies universally to all types of SAMs.

The linear relation between V_{th} and $1/C_{diel}$ for TFTs with the FC$_{18}$-PA SAM can be understood in terms of the space-charge layer described by Equation 6.4. The interfacial charge density responsible for the observed $V_{th} \propto 1/C_{diel}$ dependence (see inset in **Figure 6.13**) is estimated to be $\sigma \approx -0.6$ µCcm$^{-2} = -3.5 \times 10^{12}$ ecm^{-2}, causing accumulation of holes in the channel and leading to a value comparable to SAM-induced charge densities estimated experimentally for pentacene TFTs,[171,191] 6PTTP6 TFTs[173] and also to theoretical simulations.[176]

It is worth mentioning that in spite of the different behavior of the V_{th}, TFTs with the FC$_{18}$-PA SAM do not show hysteresis between the forward and backward sweeps of the transfer curves (shown in the **Figure 6.14**). Since hysteresis in organic TFTs is often associated with charge carrier trapping by shallows traps in the semiconductor close to the dielectric interface or associated with mobile charge carriers and mobile ions in the semiconductor or in the dielectric,[54] hysteresis-free transfer curves provide indication of absence of such effects and no or minor charge trapping of free carriers during operation of TFTs treated with the FC$_{18}$-PA SAM.
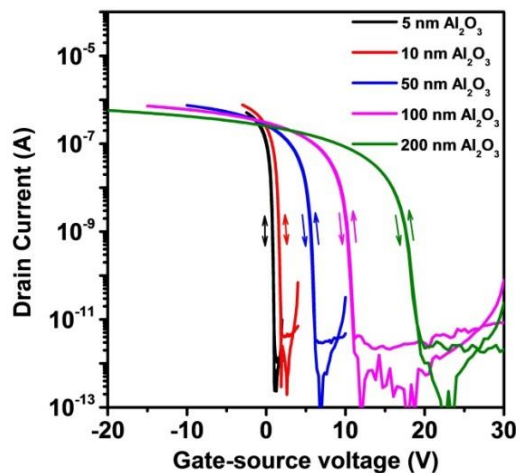
Figure 6.14: Hysteresis-free transfer curves (forward and backward sweeps in the linear regime $V_{DS} = -0.1$ V) of the TFTs functionalized with the FC_{18}-PA SAM on 5 different dielectric thicknesses (on silicon substrates coated with a 5 nm, 10 nm, 50 nm, 100 nm or 200 nm thick layer of Al_2O_3).

In addition, the transfer curves shown in **Figure 6.14** exhibit rather steep subthreshold swings, which is compelling evidence that the interfacial charge density is not caused by shallows traps in the semiconductor.

The fact that the relationship between the gate-dielectric capacitance and the threshold voltage is so different depending on the choice of the SAM ($V_{th} \approx$ const. for the TFTs with the HC_{18}-PA SAM $vs.$ $V_{th} \propto 1/C_{diel}$ for those with the FC_{18}-PA SAM) could be related to the presence of the two different chemical species (hydrogenated termination of the HC_{18}-PA SAM $vs.$ the fluorinated termination of the FC_{18}-PA SAM) at the interface. The fluorine substituents of the FC_{18}-PA molecules, which are known to be strongly electronegative, are located directly at the semiconductor/SAM interface and likely to have a decisive influence on the electronic characteristics of this interface. Before analyzing this matter, it is important to explore the possible influence of the selected SAMs on the semiconductor morphology.

6.4.1 Ruling out the impact of semiconductor morphology on the threshold voltage

From the investigation of DNTT morphology in the previous chapter, we have learned that deposition of DNTT onto different SAMs with different surface energies induces structural differences in the DNTT morphology (Chapter 5, Section 5.2). We also established that the deposition rate of DNTT can lead to a difference in the morphology (similar to the one due to the use of different SAMs), such as differences in the grain geometries, grain size and grain boundary density (Section 5.4). Therefore, by inducing different DNTT morphologies

by manipulation of the DNTT deposition rate, we have studied the effect of DNTT morphology independent of any other effect. In the Section 4.5 we have established that there is no significant correlation between the DNTT morphology and the field-effect mobilities in TFTs. Here the validity of our previous finding will be briefly crosschecked for TFTs with Al_2O_3 gate-dielectrics with the threshold voltage being in the spotlight.

Figure 6.15 shows the measured transfer characteristics of 4 TFTs with their DNTT layer deposited with either a moderate or a low deposition rate (0.03 nms^{-1} or 0.007 nms^{-1}) onto either one of the two SAMs on 10 nm thick Al_2O_3 layer as the gate dielectric.[*] **Table 6.6** represents the TFT parameters extracted from the transfer curves below.
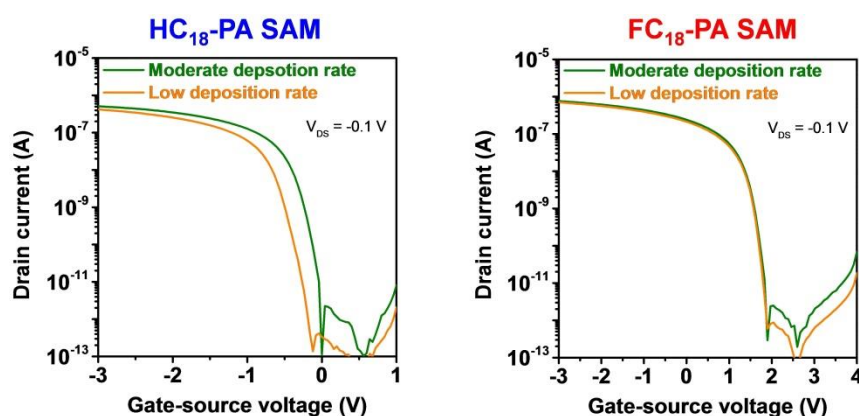
Figure 6.15: Transfer characteristics of DNTT TFTs (in the linear regime with $V_{DS} = -0.1$ V) fabricated using the HC_{18}-PA SAM or the FC_{18}-PA SAM with the DNTT layers deposited with either a moderate deposition rate of 0.03 nms^{-1} or a low deposition rate of 0.007 nms^{-1}.

Based on the morphology studies in Chapter 5 and the values obtained in the **Table 6.6**, we rule out that the different morphology of the DNTT films on HC_{18}-PA and FC_{18}-PA functionalized substrates is responsible for the observed difference in the threshold voltage of the TFTs.

Furthermore, the Al_2O_3 layer underneath the SAM is atomically smooth for all the thicknesses and thus is unlikely to induce changes in the DNTT film morphology within the series of TFTs treated with the FC_{18}-PA SAM, which might cause the observed thickness-dependent V_{th} shift. In other words, neither the fact that the threshold voltages of the TFTs based on the FC_{18}-PA SAM are significantly more positive than those of the TFTs with the HC_{18}-PA SAM, nor the observation that the threshold voltage increases

---

[*] Since the significant influence of the deposition rate on the thin-film morphology in multilayered DNTT films and partial surface DNTT coverage has already been shown and discussed in detailed in Chapter 5, here we focus on the transistor characteristics and in particular the influence of the DNTT deposition rate on the threshold voltage.

linearly with the inverse of the gate-dielectric capacitance in the case of the FC$_{18}$-PA SAM, but not in the case of the HC$_{18}$-PA SAM, can be explained with the different DNTT morphologies induced by the different surface energies of the two SAMs.

Deposition rate (nm/s)	Threshold voltage (V)	Field-effect mobility (cm^2/Vs)	Subthreshold swing (mV/decade)	On/ off current ratio
HC$_{18}$-PA SAM				
0.007	−0.6	2.2	99	10^6
0.03	−0.4	2.3	98	10^6
FC$_{18}$-PA SAM				
0.007	+1.2	2.1	121	10^6
0.03	+1.3	2.1	139	10^6

Table 6.6: The TFT parameters of DNTT TFTs (in the linear regime with V$_{DS}$ = −0.1 V) fabricated using the HC$_{18}$-PA SAM or the FC$_{18}$-PA SAM with the DNTT layers deposited with either a moderate deposition rate of 0.03 nms^{-1} or a low deposition rate of 0.007 nms^{-1}.

6.4.2 Electronic coupling between the SAM and the organic semiconductor

Having ruled out the DNTT morphology as a determinant factor in the relationship between the threshold voltage and the gate-dielectric capacitance, we turn to the question whether there are any electrostatic or electronic interactions between the SAM and the organic semiconductor that could play a role in determining the relationships between each particular SAM and the measured threshold voltages. Such possibility has been discussed in the context of charge transfer (*i.e.,* chemical doping),[176,192,193] charge trapping,[194] and electrostatic interactions between the organic semiconductor with the local electric field of the dipolar SAM.[123,171] The latter has been proposed recently by Mityashin *et al.* as the mechanism responsible for the observation of a more positive threshold voltage for pentacene TFTs with fluoroalkyl-silane SAMs (in comparison to alkyl-silane SAMs), and this effect has been attributed to the accumulation of positive charge carriers due to broadening and shift of the density of states in the pentacene/SAM interface.[123]

We showed in Section 6.3 that the electrostatic potential of the surface can be precisely measured by KPFM. In order to investigate the electrostatic interaction between DNTT and the SAMs, we require a well-defined interface between the two, at which the CPD can be measured by the KPFM. Our strategy to obtain such an interface is the growth of thin DNTT islands which leads to a partial surface coverage, similar to our approach in Chapter 4 (with the PTCDI-C$_8$/DIP system). This was achieved by the deposition of a nominally 2 nm thick layer of DNTT onto the HC$_{18}$-PA SAM and the FC$_{18}$-PA SAM.

Figure 6.16 shows AFM topography and KPFM electrostatic potential maps of a HC_{18}-PA SAM surface and of a FC_{18}-PA SAM surface, both decorated with individual and (mostly) unconnected islands of DNTT.
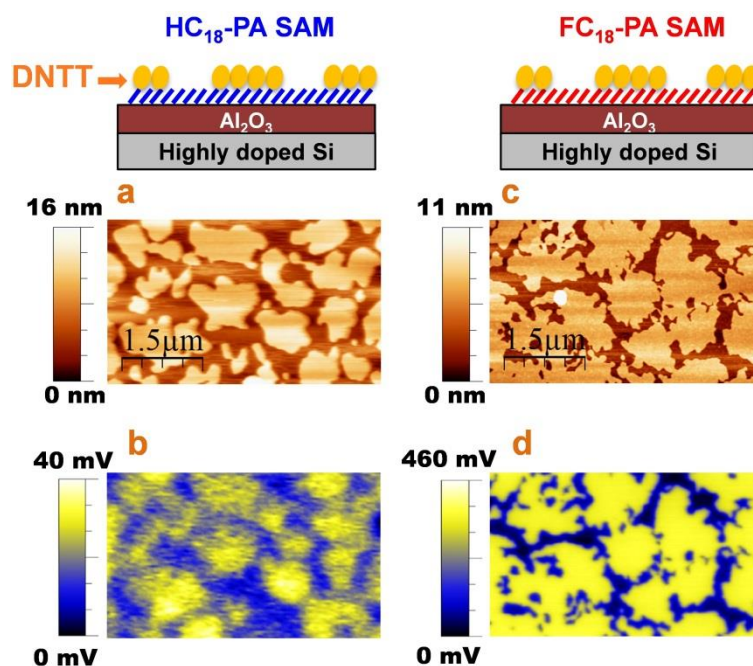
Figure 6.16: AFM topography images (first row) and KPFM electrostatic potential maps (second row) of the HC_{18}-PA SAM with partial DNTT coverage (a,b) and of the FC_{18}-PA SAM with partial DNTT coverage (c,d)

As can be seen in **Figure 6.16**-b, a small positive surface potential of about +40 mV is measured on the DNTT islands with respect to their surrounding HC_{18}-PA SAM. It has been reported that interfaces between organic semiconductors and dielectrics may exhibit interfacial electronic polarization due to interface dipoles.[195] We presume that the positive sign of the CPD observed on the DNTT islands on top of the HC_{18}-PA SAM is due to electronic polarization induced in the DNTT by the dipole moment of the HC_{18}-PA SAM.

The perpendicular components of the dipole moments of the HC_{18}-PA SAM and the FC_{18}-PA SAM point into opposite directions.[186] Therefore, if the surface potential on the DNTT located on the FC_{18}-PA SAM was also due to electronic polarization by the SAM dipole, the surface potential would be negative, *i.e.*, in the KPFM surface potential maps the DNTT islands would appear darker than the surrounding FC_{18}-PA SAM. However, as **Figure 6.16**-d clearly shows, there is a relatively large positive contact potential difference of about +0.4 V measured between the DNTT and the FC_{18}-PA SAM, which is an order of magnitude larger than that between the DNTT and the HC_{18}-PA SAM and is a value too large to have come from polarization effects by the intrinsic dipole of the SAM. This suggests that there is an interaction of some sort between the DNTT and the FC_{18}-PA

SAM that produces an interface dipole leading to a large positive surface potential on the DNTT islands.

As a cross-check experiment, we also prepared a substrate on which both SAMs are present, since a patterned substrate makes it possible to measure the electrostatic potentials on the two SAMs in a single uninterrupted measurement independent of the type and the condition of the probe tip. The potential map of the patterned surface (same substrate as the one shown in the **Figure 6.12**) partially covered by DNTT (**Figure 6.17**) clearly shows a relatively large contact potential difference between the DNTT islands and the FC_{18}-PA SAM in contrast to the small contact potential difference between the DNTT islands and the HC_{18}-PA SAM.
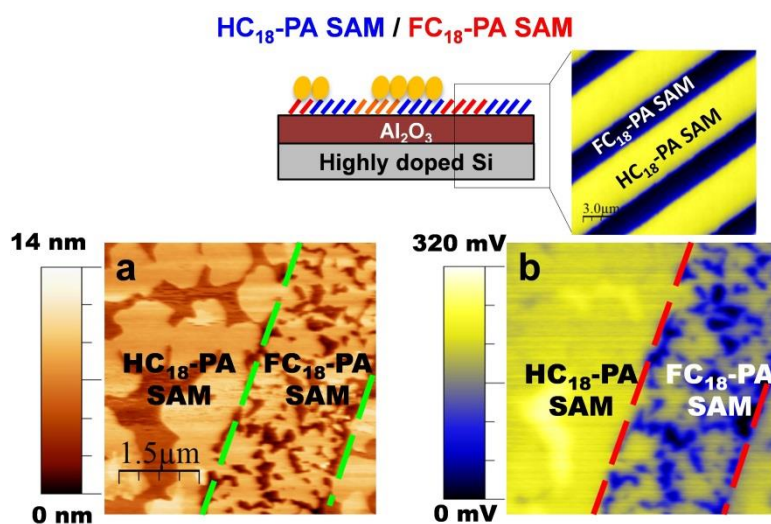
Figure 6.17: AFM topography image (a) and the KPFM map (b) of an array of both SAMs with partial DNTT coverage.

This observation confirms the presence of a certain electronic interaction between the DNTT and the FC_{18}-PA SAM, but not between the DNTT and the HC_{18}-PA SAM. It is *a priori* not clear, whether the interface dipole formed at the interface between the DNTT and the FC_{18}-PA SAM stems from a charge transfer or an electrostatic doping due to an electrostatic interaction between the DNTT and the FC_{18}-PA SAM, or both effects. The large energy level mismatch between the highest occupied molecular orbital (HOMO) of DNTT (-5.4 eV)[33] and the lowest unoccupied molecular orbital (LUMO) of the SAM (~ -0.2 eV for octadecyltrichlorosilane SAMs with the same chain length as our FC_{18}-PA SAM)[196] makes direct charge transfer between the DNTT and the SAM unlikely. The other possibility is electrostatic doping caused by a chemical reaction at the interface. According to a comprehensive review by Dhar *et al.*, the presence of different chemical species at the

interface can create different electronic states that might favor or hinder electrostatic doping at the interface.[197]

6.5 Identifying the nature and the location of the space-charge layer

The positive electrostatic potential on the DNTT islands on the FC$_{18}$-PA SAM measured by KPFM (**Figure 6.16**-d) implies the accumulation of positive charges in the DNTT layer. To determine, whether the positive charges in the DNTT that form the space-charge layer are mobile or immobile, we will compare the observed positive shift of the threshold voltage of the TFTs with the large positive electrostatic potential on the DNTT islands measured by KPFM. Assuming that the positive surface potential on the DNTT islands in **Figure 6.16**-d originates from immobile positive charges in the DNTT layer that are compensated by immobile negative charges at the FC$_{18}$-PA SAM/DNTT interface, a small capacitance-independent shift of the threshold voltage would be expected. Such a situation would be similar to the effect of V$_{SAM}$ in Equation 6.3 and is not consistent with the observed linear dependence of V$_{th}$ on the inverse of the dielectric capacitance. On the other hand, if there were uncompensated immobile positive charges present in the semiconductor, a more negative gate-source voltage would be required to accumulate mobile holes. This would imply a negative shift of V$_{th}$, which is contrary to what we obtained in our TFT devices; see **Figure 6.13**. Having ruled out the scenarios above, points to the accumulation of mobile holes in the DNTT layer that are balanced by fixed (immobile) negative charges elsewhere in the device, either within the bulk of the Al$_2$O$_3$ or at one of the two interfaces between the Al$_2$O$_3$, the SAM and the DNTT layer. In the following the location of this negatively-charged layer will be discussed.

The presence of a defect density within the bulk of the Al$_2$O$_3$ as the location of the negative space-charge layer can be easily excluded because of the following reason. Increasing the thickness of the Al$_2$O$_3$ (5 nm to 200 nm) should scale up the density of the defects in the oxide and thereby result in a non-constant charge density in the semiconductor. This would appear as a non-linear relation between the threshold voltage and inverse of the dielectric capacitance as opposed to the linear trend observed in **Figure 6.8** for the TFTs with the FC$_{18}$-PA SAM.

The presence of the layer of fixed negative charges at the interface between the Al$_2$O$_3$ and the FC$_{18}$-PA SAM is not a very likely scenario either. Although the SAM is sufficiently thin

for the charges to tunnel from the DNTT to the defects of the oxide,[179,198] we believe that charge trapping at the SAM/Al_2O_3 interface is unlikely, since the hydroxyl groups (known to act as trap states) that are initially present on the Al_2O_3 surface are eliminated by the phosphonic acid SAM treatment.

We therefore postulate that the fixed negative charges are localized in the FC_{18}-PA SAM in close proximity to the DNTT layer. The accumulation of mobile holes in the DNTT layer, which is the consequence of the presence of immobile negative charges (electrons or ions) in the fluorine substituents of the SAM molecules, resembles interface chemical doping.[197] **Figure 6.18** illustrates that the space-charge layer, which is most probably the dominant mechanism behind the threshold-voltage shifts observed in the TFTs with the FC_{18}-PA SAM, consists of mobile holes in the DNTT layer located at the interface between the DNTT and the fluorine substituents in the SAM. This positively-charged layer screens a negative space-charge layer localized in the fluorine substituents of the FC_{18}-PA SAM.
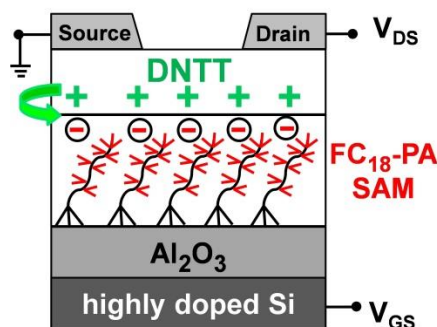
Figure 6.18: Schematic cross-section of the DNTT TFTs with the FC_{18}-PA SAM indicating the accumulation of mobile positive charges in the DNTT layer and immobile negative charges in the SAM at the interface between DNTT and the FC_{18}-PA SAM.

The density of the charges induced in the DNTT on top of the FC_{18}-PA SAM in the KPFM measurement (**Figure 6.16**-d) can be estimated by considering the DNTT islands as parallel-plate capacitors. The charge density in a capacitor can be obtained using $\sigma \approx C_{DNTT} \cdot V_{DNTT}$, where the capacitance of the DNTT islands is given by $C_{DNTT} = \varepsilon_{DNTT} \cdot \varepsilon_0 / d_{DNTT}$. The capacitance of the DNTT layer, C_{DNTT}, can be calculated assuming that $\varepsilon_{DNTT} = 4$ (same as for pentacene),[199] and $d_{DNTT} = 3.2$ nm (height of a double-layered island), resulting in a value of $C_{DNTT} \approx 0.11$ μFcm^{-2}, which together with $V_{DNTT} = 0.4$ V (from **Figure 6.16**-d) yields a value of $\sigma \approx 2.7 \times 10^{12}$ ecm^{-2} with a positive charge density σ^+ residing in the DNTT layer and a negative charge density σ^- in the FC_{18}-PA SAM. This value, which is comparable to the previously calculated charge density from the relationship between the threshold voltage and the inverse of the gate-dielectric capacitance

(3.5×10^{12} ecm^{-2} obtained from **Figure 6.13**), is a result of an electronic coupling between the FC$_{18}$-PA molecules and DNTT at their interface.

It is important to consider that the measured surface potential using KPFM stems from intrinsic electronic effects at the Al$_2$O$_3$/SAM/DNTT interfaces and does not include charge injection from the contacts to form the TFT channel, as is the case in a transistor. In fact, this could explain the slight difference between the two estimated charge densities from the KPFM and that obtained from the V$_{th}$ shifts in the TFTs ($\sigma \approx 2.7 \times 10^{12}$ ecm^{-2} *vs.* 3.5×10^{12} ecm^{-2}). Another scenario is the involvement of an additional mechanism such as trapping of immobile charges at the dielectric interface upon the operation of the TFTs as reported by Gholamrezaie *et al.*[194]

6.6 Chapter conclusions

To recapitulate this chapter; a systematic investigation was carried out to unravel the mechanisms behind the shift of the threshold voltage of bottom-gate organic TFTs by the functionalization of the surface of the Al_2O_3 gate dielectric with two different SAMs. It was demonstrated that in TFTs based on the FC_{18}-PA SAM, *i.e.,* a SAM with strongly electronegative fluorine substituents at the interface to the semiconductor, the threshold voltage exhibits a linear dependence on the inverse of the gate-dielectric capacitance ($V_{th} \propto 1/C_{diel}$), while in TFTs based on the HC_{18}-PA SAM, the threshold voltage is independent of the dielectric capacitance and is determined mainly by the electrostatic potential generated by the dipole moment of the SAM ($V_{th} \approx -V_{SAM}$).

To shed light on these dissimilar behaviors, a detailed nanoscale investigation of the electrostatic potential of the SAM/DNTT interface was carried out by means of KPFM. The obtained results provide evidence for an electronic coupling and therefore for the formation of a positive space-charge layer in the DNTT at its interface to the FC_{18}-PA SAM, which is responsible for the observed dependence of the threshold voltage on the gate-dielectric capacitance.

In contrast, no evidence for such interfacial electrostatic interaction was detected for the combination of DNTT and the HC_{18}-PA SAM. Thereby, the validity of the two intensely debated cases ($V_{th} \propto 1/C_{diel}$ and $V_{th} \approx -V_{SAM}$) was confirmed, showing that both of them are required to explain the threshold-voltage shift observed in organic TFTs due to SAMs at the semiconductor/dielectric interface.

113

7. Supplementary aspects of DNTT transistors

DNTT has received attention for its excellent air stability since the first report of its synthesis and use in TFTs in 2007.[33,200] DNTT has also been proven to be a very promising compound for the realization of large-area electronic devices on flexible substrates.[201–203]

In this chapter, we address the stability of DNTT TFTs over time by measuring the TFTs. The results are discussed in terms of the field-effect mobilities and the threshold voltages of the TFTs.

The second part of this chapter is devoted to the implementation of DNTT TFTs on flexible substrates. We have investigated the performance of DNTT TFTs based on two different flexible polymeric substrates, namely polyethylene naphthalate and benzocyclobutene.

7.1 Shelf life stability of DNTT TFTs

In this section, we will discuss the stability of the DNTT TFTs that were introduced in Section 5.5 over time. The TFTs were fabricated on Si substrates with a combination of SiO_2 and Al_2O_3 as the gate oxides (100 nm SiO_2 + 30 nm Al_2O_3), functionalized with 3 different phosphonic acid SAMs. Three devices will be compared, in which the gate dielectrics have been treated with phosphonic acid SAMs, namely a HC_{18}-PA SAM, a FC_{18}-PA SAM and a HC_{14}-PA SAM. In all three devices discussed in the following, the DNTT layer was deposited in the same deposition and with a moderate deposition rate of 0.03 nms^{-1}. The TFTs were measured three times: immediately after fabrication, one week after fabrication, and 18 months after fabrication. The samples were stored under ambient conditions outside the laboratory during this time.

Figure 7.1 shows the evolution of the transfer characteristics of transistors over time. The change of the transfer characteristics over time suggests a shift of the threshold voltage towards more positive values in all three cases. **Table 7.1** summarizes the TFT parameters from all the three devices.
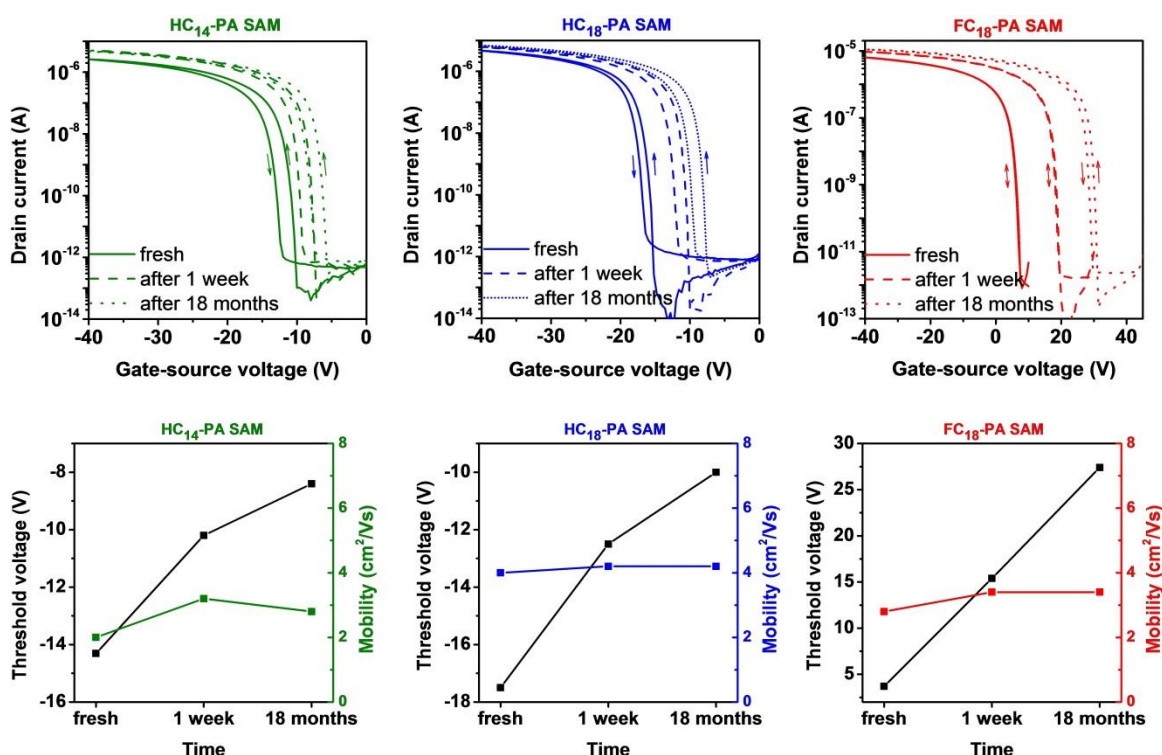
Figure 7.1: Transfer characteristics (in linear regime with V_{DS} = −1 V) of DNTT TFTs deposited onto Si/SiO_2/Al_2O_3 decorated with the HC_{14}-PA SAM, the HC_{18}-PA SAM and the FC_{18}-PA SAM measured fresh and after being exposed to air. The second row represents the threshold voltages and field-effect mobilities.

HC$_{14}$-PA SAM	fresh	after 1 week in air	after 18 months in air
μ (cm^2/Vs)	2	3.2	2.8
V_{th} (V)	-14.3	-10.2	-8.4
On/off current ratio	10^7	10^7	10^7
Subthreshold slope (mV/decade)	590	527	551

HC$_{18}$-PA SAM	fresh	after 1 week in air	after 18 months in air
μ (cm^2/Vs)	4	4.2	4.2
V_{th} (V)	-17.5	-12.5	-10
On/off current ratio	10^7	10^7	10^7
Subthreshold slope (mV/decade)	697	606	655

FC$_{18}$-PA SAM	fresh	after 1 week in air	after 18 months in air
μ (cm^2/Vs)	2.8	3.4	3.4
V_{th} (V)	3.7	15.4	27.4
On/off current ratio	10^7	10^7	10^7
Subthreshold slope (mV/decade)	801	1180	1764

Table 7.1: Summarized parameters from fresh and aged DNTT TFTs with the HC$_{14}$-PA SAM, HC$_{18}$-PA SAM and FC$_{18}$-PA SAM.

As can be seen in **Table 7.1**, in the TFTs with the HC$_{14}$-PA and the HC$_{18}$-PA SAM, the shift of the threshold voltages is rather significant during the first week of air exposure (4 V for the HC$_{14}$-PA SAM and 5 V for the HC$_{18}$-PA SAM) followed by a smaller shift of only 2 V during the following 18 months. The trend is quite different for the TFTs fabricated with the FC$_{18}$-PA SAM. The threshold voltage shifts by around 12 V during the first week of air exposure, followed by an equally large shift during the next 18 months.

However, an aspect that all TFTs have in common is that, independent of the type of the SAM, the threshold voltage always shifts towards more positive values without a linear correlation between the V_{th} shift and the time. The threshold-voltage shift towards more positive values is an indication for the accumulation of negative charges in the channel in all the devices, regardless of the type of the SAM. This suggests that the threshold voltage evolution with time does not originate from the SAM, but from DNTT.

Given the molecular structure of DNTT molecules, oxidation in air is not very likely to take place.[*] It has been reported that the positive threshold-voltage shifts in p-channel transistors could originate from the penetration of water molecules (from the humidity in

---

[*] FETs using pentacene are known to deteriorate in air. The central benzene ring in pentacene is prone to oxidation in an atmosphere. In DNTT, however, instead of the core benzene ring, two thiophene rings exist, which are less likely to react with oxygen. Besides, as a consequence of a lower-lying HOMO in DNTT compared to pentacene (-5.4 eV for DNTT *vs.* -5 eV for pentacene) the oxidation potential of DNTT molecules is larger and, therefore, DNTT is less likely to get oxidized.

the environment) into the grain boundaries of the semiconductor film, inducing the accumulation of mobile holes in the semiconductor, which leads to a more positive threshold voltage.[204,205] An alternative possibility is the occurrence of structural changes and an evolution of the thin-film morphology of DNTT, which will be investigated in the following.

The threshold-voltage shift can be seen more clearly in the graphs shown in the second row of **Figure 7.1**, which, in addition to the threshold-voltage shift, represent the evolution of the field-effect mobilities over time. The graphs showing the mobility over time demonstrate that aging in air does not have a significant effect on the field-effect mobilities in DNTT TFTs.

The influence of aging on the subthreshold slopes, however, appears to be different in the TFTs with the alkyl SAMs compared to the ones with the fluoroalkyl SAM, as shown in **Table 7.1**. The subthreshold slopes of the TFTs with the alkyl SAMs show a small reduction during the first week followed by rather small changes over the following 18 months of time compared to their initial values. In the TFTs with the FC_{18}-PA SAM, however, the subthreshold slope increases during the first week, and it reaches over twice its initial values after 18 months. An increased subthreshold slope could be an indication for trapping of charges at the dielectric interface in the TFTs with the FC_{18}-PA SAM. Therefore, charge trapping is, perhaps, the reason behind the larger threshold-voltage shift in the devices with the fluoroalkyl SAMs over time, compared to the devices with the alkyl SAMs. Also, it can be seen in **Table 7.1** that all devices, regardless of the type of the SAM, maintain a large on/off current ratio over 18 months.

In addition to the performance of the TFTs, the morphology of the DNTT layer used as the active material has been investigated using AFM topography images, as shown in **Figure 7.2**. As can be seen from the images, the morphology of the DNTT layer does not show a significant change over time. Although we have shown in Chapter 5 that the performance of DNTT TFTs is to a large degree independent of the morphology of the DNTT layer, the observation that the DNTT layer morphology does not degrade over several months is an additional evidence that supports the stability of vacuum-deposited DNTT layers.
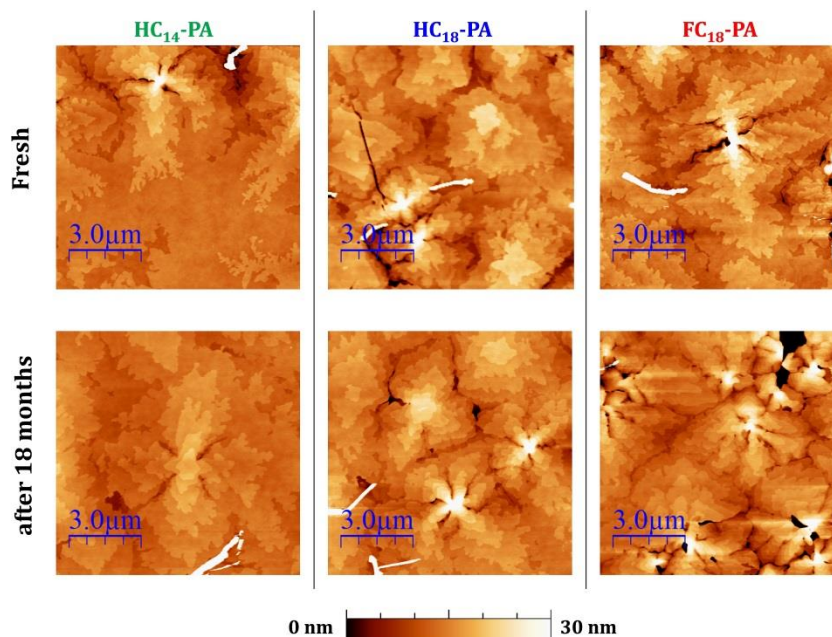
Figure 7.2: AFM topography images of DNTT thin films deposited onto $Si/SiO_2/Al_2O_3$ decorated with the HC_{14}-PA SAM, the HC_{18}-PA SAM and the FC_{18}-PA SAM measured fresh, after one week and after 18 months.

This observation and the fact that in all the cases the final mobilities are (or almost are) as large as their initial values in a fresh device, suggest that DNTT TFTs have a good air-stability. Our observations regarding the air-stability of DNTT TFTs are in agreement with the previous reports on the shelf-life stability of DNTT transistors.[200]

7.2 DNTT transistors on flexible substrates

The high performance of the TFTs with DNTT and its derivatives on flexible substrates has been reported previously in the literature.[201–203,206–208]

PEN has been frequently employed as a template for flexible DNTT TFTs. PEN is a polyester polymer and was used in this work in the form of a thin, flexible, bendable and rollable transparent film.

The second bendable film used in this work is another polymer called BCB. BCB polymer, which is known for its use in packaging and microelectronics, was spun onto a flat and smooth substrate (Si wafers) from the solution by spin-coating, leading to the formation of a smooth film. The advantage of BCB over PEN is the facile manufacturing process and the control over the film thickness. The BCB films can be easily removed from the rigid substrate base (Si) once the film is dry. The chemical structures of PEN and BCB are shown in **Figure 7.3**.
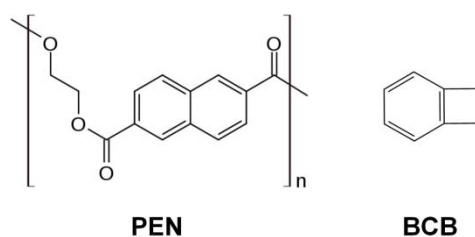
Figure 7.3: Chemical structure of PEN and BCB

The properties of PEN and BCB films can be studied in terms of surface roughness by AFM. **Figure 7.4** shows the topography images from the surface of a clean PEN film and a clean BCB film. According to this figure, PEN appears to have an overall smooth surface morphology with an exception of the sharp features with a height of several nanometers. The RMS roughness of PEN is around 3.9 nm, which is comparable to the recently-reported value in the literature.[209] The BCB surface, on the other hand, seems to consist of fiber-like structures which are distributed rather homogenously over the surface. The RMS roughness of the BCB film was measured to be around 3.1 nm, *i.e.* smaller than the PEN roughness, which might come as a surprise given the fiber structures on the BCB surface. However, unlike PEN, there are no high features present on the BCB surface.

Although high-performance DNTT TFTs have been successfully fabricated on PEN substrates, [180–182] this is the first time that BCB films are being used as a template for DNTT TFTs.
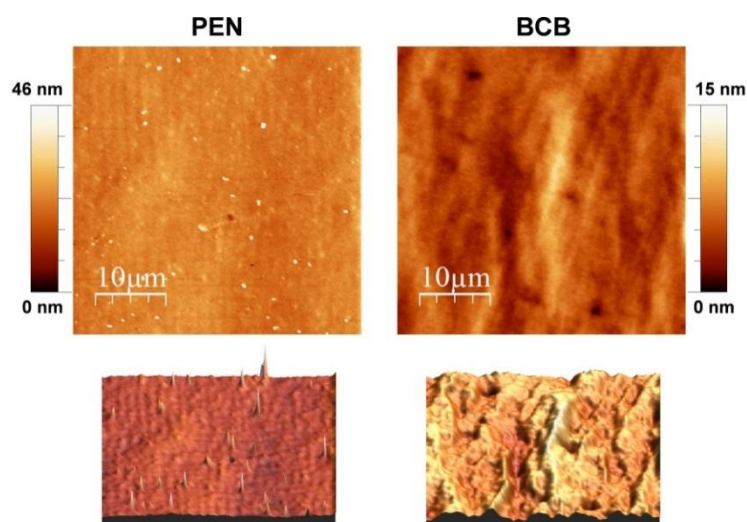
Figure 7.4: 2D and 3D AFM topography images of a PEN and a BCB film.

In the following the performance of DNTT TFTs on PEN and BCB substrates are presented and discussed. All the layers used in the fabrication of TFTs, including the gate metal (Al),

the gate dielectric, the DNTT and the source and drain contacts are patterned using high-resolution silicon stencil masks.[210] The gate metal is formed by patterning a 30 nm thick layer of Al by thermal evaporation in the vacuum system. The gate dielectric consists of a thin layer (~3.6 nm) of AlO_x formed by oxygen plasma and functionalized with the HC_{14}-PA SAM using the dip-coating method. A nominally 25 nm thick layer of DNTT was patterned by sublimation through a shadow mask followed by the deposition of Au source and drain contacts. **Figure 7.5** shows the implementation of DNTT TFTs on PEN and BCB flexible films along with the layout used for the fabrication of the TFTs.
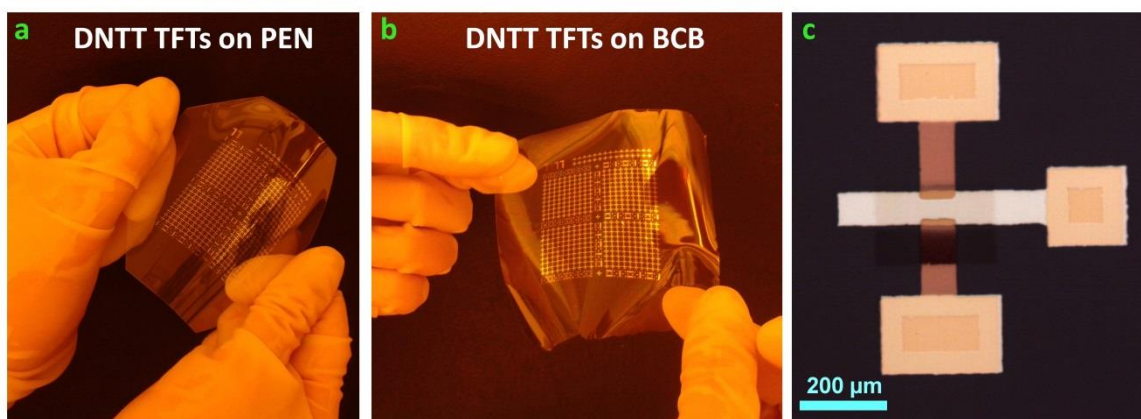
Figure 7.5: Photographs taken from fully-patterned DNTT TFTs on the two rollable and bendable substrates, (a) PEN and (b) BCB. (c) Optical micrograph of the layout of a DNTT TFT fabricated on BCB.

The output and transfer characteristics of the TFTs on PEN and BCB films are shown in **Figure 7.6** and **Table 7.2** summarizes the TFT parameters. As can be seen, both TFTs have a very small leakage current. The turn-on drain current is very similar in both TFTs (in the range of 10^{-6} A), however, the on/off current ratio is larger for the TFTs on PEN. The threshold voltage extracted from the transfer curves in the saturation regime on both substrates is -1.7 V. Nevertheless, the TFTs on the BCB substrate seem to have an overall better performance compared to the TFTs on the PEN substrate in terms of field effect mobility (1.3 cm²/Vs *vs.* 1 cm²/Vs) and (slightly) steeper subthreshold slopes (84 mV/decade *vs.* 91 mV/decade).
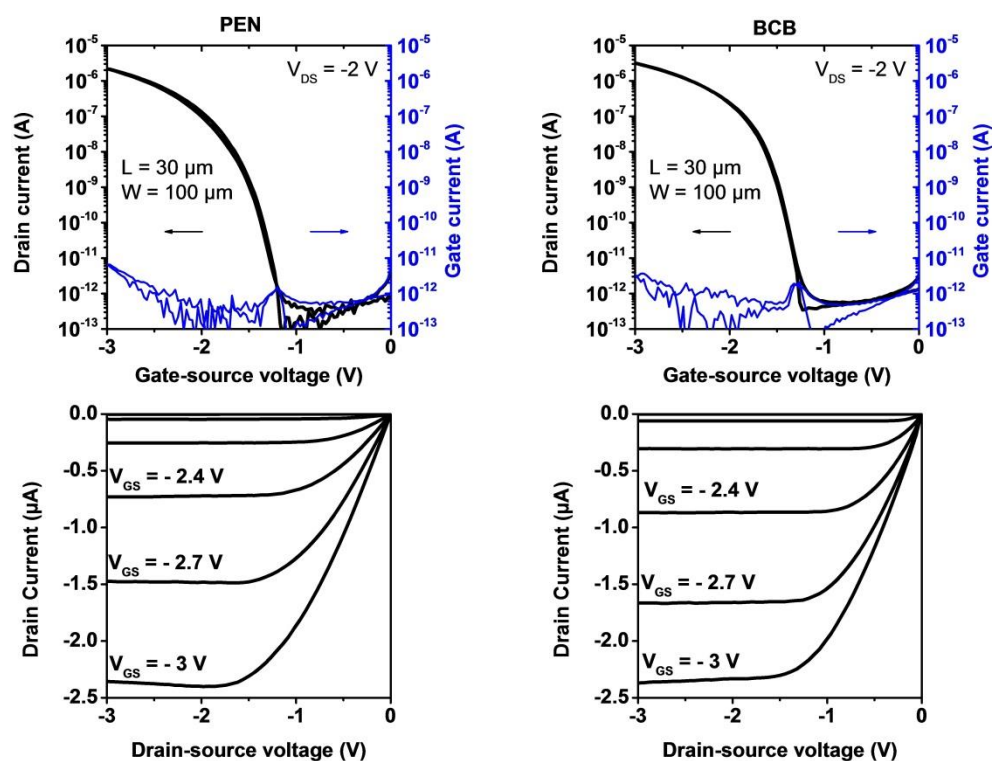
Figure 7.6: Transfer and output characteristics (in the saturation regime $V_{DS} = -2$ V) of DNTT TFTs fabricated on PEN and BCB substrates decorated with the HC_{14}-PA SAM.

Substrate	Threshold voltage (V)	Field-effect mobility (cm^2/Vs)	Subthreshold swing (mV/decade)	On/off current ratio
PEN	-1.7	1	91	10^8
BCB	-1.7	1.3	84	10^7

Table 7.2: The table represents the TFT parameters corresponding to the transfer curves.

Therefore, we have successfully fabricated high performance DNTT TFTs on BCB, a compound that was not used conventionally as a template for organic TFTs and shown that the performance of DNTT TFTs on BCB films is comparable to that of the TFTs on PEN in terms of field effect mobility, threshold voltage and subthreshold slope.

We conclude that the BCB film is the more favorable substrate over PEN due to an improved overall performance of the TFTs in addition to BCB's ease of processing and good control over the substrate thickness and geometries.

7.3   Chapter conclusions

The shelf-life stability of DNTT TFTs with three different phosphonic acid SAMs has been investigated over a period of 18 months. Our studies confirm the previously-reported good air-stability of DNTT TFTs by showing that no degradation of the field-effect mobility occurs upon exposing the samples to ambient air over a long period of time. We also showed that the thin-film morphology of DNTT does not go through structural changes over time.

The chapter was wrapped up by introducing a new state of the art flexible template for high-performance DNTT TFTs called BCB, which has never been used for this purpose before. The performance of DNTT TFTs on BCB films has been compared to that of DNTT TFTs fabricated on PEN (currently the most widely-used flexible substrate for organic electronic devices). We have demonstrated that BCB is a suitable substrate for DNTT transistors by showing that DNTT TFTs perform equally-well as (and even slightly better than) the TFTs on PEN substrates.

8. Summary and outlook

8.1 Summary

The experiments performed in the present thesis provide a fantastic opportunity to optimize the properties of the interfaces in organic electronic devices. In this thesis a series of investigations were conducted, in which the organic/organic interfaces involved in organic solar cells and organic thin-film transistors were systematically researched. Diverse scanning probe microscopy techniques played a vital role in these studies, as the morphology and the electronic phenomena at the interfaces can be monitored precisely down to the nanoscale using these techniques. The results are summarized in two sections presented in the following. Additionally, a brief outlook of the promising applications of the findings in this work is provided.

8.1.1 Organic solar cells: the decisive impact of molecular orientation in donor/acceptor systems on exciton dissociation

One of the main objectives of this thesis was successfully addressed by studying the role of the morphological aspects of the donor/acceptor (D/A) interface on the functionality of organic solar cells. The D/A system selected for this investigation consisted of two small molecules, namely DIP (as the electron donor) and PTCDI-C_8 (as the electron acceptor). Two different planar heterojunctions of DIP and PTCDI-C_8, a side-by-side heterojunction and a vertically-stacked heterojunction, were engineered and analyzed in terms of structure and optical properties. The optical phenomena occurring at these two planar interfaces were investigated using Kelvin probe force microscopy (KPFM) and photoluminescence (PL) measurements. PL measurements indicated the signature of a new transition, an emissive CT state, for the side-by-side horizontal configuration with DIP and PTCDI-C_8 molecules stacked with maximum π-orbital overlap next to each other at the interface. However, in the PL spectrum of the vertically-stacked heterojunction, where the donor and the acceptor molecules stand on top of each other, no trace of the emissive CT state was found. The second interesting finding is that the areal interface between DIP and PTCDI-C_8 in the heterojunctions has an impact on the intensity of the CT state emission that occurs at the interface.

These investigations demonstrated the impact of the relative molecular orientation of donor and the acceptor molecules at the D/A interface on the exciton dissociation and on

the energy-level alignment. Thereby, the importance of molecular design and control over the interface structure as a step towards the fabrication of photovoltaic devices with improved performances was demonstrated in this thesis.

8.1.2 Organic transistors: tunable threshold voltage and the mechanisms behind the threshold-voltage shift by SAMs

In the greater part of this thesis, the performance of TFTs with the benchmark organic semiconductor DNTT and the different phenomena associated with the passivation of the gate oxide of the DNTT TFTs with ultrathin dielectrics, known as self-assembled monolayer (SAMs) were investigated.

First, the three most common methods of treating the gate-oxide surface in the TFTs with the phosphonic acid SAMs, namely dip coating, microcontact printing and vacuum sublimation, were compared. This comparison allowed for the determination of dip coating as the most effective SAM treatment method.

Next, the impact of the DNTT morphology (used as the active layer in DNTT TFTs) on the performance of DNTT TFTs was systematically studied. The approach adopted in this part is through the manipulation of the deposition rate of the DNTT and, thereby, varying the morphology of the thin films of DNTT. This study resulted in the following finding: despite significant differences in the DNTT morphology (confirmed by atomic force microscopy (AFM)), all TFTs exhibited very similar carrier mobilities and threshold voltage values. This observation is strong evidence that the grain boundaries in polycrystalline DNTT films do not form high-resistivity barriers that limit the charge transport and performance of DNTT TFTs.

The DNTT TFTs were further investigated with the purpose of identifying the origin of the threshold-voltage shift phenomenon, as one of the most important consequences of the gate-oxide passivation with SAMs. This challenge was addressed by developing a model system, comprising DNTT TFTs with dielectrics consisting of five different aluminum oxide thicknesses (ranging from 5 nm to 200 nm) and two different SAMs, and exploring the dependence of the threshold voltage of the TFTs on the gate-dielectric capacitance. This strategy revealed that the dependence of the threshold voltage on the gate-dielectric capacitance is related to the type of the SAM: In the TFTs with the alkyl SAM, the threshold voltage is determined solely by the electrostatic potential of the SAM (created by the dipole moment of the SAM), whereas in the TFTs with the fluoroalkyl SAM the threshold voltage is inversely proportional to the gate-dielectric capacitance, which is evidence for

the formation of a space-charge layer. In other words, there exists a clear confirmation for two of the most intensely-debated scenarios in the literature, threshold-voltage shift by the dipole moment of the SAM/or by a space-charge layer, depending simply on the choice of SAM. KPFM studies established that the observed dependence of the threshold voltage on the gate-dielectric capacitance in the TFTs with the fluoroalkyl SAM can be attributed to an electrostatic interaction between the fluoroalkyl SAM and DNTT molecules. Therefore, it was demonstrated that the mechanisms, by which the gate-dielectric modification with a SAM affects the threshold voltage of organic TFTs, are ultimately related to specific properties of the SAM/semiconductor interface and can, therefore, not be ascribed solely to the dipole moment of the SAM, as reported frequently in the literature.

The thesis is wrapped up with the successful implementation of DNTT TFTs on a new state of the art flexible template, known as BCB, for high-performance organic TFTs. This finding is considered very important for potential commercial manufacturing of DNTT TFTs in flexible organic electronic devices.

8.2 Outlook

The idea behind the interface-engineering of DIP/PTCDI-C_8 as a model D/A system can be stretched to other D/A systems and tailoring the D/A interface into desired structures by taking advantage of engineered planar heterojunction architectures as an alternative to the bulk heterojunction concept.

The next promising perspective is related to the high-performance organic transistors with the desired operating voltages. The study of DNTT TFTs realized on phosphonic acid SAMs/aluminum oxide gate dielectrics can also be extended to other SAM/semiconductor systems. Additionally, by determining the electrostatic phenomena at the SAM/semiconductor interface using KPFM a new exciting path towards the design of improved logic circuits with the desired threshold voltage values opens, where selecting of the proper combination of oxide type, oxide thickness, SAM and the organic semiconductor can result in major advances for the commercialization of organic TFTs in high-end applications.

Together, in the versatile projects in this thesis the importance of the interfaces involved in organic D/A solar cells and organic TFTs are highlighted and novel strategies to open new routes towards interface engineering in organic electronic devices are developed.

Interface engineering in organic electronic devices could be the first and foremost step to achieve full realization of high performance devices and their commercialization in the market of electronic and energy devices.

Bibliography

(1)   Braun, S.; Salaneck, W. R.; Fahlman, M. Energy-Level Alignment at Organic/Metal and Organic/Organic Interfaces. *Adv. Mater.* **2009**, *21*, 1450–1472.

(2)   Clarke, T. M.; Durrant, J. R. Charge Photogeneration in Organic Solar Cells. *Chem. Rev.* **2010**, *110*, 6736–6767.

(3)   Horowitz, G. Interfaces in Organic Field-Effect Transistors. *Adv. Polym. Sci.* **2010**, *223*, 113–153.

(4)   Schwoerer, M.; Wolf, H. C. *Organic Molecular Solids*; 1st ed.; Wiley-VCH Verlag GmbH & Co. KGaA, 2007.

(5)   *Physics of Organic Semiconductors*; Brütting, W.; Adachi, C., Eds.; 2nd ed.; Wiley-VCH Verlag GmbH & Co. KGaA, 2012.

(6)   Chopra, N.; Lee, J.; Zheng, Y.; Eom, S. H.; Xue, J.; So, F. Effect of the Charge Balance on High-Efficiency Blue-Phosphorescent Organic Light-Emitting Diodes. *ACS Appl. Mater. Interfaces* **2009**, *1*, 1169–1172.

(7)   Klauk, H. Organic Thin-Film Transistors. *Chem. Soc. Rev.* **2010**, *39*, 2643.

(8)   Sze, S. M.; Ng, K. K. *Physics of Semiconductor Devices*; 3rd ed.; Wiley-Interscience, 2008.

(9)   Karl, N. Charge Carrier Transport in Organic Semiconductors. *Synth. Met.* **2003**, *133-134*, 649–657.

(10)   Bässler, H. Charge Transport in Disordered Organic Photoconductors a Monte Carlo Simulation Study. *Phys. Status Solidi B* **1993**, *175*, 15–56.

(11)   Le Comber, P. G.; Spear, W. E. Electronic Transport in Amorphous Silicon Films. *Phys. Rev. Lett.* **1970**, *25*, 509–511.

(12)   Horowitz, G.; Hajlaoui, R.; Delannoy, P. Temperature Dependence of the Field-Effect Mobility of Sexithiophene . Determination of the Density of Traps. *J. Phys. III* **1995**, *5*, 355–371.

(13)   Pope, M.; Swenberg, C. E. Electronic Processes in Organic Solids. *Annu. Rev. Phys. Chem.* **1984**, *35*, 613–655.

(14)   Kampen, T. U. *Low Molecular Weight Organic Semiconductors*; 1st ed.; Wiley-VCH Verlag GmbH & Co, 2010.

(15)   Schwoerer, M.; Wolf, H. C. *Organic Molecular Solids*; 1st ed.; Wiley-VCH Verlag GmbH & Co, 2007.

(16)   von Braun, J.; Manz, G. Patent: Verfahren Zur Herstellung von Kondensationsprodukten Des Fluoranthens. 595 024, 1934.

(17)   Heinemeyer, U.; Scholz, R.; Gisslén, L.; Alonso, M.; Ossó, J.; Garriga, M.; Hinderhofer, a.; Kytka, M.; Kowarik, S.; Gerlach, a.; *et al.* Exciton-Phonon Coupling in Diindenoperylene Thin Films. *Phys. Rev. B* **2008**, *78*, 085210.

(18)   Wilke, A.; Endres, J.; Hörmann, U.; Niederhausen, J.; Schlesinger, R.; Frisch, J.; Amsalem, P.; Wagner, J.; Gruber, M.; Opitz, A.; *et al.* Correlation between Interface Energetics and Open Circuit Voltage in Organic Photovoltaic Cells. *Appl. Phys. Lett.* **2012**, *101*, 233301.

(19)   Dürr, A. C.; Schreiber, F.; Münch, M.; Karl, N.; Krause, B.; Kruppa, V.; Dosch, H. High Structural Order in Thin Films of the Organic Semiconductor Diindenoperylene. *Appl. Phys. Lett.* **2002**, *81*, 2276.

(20)   Zhang, X. N.; Barrena, E.; de Oteyza, D. G.; Dosch, H. Transition from Layer-by-Layer to Rapid Roughening in the Growth of DIP on SiO$_2$. *Surf. Sci.* **2007**, *601*, 2420–2425.

(21)   Zhang, X.; Barrena, E.; Goswami, D.; de Oteyza, D.; Weis, C.; Dosch, H. Evidence for a Layer-Dependent Ehrlich-Schwöbel Barrier in Organic Thin Film Growth. *Phys. Rev. Lett.* **2009**, *103*, 136101.

(22)   Dürr, A.; Schreiber, F.; Ritley, K.; Kruppa, V.; Krug, J.; Dosch, H.; Struth, B. Rapid Roughening in Thin Film Growth of an Organic Semiconductor (Diindenoperylene). *Phys. Rev. Lett.* **2003**, *90*, 016104.

(23) Wagner, J.; Gruber, M.; Hinderhofer, A.; Wilke, A.; Bröker, B.; Frisch, J.; Amsalem, P.; Vollmer, A.; Opitz, A.; Koch, N.; *et al.* High Fill Factor and Open Circuit Voltage in Organic Photovoltaic Cells with Diindenoperylene as Donor Material. *Adv. Funct. Mater.* **2010**, *20*, 4295–4303.

(24) Mazhari, B.; Gangwar, A. Patent: Thin Film Transistor with a Current-Induced Channel, 2015.

(25) Jones, B. A.; Facchetti, A.; Wasielewski, M. R.; Marks, T. J. Tuning Orbital Energetics in Arylene Diimide Semiconductors. Materials Design for Ambient Stability of N-Type Charge Transport. *J. Am. Chem. Soc.* **2007**, *129*, 15259–15278.

(26) Krauss, T. N.; Barrena, E.; Zhang, X. N.; de Oteyza, D. G.; Major, J.; Dehm, V.; Würthner, F.; Cavalcanti, L. P.; Dosch, H. Three-Dimensional Molecular Packing of Thin Organic Films of PTCDI-C$_8$ Determined by Surface X-Ray Diffraction. *Langmuir* **2008**, *24*, 12742–12744.

(27) Krauss, T. N.; Barrena, E.; Oteyza, D. G. De; Zhang, X. N.; Dehm, V.; Wu, F.; Dosch, H. X-Ray / Atomic Force Microscopy Study of the Temperature-Dependent Multilayer Structure of PTCDI-C$_8$ Films on SiO$_2$. **2009**, 4502–4506.

(28) Malenfant, P. R. L.; Dimitrakopoulos, C. D.; Gelorme, J. D.; Kosbar, L. L.; Graham, T. O.; Curioni, A.; Andreoni, W. N-Type Organic Thin-Film Transistor with High Field-Effect Mobility Based on a N,N[sup ']-Dialkyl-3,4,9,10-Perylene Tetracarboxylic Diimide Derivative. *Appl. Phys. Lett.* **2002**, *80*, 2517.

(29) Chesterfield, R. J.; Mckeen, J. C.; Newman, C. R.; Ewbank, P. C.; Filho, S.; Bre, J.; Miller, L. L.; Mann, K. R.; Frisbie, C. D. Organic Thin Film Transistors Based on N-Alkyl Perylene Diimides : Charge Transport Kinetics as a Function of Gate Voltage and Temperature. *J. Phys. Chem. B* **2004**, *108*, 19281–19292.

(30) Weitz, R. T.; Amsharov, K.; Zschieschang, U.; Villas, E. B.; Goswami, D. K.; Burghard, M.; Dosch, H.; Jansen, M.; Kern, K.; Klauk, H. Organic N-Channel Transistors Based on Core-Cyanated Perylene Carboxylic Diimide Derivatives. *J. Am. Chem. Soc.* **2008**, *130*, 4637–4645.

(31) Rödel, R.; Letzkus, F.; Zaki, T.; Burghartz, J. N.; Kraft, U.; Zschieschang, U.; Kern, K.; Klauk, H. Contact Properties of High-Mobility, Air-Stable, Low-Voltage Organic N-Channel Thin-Film Transistors Based on a Naphthalene Tetracarboxylic Diimide. *Appl. Phys. Lett.* **2013**, *102*, 1–5.

(32) Rahimi, R.; Narang, V.; Korakakis, D. Optical and Morphological Studies of Thermally Evaporated PTCDI-C$_8$ Thin Films for Organic Solar Cell Applications. *Int. J. Photoenergy* **2013**, *2013*, 1–7.

(33) Yamamoto, T.; Takimiya, K. Facile Synthesis of Highly π-Extended Heteroarenes, Application to Field-Effect Transistors. *J. Am. Chem. Soc.* **2007**, *129*, 2224–2225.

(34) Sánchez-Carrera, R. S.; Atahan, S.; Schrier, J.; Aspuru-Guzik, A. Theoretical Characterization of the Air-Stable , High-Mobility Dinaphtho [2,3-b:2′3′-f]thieno[3,2-B]-Thiophene Organic Semiconductor. *J. Phys. Chem. C* **2010**, *114*, 2334–2340.

(35) Zschieschang, U.; Ante, F.; Schlörholz, M.; Schmidt, M.; Kern, K.; Klauk, H. Mixed Self-Assembled Monolayer Gate Dielectrics for Continuous Threshold Voltage Control in Organic Transistors and Circuits. *Adv. Mater.* **2010**, *22*, 4489–4493.

(36) Link   http://cleantechnica.com/2015/07/09/suntech-ramps-silicon-solar-cell-efficiency-beats-record/- (accessed Sep 11, 2015).

(37) Hübler, A.; Trnovec, B.; Zillger, T.; Ali, M.; Wetzold, N.; Mingebach, M.; Wagenpfahl, A.; Deibel, C.; Dyakonov, V. Printed Paper Photovoltaic Cells. *Adv. Energy Mater.* **2011**, *1*, 1018–1022.

(38) Würfel, P. *Physics of Solar Cells*; 2nd ed.; Wiley-VCH Verlag GmbH & Co. KGaA, 2009.

(39) Franck, J. Elementary Processes of Photochemical Reactions. *Trans. Faraday Soc.* **1924**, 536–542.

(40) Condon, E. A Theory of Intensity Distribution in Band Systems. *Phys. Rev.* **1926**, *28*, 1182–1201.

(41) Garcia Sole, J.; Bausa, L. E.; Jaque, D. *An Introduction to the Optical Spectroscopy of Inorganic Solids*; John Wiley & Sons Ltd, 2005.

(42) Markov, D.; Hummelen, J.; Blom, P.; Sieval, a. Dynamics of Exciton Diffusion in Poly(p-Phenylene

Vinylene)/fullerene Heterostructures. *Phys. Rev. B* **2005**, *72*, 1–5.

(43)   Markov, D.; Tanase, C.; Blom, P.; Wildeman, J. Simultaneous Enhancement of Charge Transport and Exciton Diffusion in Poly(p-Phenylene Vinylene) Derivatives. *Phys. Rev. B* **2005**, *72*, 1–6.

(44)   Halls, J. J. M.; Pichler, K.; Friend, R. H.; Moratti, S. C.; Holmes, A. B. Exciton Diffusion and Dissociation in a Poly(p-phenylenevinylene)/C60 Heterojunction Photovoltaic Cell. *Appl. Phys. Lett.* **1996**, *68*, 3120.

(45)   Tang, C. W. Two-Layer Organic Photovoltaic Cell. *Appl. Phys. Lett.* **1986**, *48*, 183.

(46)   Yu, G.; Gao, J.; Hummelen, J. C.; Wudl, F.; Heeger, A. J. Polymer Photovoltaic Cells: Enhanced Efficiencies via a Network of Internal Donor-Acceptor Heterojunctions. *Science* **1995**, *270*, 1789–1791.

(47)   Deibel, C.; Strobel, T.; Dyakonov, V. Role of the Charge Transfer State in Organic Donor-Acceptor Solar Cells. *Adv. Mater.* **2010**, *22*, 4097–4111.

(48)   Tvingstedt, K.; Vandewal, K.; Gadisa, A.; Zhang, F.; Manca, J.; Inganäs, O. Electroluminescence from Charge Transfer States in Polymer Solar Cells. *J. Am. Chem. Soc.* **2009**, *131*, 11819–11824.

(49)   Zhu, X.; Yang, Q.; Muntwiler, M.; Charge-, F. Charge-Transfer Excitons at Organic. **2009**, *42*, 1779–1787.

(50)   Sreearunothai, P.; Morteani, a.; Avilov, I.; Cornil, J.; Beljonne, D.; Friend, R.; Phillips, R.; Silva, C.; Herz, L. Influence of Copolymer Interface Orientation on the Optical Emission of Polymeric Semiconductor Heterojunctions. *Phys. Rev. Lett.* **2006**, *96*, 117403.

(51)   Brabec, C. J.; Heeney, M.; McCulloch, I.; Nelson, J. Influence of Blend Microstructure on Bulk Heterojunction Organic Photovoltaic Performance. *Chem. Soc. Rev.* **2011**, *40*, 1185–1199.

(52)   Horowitz, G. *Semicondcuting Polymers: Chemistry, Physics and Engineering*; Hadziioannou, G.; Van Hutten, P. F., Eds.; 1st ed.; Wiley-VCH Verlag GmbH, Weinheim, 1999.

(53)   *Organic Electronics Materials, Manufacturing and Applications*; Klauk, H., Ed.; 1st ed.; Wiley-VCH Verlag GmbH & Co, 2006.

(54)   Egginger, M.; Bauer, S.; Schwödiauer, R.; Neugebauer, H.; Sariciftci, N. S. Current versus Gate Voltage Hysteresis in Organic Field Effect Transistors. *Monatshefte für Chemie - Chem. Mon.* **2009**, *140*, 735–750.

(55)   Braga, D.; Horowitz, G. High-Performance Organic Field-Effect Transistors. *Adv. Mater.* **2009**, *21*, 1473–1486.

(56)   Meijer, E. J.; Tanase, C.; Blom, P. W. M.; van Veenendaal, E.; Huisman, B.-H.; de Leeuw, D. M.; Klapwijk, T. M. Switch-on Voltage in Disordered Organic Field-Effect Transistors. *Appl. Phys. Lett.* **2002**, *80*, 3838.

(57)   Horowitz, G. Organic Field-Effect Transistors. *Adv. Mater.* **1998**, *10*, 365–377.

(58)   Dimitrakopoulos, C. D.; Brown, A. R.; Pomp, A. Molecular Beam Deposited Thin Films of Pentacene for Organic Field Effect Transistor Applications. *J. Appl. Phys.* **1996**, *80*, 2501.

(59)   Gundlach, D. J.; Lin, Y. Y.; Jackson, T. N.; Nelson, S. F.; Schlom, D. G. Pentacene Organic Thin-Film Transistors-Molecular Ordering and Mobility. *IEEE Electron Device Lett.* **1997**, *18*, 87–89.

(60)   Kalb, W. L.; Batlogg, B. Calculating the Trap Density of States in Organic Field-Effect Transistors from Experiment: A Comparison of Different Methods. *Phys. Rev. B* **2010**, *81*, 1–13.

(61)   Klauk, H.; Schmid, G.; Radlik, W.; Weber, W.; Zhou, L.; Sheraw, C. D.; Nichols, J. A.; Jackson, T. N. Contact Resistance in Organic Thin Film Transistors. *Solid. State. Electron.* **2003**, *47*, 297–301.

(62)   Ante, F.; Kälblein, D.; Zschieschang, U.; Canzler, T. W.; Werner, A.; Takimiya, K.; Ikeda, M.; Sekitani, T.; Someya, T.; Klauk, H. Contact Doping and Ultrathin Gate Dielectrics for Nanoscale Organic Thin-Film Transistors. *Small* **2011**, *7*, 1186–1191.

(63)   Ante, F.; Kälblein, D.; Zaki, T.; Zschieschang, U.; Takimiya, K.; Ikeda, M.; Sekitani, T.; Someya, T.;

Burghartz, J. N.; Kern, K.; *et al.* Contact Resistance and Megahertz Operation of Aggressively Scaled Organic Transistors. *Small* **2012**, *8*, 73–79.

(64) Wong, H.-S.; White, M. H.; Krutsick, T. J.; Booth, R. V. Modeling of Transconductance Degradation and Extraction of Threshold Voltage in Thin Oxide MOSFET's. *Solid. State. Electron.* **1987**, *30*, 953–968.

(65) Ortiz-Conde, A.; Garcia Sánchez, F. J.; Liou, J. J.; Cerdeira, A.; Estrada, M.; Yue, Y. A Review of Recent MOSFET Threshold Voltage Extraction Methods. *Microelectron. Reliab.* **2002**, *42*, 583–596.

(66) Boudinet, D.; Le Blevennec, G.; Serbutoviez, C.; Verilhac, J.-M.; Yan, H.; Horowitz, G. Contact Resistance and Threshold Voltage Extraction in N-Channel Organic Thin Film Transistors on Plastic Substrates. *J. Appl. Phys.* **2009**, *105*, 084510.

(67) Robertson, J. High Dielectric Constant Oxides. *Eur. Phys. J. Appl. Phys.* **2004**, *29*, 265–291.

(68) Robertson, J. Intrinsic Defects and Hydroxyl Groups in a-SiO$_2$. *J. Phys. C Solid State Phys.* **1984**, *14*, L221–L225.

(69) Nguyen, P. T. T.; Rammelt, U.; Plieth, W.; Richter, S.; Plötner, M.; Fischer, W.-J.; Kiriy, N.; Kamloth, K. P.; Adler, H.-J. Experiments with Organic Field Effect Transistors Based on Polythiophene and Thiophene Oligomers. *Electrochim. Acta* **2005**, *50*, 1757–1763.

(70) Tatemichi, S.; Ichikawa, M.; Kato, S.; Koyama, T.; Taniguchi, Y. Low-Voltage, High-Gain, and High-Mobility Organic Complementary Inverters Based on N,N -Ditridecyl-3,4,9,10-Perylenetetracarboxylic Diimide and Pentacene. *Phys. Status Solidi - Rapid Res. Lett.* **2008**, *2*, 47–49.

(71) Chesterfield, R. J.; Newman, C. R.; Pappenfus, T. M.; Ewbank, P. C.; Haukaas, M. H.; Mann, K. R.; Miller, L. L.; Frisbie, C. D. High Electron Mobility and Ambipolar Transport in Organic Thin-Film Transistors Based on a π-Stacking Quinoidal Terthiophene. *Adv. Mater.* **2003**, *15*, 1278–1282.

(72) Chen, Y.; Shih, I.; Xiao, S. Effects of FeCl$_3$ Doping on Polymer-Based Thin Film Transistors. *J. Appl. Phys.* **2004**, *96*, 454.

(73) Hyodo, T.; Morita, F.; Naka, S.; Okada, H.; Onnagawa, H. Self-Aligned Organic Field-Effect Transistors Using Back-Surface Exposure Method. *Jpn. J. Appl. Phys.* **2004**, *43*, 2323–2325.

(74) Yamaguchi, J.; Yaginuma, S.; Haemori, M.; Itaka, K.; Koinuma, H. An in-Situ Fabrication and Characterization System Developed for High Performance Organic Semiconductor Devices. *Jpn. J. Appl. Phys.* **2005**, *44*, 3757–3759.

(75) Kim, K. D.; Song, C. K. Low Voltage Pentacene Thin Film Transistors Employing a Self-Grown Metal-Oxide as a Gate Dielectric. *Appl. Phys. Lett.* **2006**, *88*, 233508.

(76) Kang, H.; Han, K.; Park, J.-E.; Lee, H. H. High Mobility, Low Voltage Polymer Transistor. *Org. Electron.* **2007**, *8*, 460–464.

(77) Kim, J. B.; Fuentes-Hernandez, C.; Kim, S. J.; Potscavage, W. J.; Choi, S.; Kippelen, B. Ambipolar Thin-Film Transistors with a Co-Planar Channel Geometry. *Org. Electron.* **2010**, *11*, 1351–1356.

(78) Zakhidov, A. A.; Lee, J.-K.; DeFranco, J. A.; Fong, H. H.; Taylor, P. G.; Chatzichristidi, M.; Ober, C. K.; Malliaras, G. G. Orthogonal Processing: A New Strategy for Organic Electronics. *Chem. Sci.* **2011**, *2*, 1178.

(79) Bartic, C.; Jansen, H.; Campitelli, A.; Borghs, S. Ta$_2$O$_5$ as Gate Dielectric Material for Low-Voltage Organic Thin-Film Transistors. *Org. Electron.* **2002**, *3*, 65–72.

(80) Bartic, C.; Campitelli, a.; Borghs, S. Field-Effect Detection of Chemical Species with Hybrid Organic/inorganic Transistors. *Appl. Phys. Lett.* **2003**, *82*, 475–477.

(81) Fujisaki, Y.; Inoue, Y.; Kurita, T.; Tokito, S.; Fujikake, H.; Kikuchi, H. Improvement of Characteristics of Organic Thin-Film Transistor with Anodized Gate Insulator by an Electrolyte Solution and Low-Voltage Driving of Liquid Crystal by Organic Thin-Film Transistors. *Jpn. J. Appl. Phys.* **2004**, *43*, 372–377.

(82) Goettling, S.; Diehm, B.; Fruehauf, N. Active Matrix OTFT Display with Anodized Gate Dielectric. *J. Disp.*

Technol. **2008**, *4*, 300–303.

(83)   Hu, Y.; Dong, G.; Liu, C.; Wang, L.; Qiu, Y. Dependency of Organic Phototransistor Properties on the Dielectric Layers. *Appl. Phys. Lett.* **2006**, *89*, 7–9.

(84)   Qi, W.-J.; Nieh, R.; Lee, B. H.; Onishi, K.; Kang, L.; Jeon, Y.; Lee, J. C.; V.; Kaushik; Neuyen, B.-Y.; *et al.* Performance of MOSFETs with Ultra Thin ZrO2 and Zr Silicate Gate Dielectrics. *IEEE VLSl Technol. Dig. Tech. Pap.* **2000**.

(85)   Perkins, C. M.; Triplett, B. B.; McIntyre, P. C.; Saraswat, K. C.; Haukka, S.; Tuominen, M. Electrical and Materials Properties of ZrO2 Gate Dielectrics Grown by Atomic Layer Chemical Vapor Deposition. *Appl. Phys. Lett.* **2001**, *78*, 2357–2359.

(86)   Majewski, L. A.; Schroeder, R.; Grell, M. Low-Voltage, High-Performance Organic Field-Effect Transistors with an Ultra-Thin TiO2 Layer as Gate Insulator. *Adv. Funct. Mater.* **2005**, *15*, 1017–1022.

(87)   Sung, S.; Park, S.; Lee, W.-J.; Son, J.; Kim, C.-H.; Kim, Y.; Noh, D. Y.; Yoon, M.-H. Low-Voltage Flexible Organic Electronics Based on High-Performance Sol-Gel Titanium Dioxide Dielectric. *ACS Appl. Mater. Interfaces* **2015**, *7*, 7456–7461.

(88)   Ulman, A. *An Introduction to Ultrathin Organic Films from Langmuir- Blodgett to Self-Assembly*; Academic Press, 1991.

(89)   Collet, J.; Vuillaume, D. Nano-Field Effect Transistor with an Organic Self-Assembled Monolayer as Gate Insulator. *Appl. Phys. Lett.* **1998**, *73*, 2681–2683.

(90)   Lin, Y.; Gundlach, D. J.; Nelson, S. F.; Jackson, T. N. Stacked Pentacene Layer Organic Thin-Film Transistors with Improved Characteristics. *IEEE Electron Device Lett.* **1997**, *18*, 606–608.

(91)   Chua, L.; Zaumseil, J.; Chang, J.; Ou, E. C. General Observation of N-Type Field-Effect Behaviour in Organic Semiconductors. *Nature* **2005**, *434*, 194–199.

(92)   Tulevski, G. S.; Miao, Q.; Fukuto, M.; Abram, R.; Ocko, B.; Pindak, R.; Steigerwald, M. L.; Kagan, C. R.; Nuckolls, C. Attaching Organic Semiconductors to Gate Oxides: In Situ Assembly of Monolayer Field Effect Transistors. *J. Am. Chem. Soc.* **2004**, *126*, 15048–15050.

(93)   Mottaghi, M.; Lang, P.; Rodriguez, F.; Rumyantseva, A.; Yassar, A.; Horowitz, G.; Lenfant, S.; Tondelier, D.; Vuillaume, D. Low-Operating-Voltage Organic Transistors Made of Bifunctional Self-Assembled Monolayers. *Adv. Funct. Mater.* **2007**, *17*, 597–604.

(94)   Hutchins, D. O.; Weidner, T.; Baio, J.; Polishak, B.; Acton, O.; Cernetic, N.; Jen, A. K. Morphology and Thin Film Transistor Device Performance. *J. Mater. Chem. C* **2013**, *1*, 101–113.

(95)   Lin, Y.; Gundlach, D. J.; Nelson, S. F.; Jackson, T. N. Pentacene-Based Organic Thin-Film Transistors. *IEEE Trans. Electron Devices* **1997**, *44*, 1325–1331.

(96)   Gundlach, D. J.; Kuo, C.-C. S.; Sheraw, C. D.; Nichols, J. a.; Jackson, T. N. Improved Organic Thin Film Transistor Performance Using Chemically-Modified Gate Dielectrics. *SPIE* **2001**, *4466*, 54–64.

(97)   Hardigree, J. F. M.; Dawidczyk, T. J.; Ireland, R. M.; Johns, G. L.; Jung, B.; Nyman, M.; Ronald, O.; Markovic, N.; Katz, H. E. Reducing Leakage Currents in N-Channel Organic Field-Effect Transistors Using Molecular Dipole Monolayers on Nanoscale Oxides. *ACS Appl. Mater. Interfaces* **2013**, *5*, 7025–7032.

(98)   Kelley, T. W.; Boardman, L. D.; Dunbar, T. D.; Muyres, D. V.; Pellerite, M. J.; Smith, T. P. High-Performance OTFTs Using Surface-Modified Alumina Dielectrics. *J. Phys. Chem. B* **2003**, *107*, 5877–5881.

(99)   Majewski, L. a.; Grell, M.; Ogier, S. D.; Veres, J. A Novel Gate Insulator for Flexible Electronics. *Org. Electron.* **2003**, *4*, 27–32.

(100)   Majewski, L. A.; Schroeder, R.; Grell, M.; Glarvey, P. A.; Turner, M. L. High Capacitance Organic Field-Effect Transistors with Modified Gate Insulator Surface. *J. Appl. Phys.* **2004**, *96*, 5781–5787.

(101)   Hofmockel, R.; Zschieschang, U.; Kraft, U.; Rödel, R.; Hansen, N. H.; Stolte, M.; Würthner, F.; Takimiya,

K.; Kern, K.; Pflaum, J.; *et al.* High-Mobility Organic Thin-Film Transistors Based on a Small-Molecule Semiconductor Deposited in Vacuum and by Solution Shearing. *Org. Electron.* **2013**, *14*, 3213–3221.

(102) Yoon, W.-J.; Berger, P. R. Atomic Layer Deposited HfO2 Gate Dielectrics for Low-Voltage Operating, High-Performance Poly-(3-Hexythiophene) Organic Thin-Film Transistors. *Org. Electron.* **2010**, *11*, 1719–1722.

(103) Acton, O.; Acton, B. O.; Ting, G. G.; Shamberger, P. J.; Ohuchi, F. S.; Ma, H.; Jen, A. K.-Y. Dielectric Surface-Controlled Low-Voltage Organic Transistors via N-Alkyl Phosphonic Acid Self-Assembled Monolayers on High-K Metal Oxide. *ACS Appl. Mater. Interfaces* **2010**, *2*, 511–520.

(104) Acton, O.; Dubey, M.; Weidner, T.; O'Malley, K. M.; Kim, T.-W.; Ting, G. G.; Hutchins, D.; Baio, J. E.; Lovejoy, T. C.; Gage, A. H.; *et al.* Simultaneous Modification of Bottom-Contact Electrode and Dielectric Surfaces for Organic Thin-Film Transistors Through Single-Component Spin-Cast Monolayers. *Adv. Funct. Mater.* **2011**, *21*, 1476–1488.

(105) Cernetic, N.; Acton, O.; Weidner, T.; Hutchins, D. O.; Baio, J. E.; Ma, H.; Jen, A. K.-Y. Bottom-Contact Small-Molecule N-Type Organic Field Effect Transistors Achieved via Simultaneous Modification of Electrode and Dielectric Surfaces. *Org. Electron.* **2012**, *13*, 3226–3233.

(106) Wei, Q.; You, E.; Hendricks, N. R.; Briseno, A. L.; Watkins, J. J. Flexible Low-Voltage Polymer Thin-Film Transistors Using Supercritical CO2-Deposited ZrO2 Dielectrics. *ACS Appl. Mater. Interfaces* **2012**, *4*, 2322–2324.

(107) Park, Y. M.; Desai, A.; Salleo, A.; Jimison, L. Solution-Processable Zirconium Oxide Gate Dielectrics for Flexible Organic Field Effect Transistors Operated at Low Voltages. *Chem. Mater.* **2013**, *25*, 2571–2579.

(108) Beaulieu, M. R.; Baral, J. K.; Hendricks, N. R.; Tang, Y.; Briseño, A. L.; Watkins, J. J. Solution Processable High Dielectric Constant Nanocomposites Based on ZrO2 Nanoparticles for Flexible Organic Transistors. *ACS Appl. Mater. Interfaces* **2013**, *5*, 13096–13103.

(109) Xia, G.; Wang, S.; Zhao, X.; Zhou, L. High-Performance Low-Voltage Organic Transistor Memories with Room-Temperature Solution-Processed Hybrid Nanolayer Dielectrics. *J. Mater. Chem. C* **2013**, *1*, 3291.

(110) Lee, W.-H.; Wang, C.-C.; Chen, W.-T.; Ho, J.-C. Characteristic of Organic Thin Film Transistor with a High-K Insulator of Nano-TiO2 and Polyimide Blend. *Jpn. J. Appl. Phys.* **2008**, *47*, 8955–8960.

(111) Tang, M. L.; Okamoto, T.; Bao, Z. High-Performance Organic Semiconductors: Asymmetric Linear Acenes Containing Sulphur. *J. Am. Chem. Soc.* **2006**, *128*, 16002–16003.

(112) Bram, C.; Jung, C.; Stratmann, M. Self Assembled Molecular Monolayers on Oxidized Inhomogeneous Aluminum Surfaces. *Fresenius J. Anal. Chem.* **1997**, *358*, 108–111.

(113) Ma, H.; Acton, O.; Hutchins, D. O.; Cernetic, N.; Jen, A. K.-Y. Multifunctional Phosphonic Acid Self-Assembled Monolayers on Metal Oxides as Dielectrics, Interface Modification Layers and Semiconductors for Low-Voltage High-Performance Organic Field-Effect Transistors. *Phys. Chem. Chem. Phys.* **2012**, *14*, 14110–14126.

(114) Halik, M.; Hirsch, A. The Potential of Molecular Self-Assembled Monolayers in Organic Electronic Devices. *Adv. Mater.* **2011**, *23*, 2689–2695.

(115) DiBenedetto, S. A.; Facchetti, A.; Ratner, M. a.; Marks, T. J. Molecular Self-Assembled Monolayers and Multilayers for Organic and Unconventional Inorganic Thin-Film Transistor Applications. *Adv. Mater.* **2009**, *21*, 1407–1433.

(116) Gomes, H. L.; Stallinga, P.; Dinelll, F.; Murgia, M.; Biscarini, F.; De Leeuw, D. M.; Muck, T.; Geurts, J.; Molenkamp, L. W.; Wagner, V. Bias-Induced Threshold Voltages Shifts in Thin-Film Organic Transistors. *Appl. Phys. Lett.* **2004**, *84*, 3184–3186.

(117) Alam, M. A.; Dodabalapur, A.; Pinto, M. R. A Two-Dimensional Simulation of Organic Transistors. *IEEE Trans. Electron Devices* **1997**, *44*, 1332–1337.

(118) Li, T.; Balk, J. W.; Ruden, P. P.; Campbell, I. H.; Smith, D. L. Channel Formation in Organic Field-Effect Transistors. *J. Appl. Phys.* **2002**, *91*, 4312.

(119)   Mottaghi, M.; Horowitz, G. Field-Induced Mobility Degradation in Pentacene Thin-Film Transistors. *Org. Electron.* **2006**, *7*, 528–536.

(120)   de Oteyza, D. G.; Barrena, E.; Sellner, S.; Ossó, J. O.; Dosch, H. Structural Rearrangements during the Initial Growth Stages of Organic Thin Films of $F_{16}CuPc$ on SiO_2. *J. Phys. Chem. B* **2006**, *110*, 16618–16623.

(121)   Yang, S. Y.; Shin, K.; Park, C. E. The Effect of Gate-Dielectric Surface Energy on Pentacene Morphology and Organic Field-Effect Transistor Characteristics. *Adv. Funct. Mater.* **2005**, *15*, 1806–1814.

(122)   Chung, Y.; Verploegen, E.; Vailionis, A.; Sun, Y.; Nishi, Y.; Murmann, B.; Bao, Z. Controlling Electric Dipoles in Nanodielectrics and Its Applications for Enabling Air-Stable N-Channel Organic Transistors. *Nano Lett.* **2011**, *11*, 1161–1165.

(123)   Mityashin, A.; Roscioni, O. M.; Muccioli, L.; Zannoni, C.; Geskin, V.; Janssen, D.; Steudel, S.; Genoe, J.; Heremans, P. Multiscale Modeling of the Electrostatic Impact of Self-Assembled Monolayers Used as Gate Dielectric Treatment in Organic Thin-Film Transistors. *ACS Appl. Mater. Interfaces* **2014**, *6*, 15372–15378.

(124)   Goetting, L. B.; Deng, T.; Whitesides, G. M. Microcontact Printing of Alkanephosphonic Acids on Aluminum : Pattern Transfer by Wet Chemical Etching. *Langmuir* **1999**, *15*, 1182–1191.

(125)   Zschieschang, U.; Halik, M.; Klauk, H. Microcontact-Printed Self-Assembled Monolayers as Ultrathin Gate Dielectrics in Organic Thin-Film Transistors and Complementary Circuits. *Langmuir* **2008**, *24*, 1665–1669.

(126)   Hirata, I.; Zschieschang, U.; Ante, F.; Yokota, T.; Kuribara, K.; Yamamoto, T.; Takimiya, K.; Ikeda, M.; Kuwabara, H.; Klauk, H.; *et al.* Spatial Control of the Threshold Voltage of Low-Voltage Organic Transistors by Microcontact Printing of Alkyl- and Fluoroalkyl-Phosphonic Acids. *MRS Commun.* **2011**, *1*, 33–36.

(127)   Gupta, S.; Gleskova, H. Dry Growth of N-Octylphosphonic Acid Monolayer for Low-Voltage Organic Thin-Film Transistors. *Org. Electron.* **2013**, *14*, 354–361.

(128)   Kelvin, Lord. V. *Contact Electricity of Metals. Philos. Mag. Ser. 5* **1898**, *46*, 82–120.

(129)   Glatzel, T.; Lux-Steiner, M. C.; Strassburg, E.; Boag, A.; Rosenwaks, A. Y. Principles of Kelvin Probe Force Microscopy. In *Scanning Probe Microscopy*; Kalinin, S. V.; Gruverman, A., Eds.; 2007; pp. 113–131.

(130)   Liscio, A.; Palermo, V.; Mullen, K.; Samori, P. Tip-Sample Interactions in Kelvin Probe Force Microscopy: Quantitative Measurement of the Local Surface Potential. *J. Phys. Chem. C* **2008**, *112*, 17368–17377.

(131)   Palermo, V.; Palma, M.; Samorì, P. Electronic Characterization of Organic Thin Films by Kelvin Probe Force Microscopy. *Adv. Mater.* **2006**, *18*, 145–164.

(132)   De Boer, B.; Hadipour, A.; Mandoc, M. M.; Van Woudenbergh, T.; Blom, P. W. M. Tuning of Metal Work Functions with Self-Assembled Monolayers. *Adv. Mater.* **2005**, *17*, 621–625.

(133)   Puntambekar, K. P.; Pesavento, P. V.; Frisbie, C. D. Surface Potential Profiling and Contact Resistance Measurements on Operating Pentacene Thin-Film Transistors by Kelvin Probe Force Microscopy. *Appl. Phys. Lett.* **2003**, *83*, 5539–5541.

(134)   Horcas, I.; Fernández, R.; Gómez-Rodríguez, J. M.; Colchero, J.; Gómez-Herrero, J.; Baro, a M. WSXM: A Software for Scanning Probe Microscopy and a Tool for Nanotechnology. *Rev. Sci. Instrum.* **2007**, *78*, 013705.

(135)   Hill, J. P. Ultraviolet Photoelectron Spectroscopy. In *Characterization of Materials*; Wiley, 2002.

(136)   Last, J. A.; Ward, M. D. Electrochemical Annealing and Friction Anisotropy of Domains in Epitaxial Molecular Films. *Adv. Mater.* **1994**, *8*, 730–733.

(137)   Liley, M.; Gourdon, D.; Stamou, D.; Meseth, U.; Fischer, T. M.; Lautz, C.; Stahlberg, H.; Vogel, H.;

Burnham, N. A.; Duschl, C. Friction Anisotropy and Asymmetry of a Compliant Monolayer Induced by a Small Molecular Tilt. *Science (80-.).* **1998**, *280*, 273–275.

(138) Carpick, R. W.; Sasaki, D. Y.; Burns, A. R. Large Friction Anisotropy of a Polydiacetylene Monolayer. *Tribol. Lett.* **1999**, *7*, 79–85.

(139) Puntambekar, K.; Dong, J.; Haugstad, G.; Frisbie, C. D. Structural and Electrostatic Complexity at a Pentacene/Insulator Interface. *Adv. Funct. Mater.* **2006**, *16*, 879–884.

(140) Kalihari, V.; Tadmor, E. B.; Haugstad, G.; Frisbie, C. D. Grain Orientation Mapping of Polycrystalline Organic Semiconductor Films by Transverse Shear Microscopy. *Adv. Mater.* **2008**, *20*, 4033–4039.

(141) Zhong, J. Q.; Mao, H. Y.; Wang, R.; Qi, D. C.; Cao, L.; Wang, Y. Z.; Chen, W. Effect of Gap States on the Orientation-Dependent Energy Level Alignment at the DIP/F$_{16}$CuPc Donor–Acceptor Heterojunction Interfaces. *J. Phys. Chem. C* **2011**, *115*, 23922–23928.

(142) Hiroshiba, N.; Hayakawa, R.; Chikyow, T.; Yamashita, Y.; Yoshikawa, H.; Kobayashi, K.; Morimoto, K.; Matsuishi, K.; Wakayama, Y. Energy-Level Alignments and Photo-Induced Carrier Processes at the Heteromolecular Interface of Quaterrylene and N,N'-Dioctyl-3,4,9,10-Perylenedicarboximide. *Phys. Chem. Chem. Phys.* **2011**, *13*, 6280–6285.

(143) Kalinin, S. V.; Bonnell, D. A. Screening Phenomena on Oxide Surfaces and Its Implications for Local Electrostatic and Transport Measurements. *Nano Lett.* **2004**, *4*, 555–560.

(144) Hallermann, M.; Da Como, E.; Feldmann, J.; Izquierdo, M.; Filippone, S.; Martin, N.; Jüchter, S.; von Hauff, E. Correlation between Charge Transfer Exciton Recombination and Photocurrent in Polymer/fullerene Solar Cells. *Appl. Phys. Lett.* **2010**, *97*, 023301.

(145) Tvingstedt, K.; Vandewal, K.; Zhang, F.; Ingana, O. On the Dissociation Efficiency of Charge Transfer Excitons and Frenkel Excitons in Organic Solar Cells : A Luminescence Quenching Study. *J. Phys. Chem. C* **2010**, *114*, 21824–21832.

(146) Hallermann, M.; Kriegel, I.; Da Como, E.; Berger, J. M.; von Hauff, E.; Feldmann, J. Charge Transfer Excitons in Polymer/Fullerene Blends: The Role of Morphology and Polymer Chain Conformation. *Adv. Funct. Mater.* **2009**, *19*, 3662–3668.

(147) Clark, J.; Archer, R.; Redding, T.; Foden, C.; Tant, J.; Geerts, Y.; Friend, R. H.; Silva, C. Charge Recombination in Distributed Heterostructures of Semiconductor Discotic and Polymeric Materials. *J. Appl. Phys.* **2008**, *103*, 124510.

(148) Benson-Smith, J. J.; Goris, L.; Vandewal, K.; Haenen, K.; Manca, J. V.; Vanderzande, D.; Bradley, D. D. C.; Nelson, J. Formation of a Ground-State Charge-Transfer Complex in Polyfluorene/[6,6]-Phenyl-C61 Butyric Acid Methyl Ester (PCBM) Blend Films and Its Role in the Function of Polymer/PCBM Solar Cells. *Adv. Funct. Mater.* **2007**, *17*, 451–457.

(149) Ruani, G.; Fontanini, C.; Murgia, M.; Taliani, C. Weak Intrinsic Charge Transfer Complexes: A New Route for Developing Wide Spectrum Organic Photovoltaic Cells. *J. Chem. Phys.* **2002**, *116*, 1713.

(150) Zhang, X. N.; Barrena, E.; de Oteyza, D. G.; De Souza, E.; Dosch, H. Growth of Di-Indenoperylene Single Crystals on Amino-Functionalized SiO$_2$ Surfaces. *J. Appl. Phys.* **2008**, *104*, 104308.

(151) Opitz, A.; Wagner, J.; Br, W.; Salzmann, I.; Koch, N.; Manara, J.; Pflaum, J.; Hinderhofer, A.; Schreiber, F. Charge Separation at Molecular Donor–Acceptor Interfaces : Correlation Between Morphology and Solar Cell Performance. *IEEE J. Sel. Top. Quantum Electron.* **2010**, *16*, 1707–1717.

(152) Akaike, K.; Kanai, K.; Ouchi, Y.; Seki, K. Impact of Ground-State Charge Transfer and Polarization Energy Change on Energy Band Offsets at Donor/acceptor Interface in Organic Photovoltaics. *Adv. Funct. Mater.* **2010**, *20*, 715–721.

(153) Fraxedas, J.; García-Gil, S.; Monturet, S.; Lorente, N.; Fernández-Torrente, I.; Franke, K. J.; Pascual, J. I.; Vollmer, a.; Blum, R. P.; Koch, N.; *et al.* Modulation of Surface Charge Transfer through Competing Long-Range Repulsive versus Short-Range Attractive Interactions. *J. Phys. Chem. C* **2011**, *115*, 18640–18648.

(154) Hirata, I.; Zschieschang, U.; Yokota, T.; Kuribara, K.; Kaltenbrunner, M.; Klauk, H.; Sekitani, T.; Someya,

T. High-Resolution Spatial Control of the Threshold Voltage of Organic Transistors by Microcontact Printing of Alkyl and Fluoroalkylphosphonic Acid Self-Assembled Monolayers. *Org. Electron. physics, Mater. Appl.* **2015**, *26*, 239–244.

(155)   Halik, M.; Klauk, H.; Zschieschang, U.; Maisch, S.; Effenberger, F.; Dehm, C.; Schu, M.; Brunnbauer, M.; Stellacci, F. Low-Voltage Organic Transistors with an Amorphous Molecular Gate Dielectric. *Nature* **2004**, *431*, 963–966.

(156)   Yoshida, M.; Uemura, S.; Kodzasa, T.; Kamata, T.; Matsuzawa, M.; Kawai, T. Surface Potential Control of an Insulator Layer for the High Performance Organic FET. *Synth. Met.* **2003**, *137*, 967–968.

(157)   Zan, H. W.; Chou, C. W. Effect of Surface Energy on Pentacene Thin-Film Growth and Organic Thin Film Transistor Characteristics. *Jpn. J. Appl. Phys.* **2009**, *48*, 031501.

(158)   Owens, D. K.; Wendt, R. C. Estimation of the Surface Free Energy of Polymers. *J. Appl. Polym. Sci.* **1969**, *13*, 1741–1747.

(159)   *Modern Approaches to Wettability. Theory and Applications*; Schraeder, Malcom, E.; Loeb, G., Eds.; 1st ed.; Springer Science + Business Media: New York, 1992.

(160)   Ante, F. Contact Effects in Organic Transistors, École Polytechnique Fédérale de Lausanne, 2010.

(161)   Pellerite, M. J.; Dunbar, T. D.; Boardman, L. D.; Wood, E. J. Effects of Fluorination on Self-Assembled Monolayer Formation from Alkanephosphonic Acids on Aluminum: Kinetics and Structure. *J. Phys. Chem. B* **2003**, *107*, 11726–11736.

(162)   Pratontep, S.; Nüesch, F.; Zuppiroli, L.; Brinkmann, M. Comparison between Nucleation of Pentacene Monolayer Islands on Polymeric and Inorganic Substrates. *Phys. Rev. B - Condens. Matter Mater. Phys.* **2005**, *72*, 1–5.

(163)   Dürr, A. C.; Nickel, B.; Sharma, V.; Täffner, U.; Dosch, H. Observation of Competing Modes in the Growth of Diindenoperylene on SiO2. *Thin Solid Films* **2006**, *503*, 127–132.

(164)   Ruiz, R.; Choudhary, D.; Nickel, B.; Toccoli, T.; Chang, K. C.; Mayer, A. C.; Clancy, P.; Blakely, J. M.; Headrick, R. L.; Iannotta, S.; *et al.* Pentacene Thin Film Growth. *Chem. Mater.* **2004**, *16*, 4497–4508.

(165)   Rao, I. V. K.; Mandal, S.; Katiyar, M. Effect of Pentacene Deposition Rate on Device Characteristics of Top Contact Organic Thin Film Transistors. *IEEE Int. Work. Phys. Semicond. Devices, IWPSD* **2007**, 625–627.

(166)   Wu, Y.; Haugstad, G.; Frisbie, C. D. *2013 MRS Spring Meeting: Strain-Driven Recrystallization of DNTT Thin Films Observed by Scanning Probe Microscopy*; 2013.

(167)   Di Carlo, A.; Piacenza, F.; Bolognesi, A.; Stadlober, B.; Maresch, H. Influence of Grain Sizes on the Mobility of Organic Thin-Film Transistors. *Appl. Phys. Lett.* **2005**, *86*, 263501.

(168)   Wang, S. D.; Miyadera, T.; Minari, T.; Aoyagi, Y.; Tsukagoshi, K. Correlation between Grain Size and Device Parameters in Pentacene Thin Film Transistors. *Appl. Phys. Lett.* **2008**, *93*, 043311.

(169)   Chwang, A. B.; Frisbie, C. D. Temperature and Gate Voltage Dependent Transport across a Single Organic Semiconductor Grain Boundary. *J. Appl. Phys.* **2001**, *90*, 1342.

(170)   Kobayashi, S.; Nishikawa, T.; Takenobu, T.; Mori, S.; Shimoda, T.; Mitani, T.; Shimotani, H.; Yoshimoto, N.; Ogawa, S.; Iwasa, Y. Control of Carrier Density by Self-Assembled Monolayers in Organic Field-Effect Transistors. *Nat. Mater.* **2004**, *3*, 317–322.

(171)   Pernstich, K. P.; Haas, S.; Oberhoff, D.; Goldmann, C.; Gundlach, D. J.; Batlogg, B.; Rashid, A. N.; Schitter, G. Threshold Voltage Shift in Organic Field Effect Transistors by Dipole Monolayers on the Gate Insulator. *J. Appl. Phys.* **2004**, *96*, 6431.

(172)   Salinas, M.; Jäger, C. M.; Amin, A. Y.; Dral, P. O.; Meyer-Friedrichsen, T.; Hirsch, A.; Clark, T.; Halik, M. The Relationship between Threshold Voltage and Dipolar Character of Self-Assembled Monolayers in Organic Thin-Film Transistors. *J. Am. Chem. Soc.* **2012**, *134*, 12648–12652.

(173)   Huang, C.; Katz, H. E.; West, J. E. Solution-Processed Organic Field-Effect Transistors and Unipolar

Inverters Using Self-Assembled Interface Dipoles on Gate Dielectrics. *Langmuir* **2007**, *23*, 13223–13231.

(174) Celle, C.; Suspène, C.; Ternisien, M.; Lenfant, S.; Guérin, D.; Smaali, K.; Lmimouni, K.; Simonato, J. P.; Vuillaume, D. Interface Dipole: Effects on Threshold Voltage and Mobility for Both Amorphous and Poly-Crystalline Organic Field Effect Transistors. *Org. Electron.* **2014**, *15*, 729–737.

(175) Nausieda, I.; Ryu, K. K.; He, D. Da; Akinwande, A. I.; Bulovi, V.; Sodini, C. G. Dual Threshold Voltage Organic Thin-Film Transistor Technology. *IEEE Trans. Electron Devices* **2010**, *57*, 3027–3032.

(176) Possanner, S. K.; Zojer, K.; Pacher, P.; Zojer, E.; Schürrer, F. Threshold Voltage Shifts in Organic Thin-Film Transistors Due to Self-Assembled Monolayers at the Dielectric Surface. *Adv. Funct. Mater.* **2009**, *19*, 958–967.

(177) Sugimura, H.; Hayashi, K.; Saito, N. Surface Potential Microscopy for Organized Molecular Systems. **2002**, *188*, 403–410.

(178) Pacher, P.; Lex, A.; Proschek, V.; Etschmaier, H.; Tchernychova, E.; Sezen, M.; Scherf, U.; Grogger, W.; Trimmel, G.; Slugovc, C.; *et al.* Chemical Control of Local Doping in Organic Thin-Film Transistors: From Depletion to Enhancement. *Adv. Mater.* **2008**, *20*, 3143–3148.

(179) Fleischli, F. D.; Suárez, S.; Schaer, M.; Zuppiroli, L. Organic Thin-Film Transistors: The Passivation of the Dielectric-Pentacene Interface by Dipolar Self-Assembled Monolayers. *Langmuir* **2010**, *26*, 15044–15049.

(180) Ausserlechner, S. J.; Gruber, M.; Hetzel, R.; Flesch, H.-G.; Ladinig, L.; Hauser, L.; Haase, A.; Buchner, M.; Resel, R.; Schürrer, F.; *et al.* Mechanism of Surface Proton Transfer Doping in Pentacene Based Organic Thin-Film Transistors. *Phys. Status Solidi* **2012**, *209*, 181–192.

(181) Celle, C.; Suspene, C.; Simonato, J.; Lenfant, S.; Ternisien, M.; Vuillaume, D. Self-Assembled Monolayers for Electrode Fabrication and Efficient Threshold Voltage Control of Organic Transistors with Amorphous Semiconductor Layer. *Org. Electron.* **2009**, *10*, 119–126.

(182) Brukman, M. J.; Marco, G. O.; Dunbar, T. D.; Boardman, L. D.; Carpick, R. W. Nanotribological Properties of Alkanephosphonic Acid Self-Assembled Monolayers on Aluminum Oxide : Effects of Fluorination and Substrate Crystallinity. *Langmuir* **2006**, *22*, 3988–3998.

(183) Głowacki, E. D.; Irimia-Vladu, M.; Kaltenbrunner, M.; Gsiorowski, J.; White, M. S.; Monkowius, U.; Romanazzi, G.; Suranna, G. P.; Mastrorilli, P.; Sekitani, T.; *et al.* Hydrogen-Bonded Semiconducting Pigments for Air-Stable Field-Effect Transistors. *Adv. Mater.* **2013**, *25*, 1563–1569.

(184) Kaltenbrunner, M.; Sekitani, T.; Reeder, J.; Yokota, T.; Kuribara, K.; Tokuhara, T.; Drack, M.; Schwödiauer, R.; Graz, I.; Bauer-Gogonea, S.; *et al.* An Ultra-Lightweight Design for Imperceptible Plastic Electronics. *Nature* **2013**, *499*, 458–463.

(185) Klauk, H.; Zschieschang, U.; Pflaum, J.; Halik, M. Ultralow-Power Organic Complementary Circuits. *Nature* **2007**, *445*, 745–748.

(186) Jedaa, A.; Salinas, M.; Jäger, C. M.; Clark, T.; Ebel, A.; Hirsch, A.; Halik, M. Mixed Self-Assembled Monolayer of Molecules with Dipolar and Acceptor character—Influence on Hysteresis and Threshold Voltage in Organic Thin-Film Transistors. *Appl. Phys. Lett.* **2012**, *100*, 063302.

(187) Hanson, E. L.; Schwartz, J.; Nickel, B.; Koch, N. Bonding Self-Assembled , Compact Organophosphonate Monolayers to the Native Oxide Surface of Silicon. *J. Am. Chem. Soc.* **2003**, *125*, 16074–16080.

(188) Barriet, D.; Lee, T. R. Fluorinated Self-Assembled Monolayers: Composition, Structure and Interfacial Properties. *Curr. Opin. Colloid Interface Sci.* **2003**, *8*, 236–242.

(189) Ciferri, A. *Supramolecular Polymers*; Marcel Dekker Inc. New York, Basel, 2000.

(190) Heimel, G.; Rissner, F.; Zojer, E. Modeling the Electronic Properties of Pi-Conjugated Self-Assembled Monolayers. *Adv. Mater.* **2010**, *22*, 2494–2513.

(191) Mühlenen, A. Von; Castellani, M.; Schaer, M.; Zuppiroli, L. Controlling Charge-Transfer at the Gate Interface of Organic Field-Effect Transistors. *Phys. Status Solidi* **2008**, *245*, 1170–1174.

(192) Suemori, K.; Uemura, S.; Yoshida, M.; Hoshino, S.; Takada, N.; Kodzasa, T.; Kamata, T. Threshold Voltage Stability of Organic Field-Effect Transistors for Various Chemical Species in the Insulator Surface. *Appl. Phys. Lett.* **2007**, *91*, 192112.

(193) Ellison, D. J.; Lee, B.; Podzorov, V.; Frisbie, C. D. Surface Potential Mapping of SAM-Functionalized Organic Semiconductors by Kelvin Probe Force Microscopy. *Adv. Mater.* **2011**, *23*, 502–507.

(194) Gholamrezaie, F.; Andringa, A.-M.; Roelofs, W. S. C.; Neuhold, A.; Kemerink, M.; Blom, P. W. M.; de Leeuw, D. M. Charge Trapping by Self-Assembled Monolayers as the Origin of the Threshold Voltage Shift in Organic Field-Effect Transistors. *Small* **2012**, *8*, 241–245.

(195) Wu, Y.; Haugstad, G.; Frisbie, C. D. Electronic Polarization at Pentacene/Polymer Dielectric Interfaces: Imaging Surface Potentials and Contact Potential Differences as a Function of Substrate Type, Growth Temperature, and Pentacene Microstructure. *J. Phys. Chem. C* **2014**, *118*, 2487–2497.

(196) Boulas, C.; Davidovits, J. V; Rondelez, F.; Vuillaume, D. Suppression of Charge Carrier Tunneling through Organic Self-Assembled Monolayers. *Phys. Rev. Lett.* **1996**, *76*, 4797–4800.

(197) Dhar, B. M.; Özgün, R.; Dawidczyk, T.; Andreou, A.; Katz, H. E. Threshold Voltage Shifting for Memory and Tuning in Printed Transistor Circuits. *Mater. Sci. Eng. R* **2011**, *72*, 49–80.

(198) Suárez, S.; Fleischli, F. D.; Schaer, M.; Zuppiroli, L. From Oxide Surface to Organic Transistor Properties : The Nature and the Role of Oxide Gate Surface Defects. *J. Phys. Chem. C* **2010**, *114*, 7153–7160.

(199) Lee, J. Pentacene-Based Photodiode with Schottky Junction. *Thin Solid Films* **2004**, *451-452*, 12–15.

(200) Zschieschang, U.; Ante, F.; Kälblein, D.; Yamamoto, T.; Takimiya, K.; Kuwabara, H.; Ikeda, M.; Sekitani, T.; Someya, T.; Nimoth, J. B.-; *et al.* Dinaphtho[2,3-b:2',3'-f]thieno[3,2-B]thiophene (DNTT) Thin-Film Transistors with Improved Performance and Stability. *Org. Electron.* **2011**, *12*, 1370–1375.

(201) Bisoyi, S.; Zschieschang, U.; Kang, M. J.; Takimiya, K.; Klauk, H.; Tiwari, S. P. Bias-Stress Stability of Low-Voltage P-Channel and N-Channel Organic Thin-Film Transistors on Flexible Plastic Substrates. *Org. Electron.* **2014**, *15*, 3173–3182.

(202) Kraft, U.; Sejfić, M.; Kang, M. J.; Takimiya, K.; Zaki, T.; Letzkus, F.; Burghartz, J. N.; Weber, E.; Klauk, H. Flexible Low-Voltage Organic Complementary Circuits: Finding the Optimum Combination of Semiconductors and Monolayer Gate Dielectrics. *Adv. Mater.* **2015**, *27*, 207–214.

(203) Milvich, J.; Zaki, T.; Aghamohammadi, M.; Rödel, R.; Kraft, U.; Klauk, H.; Burghartz, J. N. Flexible Low-Voltage Organic Phototransistors Based on Air-Stable dinaphtho[2,3-b:2',3'-f]thieno[3,2-B]thiophene (DNTT). *Org. Electron.* **2015**, *20*, 63–68.

(204) Li, D.; Borkent, E.-J.; Nortrup, R.; Moon, H.; Katz, H.; Bao, Z. Humidity Effect on Electrical Performance of Organic Thin-Film Transistors. *Appl. Phys. Lett.* **2005**, *86*, 042105.

(205) Weitz, R. T.; Amsharov, K.; Zschieschang, U.; Burghard, M.; Jansen, M.; Kelsch, M.; Rhamati, B.; van Aken, P. A.; Kern, K.; Klauk, H. The Importance of Grain Boundaries for the Time-Dependent Mobility Degradation in Organic Thin-Film Transistors. *Chem. Mater.* **2009**, *21*, 4949–4954.

(206) Zschieschang, U.; Kang, M. J.; Takimiya, K.; Sekitani, T.; Someya, T.; Canzler, T. W.; Werner, A.; Blochwitz-Nimoth, J.; Klauk, H. Flexible Low-Voltage Organic Thin-Film Transistors and Circuits Based on C 10 -DNTT. *J. Mater. Chem.* **2012**, *22*, 4273–4277.

(207) Zschieschang, U.; Hofmockel, R.; Rödel, R.; Kraft, U.; Kang, M. J.; Takimiya, K.; Zaki, T.; Letzkus, F.; Butschke, J.; Richter, H.; *et al.* Megahertz Operation of Flexible Low-Voltage Organic Thin-Film Transistors. *Org. Electron.* **2013**, *14*, 1516–1520.

(208) Yokota, T.; Kuribara, K.; Tokuhara, T.; Zschieschang, U.; Klauk, H.; Takimiya, K.; Sadamitsu, Y.; Hamada, M.; Sekitani, T.; Someya, T. Flexible Low-Voltage Organic Transistors with High Thermal Stability at 250 °C. *Adv. Mater.* **2013**, *25*, 3639–3644.

(209) Oh, S.; Yu, J.-S.; Lim, J.; Jadhav, M.; Lee, T.-M.; Kim, D.; Kim, C. Highly Flexible Magnetoelectronic Device Integrated With Embedded Ag Nanoparticle Electrode. *IEEE Sens. J.* **2013**, *13*, 3957–3961.

139

(210)   Savu, V.; van den Boogaart, M. A. F.; Brugger, J.; Arcamone, J.; Sansa, M.; Perez-Murano, F. Dynamic Stencil Lithography on Full Wafer Scale. *J. Vac. Sci. Technol. B* **2008**, *26*, 2054.

List of Figures

145

146

List of acronyms

2D	two-dimensional
3D	three-dimensional
A	acceptor
AC	alternating current
AFM	atomic force microscopy
ALD	atomic layer deposition
AM-KPFM	amplitude-modulation Kelvin probe force microscopy
BCB	benzocyclobutene
BW	backward
C-AFM	conductive atomic force microscopy
CPD	contact potential difference
CT	charge transfer
D	donor
D/A	donor/acceptor
DC	direct current
DIP	diindenoperylene
DNTT	Dinaphtho[2,3-b:2´,3´-f]thieno[3,2-b]thiophene
DOS	density of states
ELR	extrapolation in the linear region
ESR	extrapolation in the saturation region
FET	field-effect transistor
FFM	friction force microscopy
FFT	fast Fourier transform
FM-KPFM	frequency-modulation Kelvin probe force microscopy
FW	forward
HOMO	highest occupied molecular orbital
HOPG	highly-oriented pyrolytic graphite
KPFM	Kelvin probe force microscopy
LFM	lateral force microscopy
LUMO	lowest unoccupied molecular orbital
MISFET	metal-insulator-semiconductor field-effect transistor
ML	monolayer
MOSFET	metal-oxide-semiconductor field-effect transistor
MTR	multiple trapping and release model
OFET	organic field-effect transistor
OLED	organic light-emitting diode

OPVC	organic photovoltaic cell
OTFT	organic thin-film transistor
PDMS	polydimethylsiloxane
PEN	polyethylene naphthalate
PL	photoluminescence
PTCDI-C_8	N,N′-dioctyl-3,4,9,10-perylene tetracarboxylicdiimide
SAM	self-assembled monolayer
SAMFET	self-assembled monolayer field-effect transistor
SD	second derivative
SKPM	scanning Kelvin probe force microscopy
SP	surface potential
TFT	thin-film transistor
TSM	transverse shear microscopy
UPS	ultraviolet photoelectron spectroscopy
XRD	X-ray diffraction

Curriculum Vitae

Mahdieh Schmidt (*nee* Aghamohammadi)

25/11/1986   Born in Aachen, Germany

2001-2005   Farzanegan High School, Tehran, Iran

2005-2009   B.Sc. in Physics, Khaje Nasir Toosi University of Technology, Tehran, Iran

2010-2011   Masters in Nanotechnology, Autonomous University of Barcelona (UAB), Barcelona, Spain; Supervisors: Dr. Mariano Campoy-Quiles and Dr. Christian Müller

Since 2011   PhD student in Physics, Autonomous University of Barcelona (UAB), Barcelona, Spain; Supervisors: Dr. Esther Barrena and Dr. Hagen Klauk

2011-2013   PhD research work at the Materials Science Institute of Barcelona (ICMAB-CSIC), Barcelona, Spain

2013-2016   PhD research work at Max Planck Institute for Solid State Research (MPI-FKF), Stuttgart, Germany

List of publications

- *Threshold-Voltage Shifts in Organic Transistors Due to Self-Assembled Monolayers at the Dielectric: Evidence for Electronic Coupling and Dipolar Effects*

M. Aghamohammadi, R. Rödel, U. Zschieschang, C. Ocal, H. Boschker, R. T. Weitz, E. Barrena, H. Klauk

ACS Applied Materials and Interfaces (2015), DOI: 10.1021/acsami.5b02747

- *Threshold-voltage control and enhancement-mode characteristics in multilayer tin disulfide field-effect transistors by gate-oxide passivation with an alkylphosphonic acid self-assembled monolayer*

U. Zschieschang, T. Holzmann, A. Kuhn, **M. Aghamohammadi**, B. V. Lotsch, H. Klauk

Journal of Applied Physics (2015) DOI: 10.1063/1.4914488

- *Flexible low-voltage organic phototransistors based on air-stable dinaphtho[2,3-b:2′,3′-f]thieno[3,2-b]thiophene (DNTT)*

J. Milvich, Tarek Zaki, **M. Aghamohammadi**, R. Rödel, U. Kraft, H. Klauk, J. N. Burghartz

Organic Electronics (2015), DOI: 10.1016/j.orgel.2015.02.007

- *Influence of the Relative Molecular Orientation on Interfacial Charge-Transfer Excitons at Donor/Acceptor Nanoscale Heterojunctions*

M. Aghamohammadi, A. Fernandez, M. Schmidt, A. Perez, A. Goni, J. Frexedas, G. Sauthier, M. Paradinas, C. Ocal, E. Barrena

Journal of Physical Chemistry C (2014), DOI: 10.1021/jp5041579

- *Interplay Between Fullerene Surface Coverage and Contact Selectivity of Cathode Interfaces in Organic Solar Cells*

A. Guerrero, B. Dörling, T.Ripolles-Sanchis, **M. Aghamohammadi**, E. Barrena, M. Campoy-Quiles, G. Garcia-Belmonte

ACS Nano (2013), DOI: 10.1021/nn4014593

- *One-Step Macroscopic Alignment of Conjugated Polymer Systems by Epitaxial Crystallization during Spin-Coating*

C. Müller, **M. Aghamohammadi**, S. Himmelberger, P. Sonar, M. Garriga, A. Salleo, M. Campoy-Quiles

Advanced Functional Materials (2012), DOI: 10.1002/adfm.201202983

List of presentations

- *Evidence for Electronic Coupling and Dipolar Effects as Mechanisms for Threshold Voltage Shift in Organic Transistors with Self-Assembled Monolayers*

Materials Research Society Fall meeting, Boston, MA, USA (2015)
Poster Presentation

- *Threshold Voltage Modification in Organic Transistors with Self-Assembled Monolayers: The Bigger Picture*

European Materials Research Society Spring meeting, Lille, France (2015)
Oral Presentation
Award: Young Scientist Award for the best talk

- *Kelvin Probe Force Microscopy Investigations on the Gate-Dielectric Interface in High-Mobility Organic Thin-Film Transistors*

56th Electronic Materials Conference, Santa Barbara, CA, USA (2014)
Oral Presentation

- *Molecular-scale Investigation of Organic-Organic Heterostructures*

International conference on Nanotechnologies & Organic Electronics (Nanotexnology), Thessaloniki, Greece (2013)
Poster Presentation

- *Energy Alignment at Organic-organic Heterojunctions Investigated by KPFM*

Force and Tunnels conference, Madrid, Spain (2012)
Oral Presentation

Acknowledgments

During my PhD I have had the advantage of working in two different scientific environments, MPI in Stuttgart and ICMAB in Barcelona, which made the experience incredibly versatile, worthwhile and enjoyable. The experience would not have been the same without the support from a number of amazing people.

Firstly, I would like to thank my research advisors, Dr. Esther Barrena and Dr. Hagen Klauk. I have been privileged to benefit from their immensely insightful, yet dissimilar supervisions during my PhD. Esther's dedication to ensure that I developed self-discipline and scientific integrity was vital to my professional growth as a scientist. Hagen's constant encouragement to present my work and participate in research experiences and his incredible openness and flexibility helped me develop more initiative and achieve a more independent professional character.

I acknowledge the former and current members of the group of Physical Chemistry of Surfaces and Interfaces at ICMAB: Professor Carmen Ocal, Dr. Marcos Paradinas, Dr. Sonia Matencio, Dr. Lucho Garzon and Ana Pérez for their kind support. I thank the former and current ICMAB fellows: Reza and the ICMAB choir for good times; Dr. Mariano Campoy and Dr. Christian Müller, my master's supervisors, for their good faith and triggering the first scientific flames in me.

I acknowledge the former and current members of the Organic Electronics group at the MPI, Dr. Michael Strecker, Dr. Ulrike Kraft and James Borchert for creating a rich scientific environment and for interesting daily conversations at the lunch table. I am deeply grateful to Dr. Ute Zschieschang for her selfless help around the lab and her calm and open personality. My special gratitude goes to Dr. Reinhold Rödel (the physicist in the group) for his generous help around the lab and valuable scientific input when it came to deep concepts in physics. I am thankful to Dr. Sibani Bisoyi for her warm presence and priceless friendship.

I appreciate the help of Marion Hagel for the endless ALD depositions. I extend my gratitude to Dr. Hans Boschker, for his once-very-critical, yet helpful assessment of my work and for his friendship.

Extending beyond the laboratory, I have enjoyed spending time with my lovely colleagues during coffee breaks at the MPI and in the Ringberg castle. I thank Maryam, Jone, Kristina, Iman, Parmida, Muriel and Joel for all the good times spent together. I am thankful to René

for his open heart, friendship and the strong coffee he provided me with during my writing process.

I thank my dear sister Atiyeh and her husband Meysam for the memorable Sunday lunches in Barcelona and their continuous hospitality during my short stays in Barcelona.

Last but not least, I want to thank my parents for their constant faith in me and supporting my decisions both in my academic and in my personal life. Words can't explain the support I have gotten from my mother during my PhD. Maman, Thanks for listening to me stressing out over the phone for hours and hours. You are simply amazing! I want to thank my role model, my father, for his years of mentoring me. Baba, I am a better person because of you.

Above all, none of this would have been possible without the loving support of my former colleague and now- husband and best friend, Malte. Schatz, wir haben es geschafft!